Path integral and qubit encoding techniques for quantum simulations of discrete planar rotor lattices

by

Muhammad Shaeer Moeed

A thesis
presented to the University of Waterloo
in fulfillment of the
thesis requirement for the degree of
Master Of Science
in
Chemistry (Quantum Information)

Waterloo, Ontario, Canada, 2025

© Muhammad Shaeer Moeed 2025

Author's Declaration

This thesis consists of material all of which I authored or co-authored: see Statement of Contributions included in the thesis. This is a true copy of the thesis, including any required final revisions, as accepted by my examiners.

I understand that my thesis may be made electronically available to the public.

Statement of Contributions

Aside from chapter 1 and chapter 4, this thesis is composed of manuscripts (published or in preparation) to which I have contributed significantly, but not exclusively. Following is a delineation of my co-authors' contributions towards each manuscript:

- Chapter 2: This chapter is reproduced from Muhammad Shaeer Moeed, Tobias Serwatka and Pierre-Nicholas Roy; "Pair approximating the action for molecular rotations in path integral Monte Carlo", Journal of Chemical Physics 162 (2), 024113 (2025). Tobias Serwatka contributed his density matrix renormalization group calculations and code for benchmarking. Pierre-Nicholas Roy engaged in fruitful discussions, suggested changes to the text of the manuscript, and contributed to the conceptualization and methodology of the work.

- Chapter 3: This chapter is based on Muhammad Shaeer Moeed, James Brown, Estevao De Oliveira, and Pierre-Nicholas Roy, "Qubit encodings for lattices of dipolar planar rotors" (manuscript in preparation, to be submitted in 2025). James Brown developed the binary qubit encoding and contributed his expertise in state vector simulations using Tangelo. Estevao De Oliveira made recommendations towards the methodology. Pierre-Nicholas Roy engaged in fruitful discussions, suggested changes to the text of the manuscript, and contributed to the conceptualization and methodology of the work.

Additionally, I contributed to the following publication during the course of my Master's research which I have chosen to exclude from this thesis, since I was not the primary author:

- Wenxue Zhang, Muhammad Shaeer Moeed, Andrew Bright, Tobias Serwatka, Estevao De Oliveira, Pierre-Nicholas Roy; "Path integral Monte Carlo in a discrete variable representation with Gibbs sampling: Dipolar planar rotor chain" Journal of Chemical Physics, 162 (1), 014106 (2025)

Abstract

Typical path integral Monte Carlo approaches use the primitive approximation to compute the probability density for a given path. In this thesis, we investigate the utility of pair approximating the action in path integral ground state simulations targeting planar rotations. The pair propagator, which was initially introduced to study superfluidity in condensed Helium, is naturally well-suited for systems interacting with a pair-wise potential. Consequently, paths sampled using the pair action tend to be closer to the exact paths (compared to primitive Trotter paths) for such systems leading to convergence with less imaginary time steps. Our approach relies on using the pair factorization in conjunction with a rejection-free path integral ground state paradigm to study a chain of planar rotors interacting with a pair-wise dipole-dipole interaction. We first use a heat kernel expansion to analyze the asymptotics of the pair propagator in imaginary time. Then, we exhibit the utility of the pair factorization scheme via convergence studies comparing the pair and primitive propagators. Finally, we compute energetic and structural properties of this system including the orientational correlation and Binder ratio as functions of the coupling strength to examine the behavior of the pair-DVR method near criticality. Density matrix renormalization group calculations are used for benchmarking throughout.

Near term quantum devices have recently garnered significant interest as promising candidates for investigating difficult-to-probe regimes in many-body physics. To this end, various qubit encoding schemes targeting second quantized Hamiltonians have been proposed and optimized. In this thesis, we also investigate two qubit representations of the planar rotor lattice Hamiltonian. The first representation is realized by decomposing the rotor Hamiltonian projectors in binary and mapping them to spin-1/2 projectors. The second approach relies on embedding the planar rotor lattice Hilbert space in a larger space and recovering the relevant qubit encoded system as a quotient space projecting down to the physical degrees of freedom. This is typically called the unary mapping and is used for bosonic systems. We establish the veracity of the two encoding approaches using sparse diagonalization on small chains and discuss quantum phase estimation resource requirements to simulate small planar rotor lattices on near-term quantum devices.

Acknowledgements

I would firstly like to thank my supervisor: Professor Pierre-Nicholas Roy, for his continuous support and invaluable guidance. None of the work contained in this thesis would have been possible without his exemplary supervision.

I would also like to thank my committee members: Professor Marcel Nooijen and Professor Jonathan Baugh. Their constructive feedback helped me elevate the quality of my research.

Additionally, I would like to acknowledge my collaborators: Dr. James Brown, Dr. Tobias Serwatka, Wenxue Zhang and Estevao De Oliveira, as well as the rest of the theoretical chemistry group at the University of Waterloo for the helpful discussions we had about quantum simulation techniques during my time here.

Finally, I would like to acknowledge the support and encouragement of my family and friends throughout this process.

Table of Contents

Author's Declaration **ii**

Statement of Contributions **iii**

Abstract **iv**

Acknowledgements **v**

List of Figures **ix**

List of Tables **x**

List of Abbreviations **xi**

Graphical Abstract **xii**

1 Introduction **1**

1.1 Quantum Mechanics of Planar Rotations 3

1.1.1 Canonical Quantization of Classical Rotors 3

1.1.2 Discrete Representations Of Planar Rotors 5

1.1.3 Planar Rotor Lattices From The Transverse Field Ising Model . . . 14

1.2 Quantum Statistical Mechanics of Planar Rotations 15

1.2.1 Imaginary-Time Path Integrals 16
1.2.2 Path Integral Ground State 24
1.2.3 Quantum Phase Transitions 28
1.3 Quantum Monte Carlo For Planar Rotations 31
1.3.1 Metropolis-Hastings 33
1.3.2 Gibbs Sampling 34
1.4 Thesis Outline 35

2 Pair Approximating The Action For Molecular Rotations In Path Integral Monte Carlo 36

2.1 Introduction 36
2.2 Theory 38
2.2.1 Planar Rotor Chain 38
2.2.2 The Pair Approximation 39
2.2.3 Pair Density Error 41
2.2.4 Path Integral Ground State Estimators 45
2.2.5 Discrete Variable Representation 47
2.2.6 Sequentially Gibbs Sampling The Pair Density 48
2.2.7 The Sign Problem 50
2.2.8 Numerical Matrix Multiplication 51
2.3 Results & Discussion 52
2.3.1 Convergence Studies 52
2.3.2 Energetic Properties 56
2.3.3 Structural Properties 58
2.4 Conclusions 61
2.5 Supplementary Material 62

2.5.1 Green's Function Differential Equation 62
2.5.2 Rotational Free Propagator Asymptotics 62
2.5.3 Second Term Of The Wigner-Kirkwood Expansion 63
2.5.4 Pair Density Error 64

3 Qubit Encodings For Planar Rotor Lattices 67
3.1 Introduction 67
3.2 Theoretical Framework 68
3.2.1 Planar Rotor Lattice 68
3.2.2 Binary Qubit Encoding 71
3.2.3 Unary Qubit Encoding 74
3.2.4 Quantum Phase Estimation 79
3.3 Computational Results & Discussion 80
3.3.1 Sparse Diagonalization 80
3.3.2 Phase Estimation 83
3.4 Conclusions & Outlook 87

4 Conclusions & Future Directions 89
4.1 Future Work 90
4.1.1 Entanglement Entropy 90
4.1.2 Higher Dimensional Lattices 92
4.1.3 Stochastic Series Expansion 93
4.1.4 Variational Quantum Eigensolver 95

References 96

List of Figures

1.1 Ground state energy convergence with increasing frequency cutoff 13
1.2 Rotational free propagator reciprocal temperature dependence 21
1.3 Brownian motion on a circle 23
2.1 Schematic representation of a chain of planar rotors. 38
2.2 Sampling comparison of the pair and symmetric Trotter factorizations . . . 50
2.3 Pair propagated energy asymptotics in imaginary time 53
2.4 Numerical matrix multiplication energy convergence in imaginary time . . 54
2.5 Monte Carlo energy convergence in imaginary time 55
2.6 Ground state energy for a chain of 150 rotors 56
2.7 Ground state energy per particle convergence with number of particles . . 57
2.8 Ground state correlation for a chain of 150 rotors 59
2.9 Binder ratio for a chain of 150 rotors 60
3.1 Schematic representation of the unary encoding for a coplanar chain 76
3.2 Circuit diagram for quantum phase estimation 79
3.3 Sparse diagonalization results (2 rotors) 81
3.4 Sparse diagonalization results (3 rotors) 82
3.5 Trotter convergence of quantum phase estimation (2 rotors) 84
3.6 Trotter convergence of quantum phase estimation (3 rotors) 85
3.7 Energy gap and phase estimation register bound for a small chain 86
4.1 Rotor chain subsystems for entanglement entropy 91

List of Tables

3.1 Quantum Phase Estimation Simulation Paramters 86

List of Abbreviations

BCH Baker–Campbell–Hausdorff

DMRG Density Matrix Renormalization Group

DVR Discrete Variable Representation

ED Exact Diagonalization

FBR Finite Basis Representation

HVA Hamiltonian Variational Ansatz

MC Monte Carlo

MCMC Markov Chain Monte Carlo

MH Metropolis-Hastings

MPS Matrix Product State

NMM Numerical Matrix Multiplication

PIGS Path Integral Ground State

PIMC Path Integral Monte Carlo

QAPR Quantum Anisotropic Planar Rotor

QMC Quantum Monte Carlo

QPE Quantum Phase Estimation

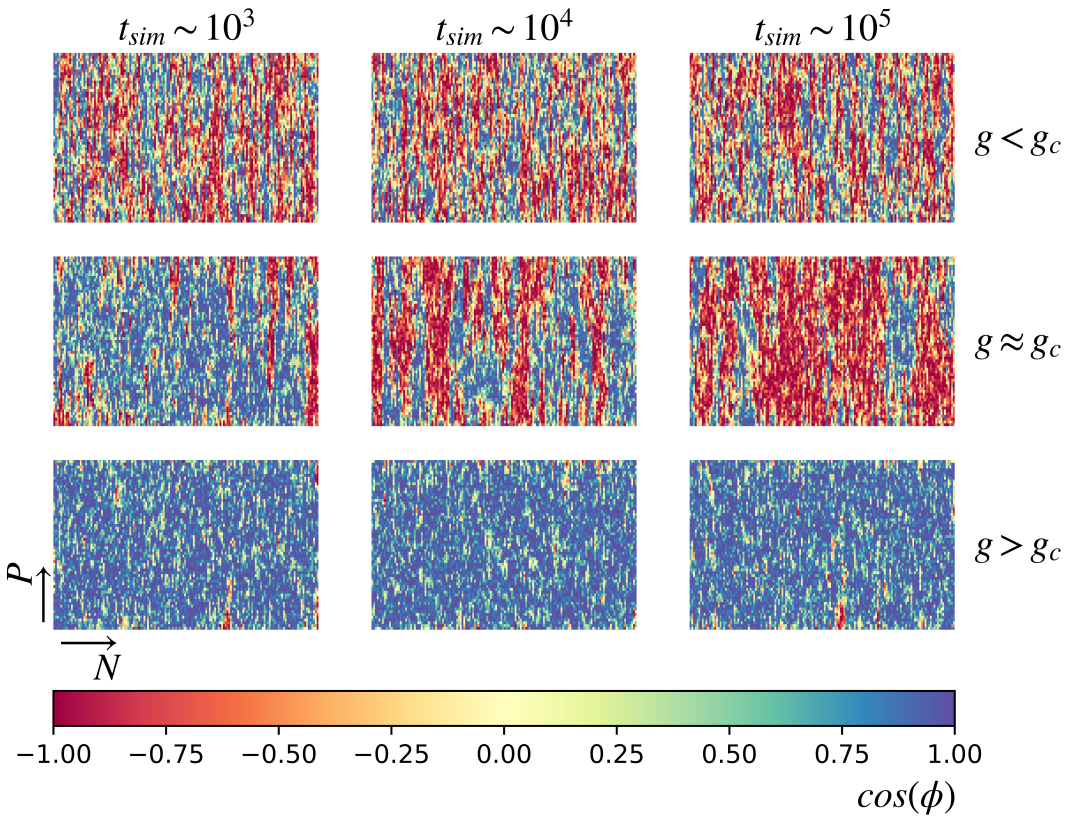
SSE Stochastic Series Expansion

TFIM Transverse Field Ising Model

VBR Variational Basis Representation

VQE Variational Quantum Eigensolver

Graphical Abstract



This graphical abstract has been reproduced from Muhammad Shaeer Moeed, Tobias Serwatka and Pierre-Nicholas Roy, "Pair approximating the action for molecular rotations in path integral Monte Carlo", Journal of Chemical Physics 162 (2), 024113 (2025), with the permission of AIP Publishing.

Chapter 1

Introduction

Of central importance to condensed matter physics and theoretical chemistry is the idea of emergence; that the behavior of a collection of degrees of freedom can be different from that of its constituents.[1–3] Perhaps this is most famously exhibited by the phenomenon of spontaneous symmetry breaking in the Ising model; while the microscopic Hamiltonian is symmetric under spin inversion, the ground state only retains that $\mathbb{Z}_2$ symmetry at high temperatures in the thermodynamic limit. As the temperature is lowered, the system undergoes a continuous phase transition, becomes ordered and attains a ferromagnetic phase.[4,5] The transition point itself is characterized by diverging correlation lengths which cause the many-body physics to become invariant under scale transformations. This allows one to construct a macroscopic theory (via the so-called renormalization group flow) to describe the statistical mechanics of critical systems near the continuous phase transition.[3–6] The resulting effective field theories abstract away the microscopic details of the systems they model and classify the large-scale behavior of a wide array of strikingly different Hamiltonians into a handful of "universality classes".[4,7] A powerful example of this is the 3D XY universality class which models the continuous superfluid transition of Helium-4 as well as the superconductor-insulator transition in the fermionic Hubbard model.[8–10]

While analyzing the macroscopic properties of microscopically simple systems such as (some variants of) the Ising model is analytically tractable, the same cannot be said about the vast majority of many-body systems relevant to physics and chemistry.[4,11] Consequently, studying the large-scale behavior of such systems necessitates the reduction of physical Hamiltonians into simpler models capable of capturing the relevant physics of the system

under question, as well as the development of robust algorithmic tools for calculating the equilibrium properties of many-body quantum systems.[11–13] Towards the latter objective, various computational techniques have been developed over the past 5 decades to circumvent the exponential scaling of exact matrix diagonalization with system size, such as the Density Matrix Renormalization Group (DMRG), coupled cluster approaches and Path Integral Monte Carlo (PIMC) methods.[14–16] This thesis will focus on optimizing path integral techniques for one such model: a lattice of planar rotors.[17,18] We use a 1d chain with a $\mathbb{Z}_2$ dipole-dipole interaction because it has been shown to undergo a quantum phase transition, parameterized by the coupling strength, that is in the same universality class as the (1+1)d Ising model.[19,20] Since path integral techniques suffer from an exponential slowdown in convergence near continuous phase transitions and scale polynomially in lattice dimensions, this system provides an excellent testing ground for optimizing Quantum Monte Carlo (QMC) techniques targeting molecular rotations restricted to a plane.[20–22]

As model systems, planar rotor lattices have wide ranging applications in chemistry and physics. They can be used to model the low temperature behavior of water molecules confined in crystals such as Beryl and Cordierite.[23,24] Experimental results have shown that the crystal structure screens the usual Hydrogen bonding between the water molecules and allows them to interact via their dipolar couplings.[23] This allows for the formation of an ordered phase causing the system to exhibit ferroelectricity.[24] Moreover, 2d planar rotor lattices model the orientational ordering of homo-nuclear diatomic molecules e.g. N_2 adsorbed on inert surfaces such as graphite.[17] This is called the Quantum Anisotropic Planar Rotor (QAPR) model which assumes that the molecules perform uniaxial rotation with fixed bond-lengths while interacting with a quadrupolar dipole-dipole interaction.[25,26] Past theoretical work has suggested that the QAPR model displays a re-entrant phase transition i.e. at high temperatures, the system is in the disordered phase and as the temperature is lowered, it first enters an ordered phase and then re-enters a disordered phase.[17,25,27]

In condensed matter physics, planar rotors with a dot product interaction are used to construct the classical XY model as well as the chiral $\mathbb{Z}_d$ quantum clock model.[28–31] The latter corresponds to a lattice of discretized rotors with a broken chiral symmetry.[30] 1d chains of achiral quantum clocks are mathematically equivalent to a theory of interacting para-fermions and chiral variations of this model have been shown to admit topological order.[31] Furthermore, 1d Rydberg atom arrays have been experimentally shown to display quantum phase transitions in the same universality class as the $\mathbb{Z}_d$ quantum clock

model.[32,33] The phase diagram of this system has been investigated in the past both computationally as well as theoretically using renormalization group analysis due to its rich structure.[30,34] Depending on the order of discretization (d) and the existence of a chiral symmetry breaking term, the model admits either 2 or 3 distinct phases.[30,31] For large d, there is a gapless phase between the two gapped phases; one that preserves the $\mathbb{Z}_d$ symmetry and another that breaks it. For small d, the phase diagram only contains the 2 gapped phases with a continuous phase transition separating them. Interestingly, the universality class of the transition in the quantum clock model depends on d.[30] It is the existence of such complexity in the phase diagrams of these systems that underscores the need to optimize our simulation techniques targeting planar rotor lattices, and motivates the work contained in this thesis.

This chapter is organized as follows: we start with the canonical quantization of continuous rotors to derive the quantum Hamiltonian we use throughout this thesis. We also discuss here the various discretization schemes that have proven useful for our computational work. The next section is dedicated to the path integral formulation of the planar rotor problem and the Feynman-Kac theorem. We end this chapter by reviewing some of the Monte Carlo algorithms useful for simulating ground state properties of many-body quantum systems.

1.1 Quantum Mechanics of Planar Rotations

In this section, we construct the Hamiltonian of a lattice of planar rotor from first principles. Starting with the classical Lagrangian of continuous planar rotations, we canonically quantize the associated Hamiltonian. Finally, we consider two different approximate representations of the problem and discuss the connection of one of these discrete representation with the Transverse Field Ising Model (TFIM).

1.1.1 Canonical Quantization of Classical Rotors

Consider a classical particle of mass m rotating around a ring of radius r in the presence of a position dependent potential $V(\boldsymbol{r})$. The dynamics of such a system are determined by the Lagrangian,[35]

$$L = \frac{1}{2} m \dot{\boldsymbol{r}}^2 - V(\boldsymbol{r}) = \frac{1}{2} I \dot{\phi}^2 - V(r, \phi) \tag{1.1}$$

where in the second equality, $I = mr^2$ is the moment of inertia and we have imposed the constraint $\dot{r} = 0$, resolving the problem in polar coordinates. The Hamiltonian associated with this system is the Legendre transform of the above Lagrangian,[35]

$$H(\phi, p_\phi) = \frac{p_\phi^2}{2I} + V(r, \phi), \quad p_\phi = \frac{\partial L}{\partial \dot{\phi}} \tag{1.2}$$

Canonical quantization of the above Hamiltonian function yields the Hamiltonian operator we use throughout this thesis,

$$\hat{H} = \frac{\hat{l}^2}{2I} + \hat{V}, \quad \hat{l} = i\hbar\{p_\phi, \cdot\} = i\hbar\left(\frac{\partial p_\phi}{\partial \phi}\frac{\partial}{\partial p_\phi} - \frac{\partial p_\phi}{\partial p_\phi}\frac{\partial}{\partial \phi}\right) = -i\hbar\frac{\partial}{\partial \phi}, \quad \hat{V} = V(r, \hat{\phi}) \tag{1.3}$$

where $\hat{\phi}$ is the usual multiplication operator in the position representation and $\{\cdot, \cdot\}$ is the Poisson bracket.[36] We will typically set $\hbar = 1$ and $I = 1/2$ throughout this thesis unless stated otherwise. Our system of interest is a lattice of N planar rotors, each of which are taken to represent an electric dipole. These interact electromagnetically as follows,[37]

$$V(\boldsymbol{r}_1, \boldsymbol{r}_2) = \frac{-1}{4\pi\epsilon_0 R^3}(3(\boldsymbol{r}_1 \cdot \boldsymbol{R})(\boldsymbol{r}_2 \cdot \boldsymbol{R}) - \boldsymbol{r}_1 \cdot \boldsymbol{r}_2) \tag{1.4}$$

Here, $\boldsymbol{R}$ is the vector connecting the two sites and ϵ_0 is the permeability of free space. For planar rotors, $\boldsymbol{r} = (r\cos(\phi), r\sin(\phi))$. Moreover, for a 1d lattice (chain), we can pick $\boldsymbol{R}$ to be parallel to the x-axis without loss of generality. This gives,

$$V(\phi_1, \phi_2) = g(\sin(\phi_1)\sin(\phi_2) - 2\cos(\phi_1)\cos(\phi_2)) \tag{1.5}$$

where $g = r^2/(4\pi\epsilon_0 R^3)$ and we have used the fact that all of the dipoles on the lattice are identical ($r_1 = r_2$). For this thesis, we also assume nearest neighbor interactions which yields the following Hamiltonian in the position representation,

$$H = -\sum_{i=1}^{N}\frac{\partial^2}{\partial \phi_i^2} + g\sum_{i=1}^{N-1}(\sin(\phi_i)\sin(\phi_{i+1}) - 2\cos(\phi_i)\cos(\phi_{i+1})) \tag{1.6}$$

Because the Hamiltonian is invariant under the transformation: $\phi_i \to \phi_i + \pi$ for all $i \in \{1, ..., N\}$, this system possesses a $\mathbb{Z}_2$ symmetry. Consequently, we will often refer to this as the $\mathbb{Z}_2$ chain. It is also instructive to note here that this is not the only possible approach to quantization for the classical planar rotor Lagrangian. Other schemes such

as the Dirac bracket approach and path integral techniques have also been examined in the literature.[38–41] However, all of these quantization approaches yield different constant energy offsets. While this is of little consequence to us since our focus is on statistical mechanics which is entirely determined by energy differences, this discrepancy is interesting from the perspective of mathematical physics and reconciliations have been proposed using gauge theoretic techniques in the past.[42] For this thesis, we will restrict ourselves to the Hamiltonian defined in Eq. (1.6).

1.1.2 Discrete Representations Of Planar Rotors

In this subsection, we construct two different discretizations of the continuous rotor Hamiltonian. The first approach relies on using finite differences to approximate the second derivative kinetic energy operator and then imposing a grid in the continuous angular variable ϕ. To this end, let $\psi(\phi)$ be an arbitrary function on the circle and note that its derivative can be approximated as follows for Δ small,

$$\frac{\partial \psi}{\partial \phi} \approx \frac{\psi(\phi+\Delta)-\psi(\phi)}{\Delta} \approx \frac{\psi(\phi)-\psi(\phi-\Delta)}{\Delta} \tag{1.7}$$

$$\Rightarrow \langle \phi|l^2|\psi\rangle = -\frac{\partial^2 \psi}{\partial \phi^2} \approx -\frac{(\psi(\phi+\Delta)+\psi(\phi-\Delta)-2\psi(\phi))}{\Delta^2} \tag{1.8}$$

Now, note that since ψ is a function on the circle, $|\psi\rangle = \sum_m \psi_m |m\rangle \Leftrightarrow \psi(\phi) = \sum_m \psi_m e^{im\phi}$, i.e. $\psi(\phi)$ admits a Fourier series. Expanding $|\psi\rangle$ in this basis yields,

$$\langle \phi|l^2|\psi\rangle \approx -\frac{1}{\Delta^2}\sum_{m=-\infty}^{\infty} \psi_m (e^{im(\phi+\Delta)} + e^{im(\phi-\Delta)} - 2e^{im\phi}) \tag{1.9}$$

Now we define the shift operator τ and its Hermitian conjugate on the circle as follows,

$$\tau|\phi\rangle = |\phi-\Delta\rangle, \quad \tau^+|\phi\rangle = |\phi+\Delta\rangle \Rightarrow \langle\phi|\tau|m\rangle = e^{im(\phi+\Delta)}, \quad \langle\phi|\tau^+|m\rangle = e^{im(\phi-\Delta)} \tag{1.10}$$

Using this, the approximate kinetic energy action becomes (for a small Δ),

$$\langle \phi|l^2|\psi\rangle \approx -\frac{1}{\Delta^2}\sum_{m=-\infty}^{\infty} \psi_m \langle\phi|\tau+\tau^+-2|m\rangle = -\frac{1}{\Delta^2}\langle\phi|\tau+\tau^+-2|\psi\rangle \tag{1.11}$$

Now, imposing a uniform grid with d points in ϕ and setting $\Delta = 2\pi/d$ gives the following approximate form for the kinetic energy operator,

$$\tilde{l}^2 = -\frac{1}{\Delta^2}(\tau^+ + \tau - 2I) \tag{1.12}$$

The discrete basis in this representation is the set $\{|k\rangle \equiv |2\pi k/d\rangle \mid 0 \leq k \leq d-1\}$. Note that ϕ is 2π periodic so for any grid point such that $\phi = 2\pi - \epsilon$ for some $0 \leq \epsilon < \Delta$, $\tau^+|2\pi - \epsilon\rangle = |\Delta - \epsilon\rangle$ and $\tau|\Delta - \epsilon\rangle = |2\pi - \epsilon\rangle$. Therefore, the shift operators in the grid representation are cyclic and have the following matrix elements,

$$\tau_{ij} = \delta_{i,i+1}, \quad \tau^+_{ij} = \delta_{j+1,j} \tag{1.13}$$

Here, the addition in the above Kronecker delta operators is modulo d to allow for the cyclic shift property. The diagonal interaction term can similarly be approximated by evaluation on the ϕ grid. Moreover, we can represent the interaction for a chain of planar rotors in terms of the clock matrices σ and σ^+, the discrete Fourier transforms of the shift matrices τ and τ^+. The matrix elements of these operators are,

$$\sigma_{jk} = e^{-i2\pi j/d}\delta_{jk}, \quad \sigma^+_{jk} = e^{i2\pi j/d}\delta_{jk} \tag{1.14}$$

To see this, note that we can express the interaction as follows,

$$\begin{aligned} V_{i,i+1} &= g(\sin(\phi_i)\sin(\phi_{i+1}) - 2\cos(\phi_i)\cos(\phi_{i+1})) \\ &= -\frac{g}{4}(e^{i\phi_i} - e^{-i\phi_i})(e^{i\phi_{i+1}} - e^{-i\phi_{i+1}}) - \frac{g}{2}(e^{i\phi_i} + e^{-i\phi_i})(e^{i\phi_{i+1}} + e^{-i\phi_{i+1}}) \end{aligned} \tag{1.15}$$

The operator $e^{i\phi}$ agrees with σ^+ on the grid: $e^{i\phi}|2\pi k/d\rangle = e^{i2\pi k/d}|2\pi k/d\rangle \equiv \sigma^+|k\rangle$. Using this identification, the interaction operator becomes,

$$V_{i,i+1} = -\frac{3g}{4}(\sigma_i^+\sigma_{i+1}^+ + \sigma_i\sigma_{i+1}) - \frac{g}{4}(\sigma_i^+\sigma_{i+1} + \sigma_i\sigma_{i+1}^+) \tag{1.16}$$

We will often refer to this as the clock and shift representation of the Hamiltonian. Since this discretization relies on using finite differences, it requires a large number of grid points for convergence. The existence of grid representations that converge much faster typically makes the finite difference approach a poor choice for computational studies. However, the simple form of the resulting Hamiltonians can be useful for theoretically analyzing the nature of critical points in systems with a specific symmetry. An example of this can be

found in Ref. 30 where the connection between the clock and shift representation and the continuous rotor analogue is exploited in a field theory context to investigate the phase diagram of the $\mathbb{Z}_d$ chain. For this thesis, the clock and shift representation of the rotor Hamiltonian will be useful in the next subsection when we construct the $\mathbb{Z}_2$ planar rotor chain as a generalization of the TFIM. That connection will then be leveraged in chapter 4 to propose a possible Stochastic Series Expansion (SSE) QMC approach for the $\mathbb{Z}_2$ chain.

For the computational studies contained in this thesis, we use the Discrete Variable Representation (DVR) investigated by Meyer (also often referred to as the Colbert-Miller DVR in the literature).[43–45] To construct this representation, we start by restricting ourselves to functions on the circle that can be approximated by a finite Fourier series,

$$\psi(\phi) = \sum_{k=-M}^{M} \psi_k e^{ik\phi} \tag{1.17}$$

Here, we have imposed a momentum cutoff M so that $\psi(\phi)$ is defined exactly by $d = 2M+1$ frequency components. Each of these frequency components ψ_k are given by the discrete Fourier transform of the function ψ evaluated on a grid in ϕ, $\mathcal{G} = \{\phi_l = 2\pi l/d \mid 0 \leq l \leq d-1\}$. This can be seen as follows,

$$\begin{aligned}\frac{1}{d}\sum_{l=0}^{d-1} \psi(\phi_l) e^{-ik\phi_l} &= \frac{1}{d}\sum_{l=0}^{d-1}\sum_{r=-M}^{M} \psi_r e^{ir\phi_l} e^{-ik\phi_l} = \frac{1}{d}\sum_{r=-M}^{M}\sum_{l=0}^{d-1} \psi_r e^{-i(k-r)2\pi l/d} \\ &= \sum_{r=-M}^{M} \psi_r \delta_{rk} = \psi_k \Rightarrow \psi_k = \frac{1}{d}\sum_{l=0}^{d-1} \psi(\phi_l) e^{-ik\phi_l}\end{aligned} \tag{1.18}$$

The sum over l above was evaluated using the finite geometric series with the common ratio $r = e^{-i(k-r)2\pi/d}$. Therefore, to evaluate a function $\psi(\phi)$ of the form given in Eq. (1.17) on $[0, 2\pi)$, we only need to evaluate it on a finite number of points defined by the set $\mathcal{G}$. Given those points, the function at an arbitrary point ϕ is given by,

$$\psi(\phi) = \frac{1}{d}\sum_{k=-M}^{M}\sum_{l=0}^{d-1} \psi(\phi_l) e^{-ik(\phi_l - \phi)} \tag{1.19}$$

Since our functions of interest are entirely determined by their values on the grid $\mathcal{G}$ and because our operators are linear, it is useful to represent the problem using finite dimensional linear algebra; the states are represented by vectors $v_l = \psi(\phi_l)$ and operators as matrices

on the grid. This requires us to represent the circle Laplacian as a matrix as well. To this end, consider the second derivative of a function of the form of Eq. (1.17). The second derivatives of such functions are also compactly supported on the interval $[-M, M]$ in the frequency domain,

$$\psi(\phi) = \sum_{k=-M}^{M} \psi_k e^{ik\phi} \Rightarrow \frac{d^2\psi}{d\phi^2} = \sum_{k=-M}^{M} k^2 \psi_k e^{ik\phi} = \sum_{k=-M}^{M} \tilde{\psi_k} e^{ik\phi} \tag{1.20}$$

Therefore, for any point $\phi \in [0, 2\pi)$, the second derivative can be exactly evaluated by interpolation as well,

$$-\frac{d^2\psi}{d\phi^2} = \frac{1}{d} \sum_{k=-M}^{M} \sum_{l=0}^{d-1} -\frac{d^2\psi}{d\phi^2}\bigg|_{\phi_l} e^{-ik(\phi_l - \phi)} \tag{1.21}$$

Eq. (1.21) implies that the action of the circle Laplacian on a band-limited function at an arbitrary point can be determined by the second derivative of such a function evaluated at the grid points. To determine the matrix representation for this, we can use (1.19) to get,

$$-\frac{d^2\psi}{d\phi^2}\bigg|_{\phi_r} = \sum_{l=0}^{d-1} \left(\frac{1}{d} \sum_{k=-M}^{M} k^2 e^{ik(\phi_r - \phi_l)} \right) \psi(\phi_l) = \sum_{l=0}^{d-1} D_{rl} \psi(\phi_l) \tag{1.22}$$

$$\Rightarrow D_{rl} = \frac{1}{d} \sum_{k=-M}^{M} k^2 e^{ik(\phi_r - \phi_l)} \tag{1.23}$$

Note that we have included a negative sign in the second derivative because we need a DVR representation of the kinetic energy operator for our problem. On the DVR grid, this operator is represented by the matrix D_{rl}. We can compute the sum in Eq. (1.23) analytically for all $0 \leq r, l \leq d-1$. For $r = l$, we get,

$$D_{rl} = -\frac{1}{d} \sum_{k=-M}^{M} k^2 = -\frac{2}{d} \sum_{k=1}^{M} k^2 = -\frac{M(M+1)}{3} \tag{1.24}$$

where in the last line, we have used the sum of squares formula. For $r \neq l$, we can pull out two derivatives with respect to $\Delta\phi = (\phi_r - \phi_l)$ and compute the sum analytically,

$$D_{rl} = -\frac{1}{d} \frac{\partial^2}{\partial \Delta\phi^2} \left(\sum_{k=-M}^{M} e^{ik\Delta\phi} \right) = -\frac{1}{d} \frac{\partial^2}{\partial \Delta\phi^2} \left(e^{-iM\Delta\phi} \sum_{k=0}^{d-1} e^{ik\Delta\phi} \right) \tag{1.25}$$

Noting that the sum is a geometric series, we get,

$$\sum_{k=0}^{d-1} e^{ik\Delta\phi} = \left(\frac{1-e^{id\Delta\phi}}{1-e^{i\Delta\phi}}\right) = \frac{e^{id\Delta\phi/2}}{e^{i\Delta\phi/2}}\left(\frac{e^{-id\Delta\phi/2}-e^{id\Delta\phi/2}}{e^{-i\Delta\phi/2}-e^{i\Delta\phi/2}}\right) \tag{1.26}$$

$$\Rightarrow \sum_{k=0}^{d-1} e^{ik\Delta\phi} = e^{i\Delta\phi M}\frac{\sin(d\Delta\phi/2)}{\sin(\Delta\phi/2)} \Rightarrow D_{rl} = -\frac{1}{d}\frac{\partial^2}{\partial\Delta\phi^2}\left(\frac{\sin(d\Delta\phi/2)}{\sin(\Delta\phi/2)}\right) \tag{1.27}$$

In the above equations, we have used $d = 2M+1$ which implies $e^{i\Delta\phi(d-1)/2} = e^{iM\Delta\phi}$. Evaluating the second derivative of the quotient yields,

$$D_{rl} = \frac{1}{2}\cos(d\Delta\phi/2)\frac{\cos(\Delta\phi/2)}{\sin^2(\Delta\phi/2)} + \frac{d}{4}\frac{\sin(d\Delta\phi/2)}{\sin(\Delta\phi/2)} - \frac{1}{4d}\frac{\sin(d\Delta\phi/2)}{\sin^3(\Delta\phi/2)}\left(\cos(\Delta\phi/2)+1\right) \tag{1.28}$$

Now, using the fact that $\Delta\phi = 2\pi(r-l)/d$, which implies $\cos(d\Delta\phi/2) = \cos(\pi(r-l)) = (-1)^{r-l}$, and $\sin(d\Delta\phi/2) = 0$, we get,

$$D_{rl} = (-1)^{r-l}\frac{\cos(\Delta\phi/2)}{2\sin^2(\Delta\phi/2)} = (-1)^{r-l}\frac{\cos(\pi(r-l)/(2M+1))}{2\sin^2(\pi(r-l)/(2M+1))}, \quad r \neq l \tag{1.29}$$

The DVR potential energy matrix elements can now be obtained by evaluating V on the grid. For a coplanar chain of rotors, this yields,

$$V_{ijkl} = g(\sin(2\pi i/d)\sin(2\pi k/d) - 2\cos(2\pi i/d)\cos(2\pi k/d))\delta_{ij}\delta_{kl} \tag{1.30}$$

We could also have equivalently expressed the matrix elements of V using the exponential operators as done in Eq. (1.15). In both the DVR representation as well as the finite differences grid representation, the potential matrix elements are given by (1.16). The potential has 4 indices since it is a 2-body operator. We can determine the matrix associated with Eq. (1.30) using lexicographic ordering,

$$V_{id+j}^{kd+l} = V_{ijkl}, \tag{1.31}$$

$$\Rightarrow\ V_n^m = V_{n_1,n_2,m_1,m_2},\ n_1 = \lfloor n/d \rfloor,\ n_2 = n\%d,\ m_1 = \lfloor m/d \rfloor,\ n_2 = n\%d \tag{1.32}$$

It is instructive at this point to briefly discuss the different sources of error in the DVR representation. The first approximation is of course the assumption that all states of interest have a compactly supported spectrum in the range $[-M, M]$. Given this, the kinetic energy operator is exact in this representation since we can re-construct the second

derivative of such functions exactly for any $\phi \in [0, 2\pi)$, given $\psi(\phi_l)$ for all $\phi_l \in \mathcal{G}$, using Eqs. (1.21) and (1.22) and the definition of the matrix D_{rl}. However, the potential energy operator does change the spectrum of our band-limited functions. This can be seen by applying the operator $e^{i\hat{\phi}}$ (since our potential can be constructed using combinations of exponential operators) on such a function,

$$\begin{aligned}\varphi(\phi) = e^{i\hat{\phi}}\psi(\phi) &= \sum_{k=-M}^{M} \psi_k e^{i(k+1)\phi} = \sum_{k=-M+1}^{M+1} \psi_{k-1} e^{ik\phi} \\ &= \sum_{k=-M+1}^{M} \psi_{k-1} e^{ik\phi} + \psi_M e^{i(M+1)\phi} \end{aligned} \tag{1.33}$$

Note that the frequency spectrum of $\varphi(\phi)$ is still compactly supported but the interval is $[-M+1, M+1]$ now. However, if $\phi = \phi_l$ is a grid point, we can re-express the term corresponding to $k = M+1$ in the last sum as follows,

$$\psi_M e^{i(M+1)\phi_l} = \psi_M e^{i(M+1+M-M)\phi_l} = \psi_M e^{-iM\phi_l} e^{id\phi_l} = \psi_M e^{-iM\phi_l} \tag{1.34}$$

Therefore, for the grid points in $\mathcal{G}$, the extra phase on the last term cancels and we can re-write the action,

$$e^{i\hat{\phi}_l}\psi(\phi_l) = \sum_{k=-M}^{M} \psi_{k-1} e^{ik\phi_l} \tag{1.35}$$

Here, we have used the fact that $\psi_{k-d} = \psi_{k+d} = \psi_k$ with $k = M$, which can be seen as follows,

$$\psi_{k\pm d} = \frac{1}{d}\sum_{l=0}^{d-1} \psi(\phi_l) e^{i(k\pm d)\phi_l} = \frac{1}{d}\sum_{l=0}^{d-1} \psi(\phi_l) e^{ik\phi_l} = \psi_k \tag{1.36}$$

As a consequence, $\psi_M = \psi_{M-d} = \psi_{-M-1}$. Eq. (1.35) implies that restricted to the grid, the action of the operator $e^{i\hat{\phi}}$ is to shift all the frequency components $k \in [-M, M-1]$ up by 1 and wrap around the final frequency component ψ_M and map it to $k = -M$. Therefore, on the grid $\mathcal{G}$, the action of the potential operators is fully encapsulated by the DVR representation. But, unlike in the case of $\hat{l}^2\psi(\phi)$, we cannot recover $e^{i\hat{\phi}}\psi(\phi)$ by interpolation exactly. To see this, consider the approximation yielded by the interpolation formula (Eq. (1.19)) for $e^{i\hat{\phi}}\psi(\phi)$,

$$\tilde{\varphi}(\phi) = \frac{1}{d}\sum_{k=-M}^{M}\sum_{l=0}^{d-1} (e^{i\hat{\phi}}\psi)\big|_{\phi_l} e^{-ik(\phi_l - \phi)} = \sum_{k=-M}^{M} \psi_{k-1} e^{ik\phi} \tag{1.37}$$

Now, subtracting φ and $\tilde{\varphi}$, we get,

$$\varphi(\phi) - \tilde{\varphi}(\phi) = \psi_M(e^{-iM\phi} - e^{i(M+1)\phi}) \neq 0 \tag{1.38}$$

Similar arguments can be made for a general potential to show that the higher frequency components lead to errors uncontrolled by the grid spacing. This issue is circumvented in ground state simulations by picking a large enough M such that states near the momentum cutoff M do not appreciably affect the ground state of the system.[43,46]

In our work, we will use the DVR representation of the Hamiltonian to calculate expectation values in our simulations. Therefore, it is instructive to examine the error contributions to the Hamiltonian matrix elements directly. For the kinetic energy matrix elements, the error arises due to the truncation of the basis set to $[-M, M]$. This error is typically referred to as the variational error in the DVR.[46] The potential matrix elements are subject to this variational error as well as an additional quadrature error.[46]

To make this quadrature error for the present case precise, let us again use the example of the operator $e^{i\hat{\phi}}$. The matrix elements of this operator in the DVR are given by the clock matrix specified in Eq. (1.14). Now, if we discrete Fourier transform this matrix, we get the shift operator given in Eq. (1.13). The discrete Fourier transformed representation of the problem is typically referred to as the Finite Basis Representation (FBR) and is unitarily equivalent to the DVR.[46] To determine the error, we can compare the FBR matrix elements of $e^{i\hat{\phi}}$ to their exact counterparts given by,

$$\langle m|e^{i\phi}|m'\rangle = \frac{1}{2\pi}\int_0^{2\pi} d\phi\ e^{i(m-m'+1)\phi} = \delta_{m,m'-1} \tag{1.39}$$

The representation that uses exact matrix elements for both the kinetic and the potential energy operators (up to basis truncation) is typically referred to as the Variational Basis Representation (VBR).[46] In the above exact case, the Kronecker delta indices are not determined modulo d which means that the VBR corresponds to the linear shift operator. Therefore, the quadrature error in the DVR for our problem is associated with the use of the circulant shift operator from Eq. (1.13) in the FBR. Both the quadrature and the variational errors contribute to the polynomial interpolation error exhibited in Eq. (1.38). Since these errors are all largely restricted to the higher frequency components, using a sufficiently large momentum cutoff insulates our calculations when we compute ground state expectation values.

It is also important to highlight that the linear shift operator (which corresponds to the VBR) is not typically used to construct a grid representation of the potential in the position representation because the associated potential matrix would not be diagonal. This can be seen by explicitly evaluating the discrete Fourier transform of the linear shift operator (denoted $\tilde{\tau}$ below),

$$\mathcal{F}(\tilde{\tau}_{rl})_{nm} = \frac{1}{d}\sum_{r,l=0}^{d-1} e^{in\phi_l} e^{-im\phi_r}\delta_{l,r-1} = \frac{1}{d}\sum_{r=1}^{d-1}\sum_{l=0}^{d-1} e^{in\phi_l} e^{-im\phi_r}\delta_{l,r-1} \tag{1.40}$$

$$\Rightarrow \mathcal{F}(\tilde{\tau}_{rl})_{nm} = \frac{1}{d}\left(\sum_{r=1}^{d-1} e^{i(n-m)2\pi r/d}\right) e^{-i2\pi n/d} = (\delta_{nm}-1)e^{-i2\pi n/d} \tag{1.41}$$

Note that in the linear shift, because the first row is the zero vector, the sum over r starts at $r = 1$ as shown in Eq. (1.40). In contrast, the circulant shift does not have a zero vector which yields an (exactly diagonal) Kronecker delta term instead of the right side of Eq. (1.41).

Since the finite difference approach introduced at the beginning of this subsection has the same potential matrix elements, these variational and quadrature errors are also reflected in that technique. Moreover, the finite difference approach has an additional layer of approximation built into it as can be seen by comparing the kinetic energy matrices of the two representations in the momentum basis. To see this, we can discrete Fourier transform Eq. (1.23) and Eq. (1.12),

$$\mathcal{F}(D_{rl})_{nm} = \frac{1}{d}\sum_{r,l=0}^{d-1} e^{in\phi_l} e^{-im\phi_r}\left(\frac{1}{d}\sum_{k=-M}^{M} k^2 e^{-ik(\phi_l-\phi_r)}\right) = n^2\delta_{nm} \tag{1.42}$$

$$\mathcal{F}(\tau_{rl})_{nm} = \frac{1}{d}\sum_{r,l=0}^{d-1} e^{in\phi_l} e^{-im\phi_r}\delta_{r,l+1} = e^{-im2\pi/d}\delta_{nm} \tag{1.43}$$

$$\Rightarrow \mathcal{F}\left(\tilde{l}^2\right)_{nm} = -\frac{1}{\Delta^2}(e^{-in2\pi/d} + e^{in2\pi/d} - 2)\delta_{nm} = -\frac{2}{\Delta^2}\left(\cos\left(\frac{2\pi n}{d}\right) - 1\right)\delta_{nm} \tag{1.44}$$

Note that here, $-M \leq n, m \leq M$. It can be seen from Eqs. (1.42) and (1.44) that the finite difference approach approximates the n^2 on the diagonals of the kinetic energy operator in the momentum representation, by $\alpha(\cos(2\pi n/d) - 1)$. Here α depends on the number of grid points $d = 2M + 1$. Taylor expanding Eq. (1.44) recovers the n^2 term we

are approximating,

$$\mathcal{F}\left(\tilde{l}^2\right) \approx -\frac{2}{\Delta^2}\left(-\frac{1}{2!}n^2\Delta^2 + \frac{1}{4!}n^4\Delta^4 + ...\right)\delta_{nm} = (n^2 + \mathcal{O}(\Delta^2))\delta_{nm} \tag{1.45}$$

The error in Eq. (1.45) is only controlled by Δ in the entries closer to the middle of the matrix. As $\Delta \to 0$, $M \to \infty$ and for the boundary terms, the argument of the cosine is $M\Delta$ which does not become small.

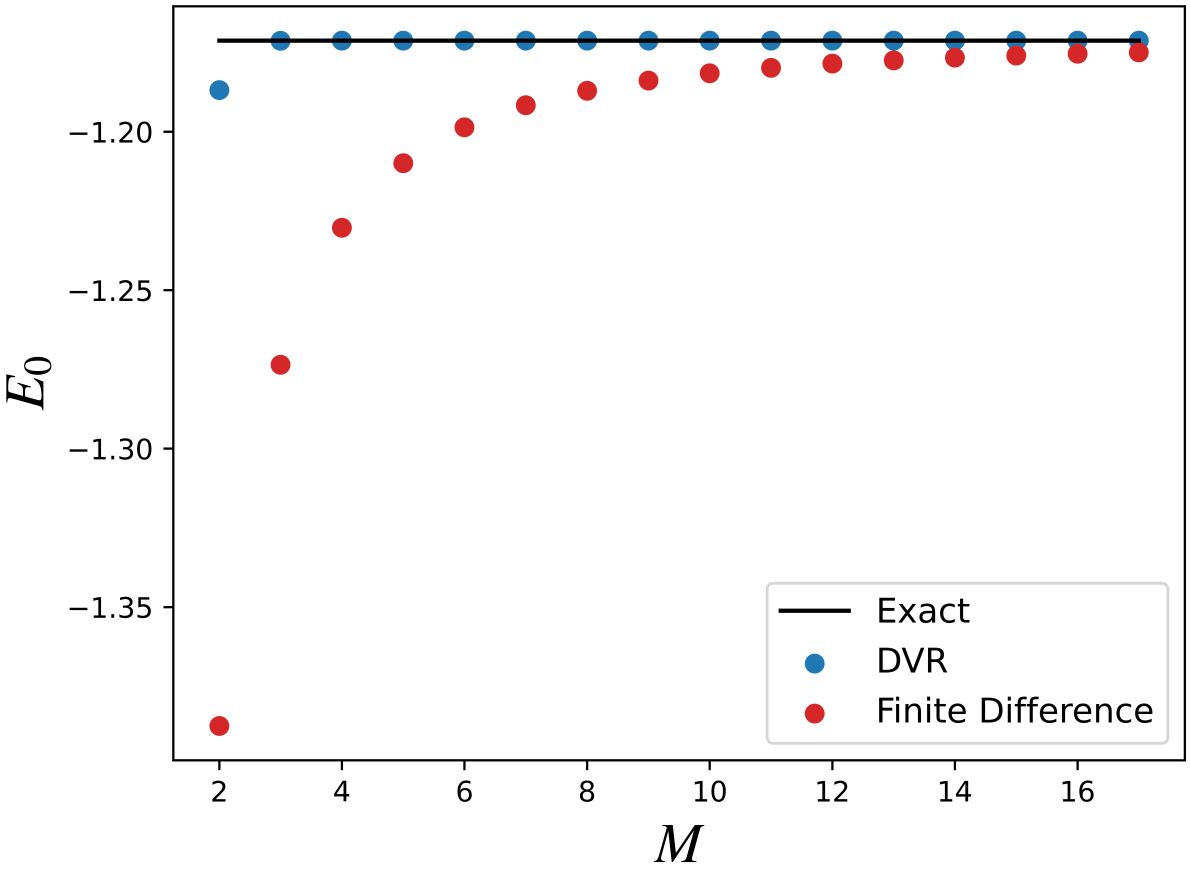


Figure 1.1: Convergence of the ground state energy computed using sparse diagonalization, for $N = 3$ $g = 1.0$ as M is increased, when using the DVR and the finite difference (clock and shift representation) discretizations. The exact energy is computed using the DVR approach via diagonalization with $M = 17$.

However, as discussed above, in ground state simulations, we must pick M large enough such that ground state properties are unaffected by states close to $-M$ and M to minimize errors associated with the potential matrix elements. The same approach can be used to circumvent the additional errors associated with the kinetic energy operator in the clock and shift representation of the problem. These larger error contributions imply that convergence in the clock and shift representation is, by construction, much slower than in the DVR representation. As an example, Fig. 1.1 shows the convergence of the ground state energy for a coplanar chain with $N = 3$ rotors ($g = 1.0$) computed using both discretization schemes as a function of M. We need $M > 16$ to converge with the clock and shift representation while $M = 4$ is sufficient with the DVR approach.

1.1.3 Planar Rotor Lattices From The Transverse Field Ising Model

In this subsection, we show how the clock and shift representation of the planar rotor chain Hamiltonian introduced in subsection 1.1.2 can be recovered by generalizing the TFIM. To this end, consider the Hamiltonian of the nearest neighbor TFIM,[4,6]

$$H = A\sum_{i=1}^{N-1}\sigma_i^z\sigma_{i+1}^z + B\sum_{i=1}^{N}\sigma_i^x \tag{1.46}$$

Here, σ^z and σ^x are the Z and X Pauli matrices respectively. Since σ^z and σ^x are both hermitian, we can re-express H as follows,

$$H = \frac{A_1}{4}\sum_{i=1}^{N-1}(\sigma_i^z\sigma_{i+1}^z + \sigma_i^{z,+}\sigma_{i+1}^{z,+}) + \frac{A_2}{4}\sum_{i=1}^{N-1}(\sigma_i^{z,+}\sigma_{i+1}^z + \sigma_i^z\sigma_{i+1}^{z,+}) + \frac{B}{2}\sum_{i=1}^{N}(\sigma_i^x + \sigma_i^{x,+}) \tag{1.47}$$

with $A_1 = A_2$. Here, $\sigma^{k,+}$ is the Hermitian conjugate of σ^k for $k \in \{x, z\}$. One possible generalization of Pauli matrices can be constructed by retaining the following properties of σ^x and σ^z,[31]

$$(\sigma^z)_{nm} = \delta_{nm}e^{i2\pi n/d}, \quad \sigma^x = F_d\sigma^z F_d^+, \quad (\sigma^z)^d = (\sigma^x)^d = I, \quad \sigma^z\sigma^x = e^{2i\pi/d}\sigma^x\sigma^z \tag{1.48}$$

Here, $(\sigma^z)_{nm}$ is the matrix element of σ^z corresponding to the nth row and mth column and $d = 2$. $F_d = F_2$ is the Hadamard transform defined by the matrix,[47]

$$F_2 = \frac{1}{\sqrt{d}}\begin{pmatrix}1 & 1\\ 1 & -1\end{pmatrix} = \frac{1}{\sqrt{d}}\begin{pmatrix}1 & 1\\ 1 & e^{2\pi i(d-1)/d}\end{pmatrix} \tag{1.49}$$

Noting that F_2 coincides with the discrete Fourier transform in 2 dimensions, we can increase d while preserving Eq. (1.48) to get $\sigma^z \to \sigma$, the clock matrix in d dimensions, $\sigma^x \to \tau$, the shift matrix in d dimensions.[31] For larger d, $F_2 \to F_d = F$, the discrete Fourier transform in Eq. (1.48). Now, using this generalization, the Hamiltonian in Eq. (1.47) becomes ($H(\sigma^z, \sigma^x) \to H(\sigma, \tau)$),

$$H(\sigma, \tau) = \frac{A_1}{4} \sum_{i=1}^{N-1} (\sigma_i \sigma_{i+1} + \sigma_i^+ \sigma_{i+1}^+) + \frac{A_2}{4} \sum_{i=1}^{N-1} (\sigma_i^+ \sigma_{i+1} + \sigma_i \sigma_{i+1}^+) + \frac{B}{2} \sum_{i=1}^{N} (\tau_i + \tau_i^+) \quad (1.50)$$

Setting $A_1 = -\frac{3g}{4}$, $A_2 = -\frac{g}{4}$, and $B = -\frac{1}{\Delta^2}$, we recover the coplanar rotor chain Hamiltonian in the clock and shift representation (Eqs. (1.12), (1.16)) with a constant energy offset,

$$H_{\mathbb{Z}_2} = H(\sigma, \tau) + \frac{2N}{\Delta^2} \quad (1.51)$$

$H_{\mathbb{Z}_2}$ here is the coplanar rotor chain Hamiltonian in the finite difference approximation. This construction is interesting from the perspective of QMC simulations. Typical PIMC approaches for simulating the rotor chain problem rely on single particle moves. However, near criticality, this becomes insufficient as the system suffers from critical slowing down.[21] For spin systems, this issue is generally resolved by implementing global moves; transitions that allow multiple spins to flip in the same iteration which leads to faster convergence.[48,49] In particular for the TFIM, it is relatively easy to implement global moves via the SSE algorithm.[50] This connection between the TFIM and the quantum clock model offers a potential path towards developing a SSE approach for the quantum rotor chain problem as well. We briefly discuss one potential scheme for constructing a SSE algorithm for the $\mathbb{Z}_2$ chain in chapter 4.

1.2 Quantum Statistical Mechanics of Planar Rotations

In this section, we first introduce our imaginary-time path integral formalism for planar rotors.[18,51] While the theoretical construction assumes finite temperatures, using a sufficiently low temperature or a slight variation of the usual PIMC framework called Path Integral Ground State (PIGS) allows us to compute ground state properties.[11,16,52] Following this we derive the PIGS estimators that we use for our computational studies in

chapter 2. We conclude this section by discussing the theory of quantum phase transitions in the context of the $\mathbb{Z}_2$ rotor chain.[3,19]

1.2.1 Imaginary-Time Path Integrals

At a finite temperature T, the statistical mechanics of our system is described by the canonical ensemble,[6,11]

$$Z = \mathrm{Tr}(\rho), \quad \rho = e^{-\beta H}, \quad \tilde{\rho} = \frac{1}{Z} e^{-\beta H} \tag{1.52}$$

where Z is the partition function, $\tilde{\rho}$ is the density matrix, and $\beta = 1/k_b T$ is the reciprocal temperature. k_b is the Boltzmann constant which we will always set to 1 since we use natural units. Operator expectation values for an ensemble at temperature T can be computed as follows,[6,11]

$$\langle O \rangle = \mathrm{Tr}(\tilde{\rho}\ O) = \frac{1}{Z} \mathrm{Tr}(e^{-\beta H} O) \tag{1.53}$$

where O is some arbitrary operator defining a property of interest such as the Hamiltonian (for energy), the correlation function or the net polarization of our chain of rotors in the presence of an external field. For simplicity, we will use the partition function (Eq. (1.52)) to construct our path integral. Then, we will derive the relevant estimators in the context of PIGS in the next section since we are interested in ground state properties. To this end, note that we can resolve the trace in the position representation,

$$Z = \int d\boldsymbol{\phi}\ \rho(\boldsymbol{\phi}, \boldsymbol{\phi}, \beta), \quad \rho(\boldsymbol{\phi}, \boldsymbol{\phi}, \beta) = \langle \boldsymbol{\phi} | e^{-\beta H} | \boldsymbol{\phi} \rangle \tag{1.54}$$

Here, $\boldsymbol{\phi} = (\phi^1, ..., \phi^N)$ is the N rotor configuration, the integral is over N circles: $(S^1)^N$, and $\rho(\boldsymbol{\phi}, \boldsymbol{\phi}, \beta)$ represents the diagonal matrix elements of $e^{-\beta H}$. Evaluating Z or $\rho(\boldsymbol{\phi}, \boldsymbol{\phi}, \beta)$ exactly is intractable for large systems since that would require diagonalizing the many-body Hamiltonian.[53] Therefore, we proceed by using the convolution property of the propagator ρ,

$$e^{-\beta H} = (e^{-\tau H})^P, \quad \tau = \beta / P \tag{1.55}$$

$$\Rightarrow \rho(\boldsymbol{\phi}_0, \boldsymbol{\phi}_P, \beta) = \langle \boldsymbol{\phi}_0 | e^{-\beta H} | \boldsymbol{\phi}_P \rangle = \int d\vec{\boldsymbol{\phi}}_{P-1} \prod_{i=0}^{P-1} \rho(\boldsymbol{\phi}_i, \boldsymbol{\phi}_{i+1}, \tau) \tag{1.56}$$

In the second line above, we have inserted $P-1$ resolutions of identity (one between each factor of $e^{-\tau H}$) and denoted the resulting measure $d\vec{\boldsymbol{\phi}}_{P-1} = d\boldsymbol{\phi}_1 ... d\boldsymbol{\phi}_{P-1}$. These extra integration variables are often referred to as beads. For τ small, we can use the (symmetric) Trotter factorization,[54,55]

$$e^{-\tau H} = e^{-\tau V/2} e^{-\tau K} e^{-\tau V/2} + \mathcal{O}(\tau^3) \tag{1.57}$$

where $H = K + V$, K is the kinetic energy operator and V is the potential operator. For the matrix elements of ρ, this implies,

$$\rho(\boldsymbol{\phi}, \boldsymbol{\phi}') = \rho_K(\boldsymbol{\phi}, \boldsymbol{\phi}', \tau) \rho_V(\boldsymbol{\phi}, \tau/2) \rho_V(\boldsymbol{\phi}', \tau/2) + \mathcal{O}(\tau^3) \tag{1.58}$$

$$\rho_K(\boldsymbol{\phi}, \boldsymbol{\phi}', \tau) = \langle \boldsymbol{\phi} | e^{-\tau K} | \boldsymbol{\phi}' \rangle, \quad \rho_V(\boldsymbol{\phi}, \tau/2) = e^{-\tau V(\boldsymbol{\phi})/2} \tag{1.59}$$

Here, we have used the fact that V is diagonal in the position representation to pull out factors of $e^{-\tau V/2}$ from the inner product. We can further factor the free propagator ρ_K by noting that the many-body kinetic energy operator K is a sum of one-body terms,

$$K = \sum_{j=1}^{N} K_i \Rightarrow \rho(\boldsymbol{\phi}, \boldsymbol{\phi}', \tau) = \prod_{j=1}^{N} \rho_K^j(\phi^j, \phi'^j, \tau) = \prod_{j=1}^{N} \langle \phi^j | e^{-\tau K_j} | \phi'^j \rangle \tag{1.60}$$

Similarly, the term corresponding to the potential in Eq. (1.58) can also be factored,

$$V = \sum_{j=1}^{N-1} V_{i,i+1} \Rightarrow \rho_V(\boldsymbol{\phi}, \tau/2) = \prod_{j=1}^{N-1} \rho_V^j(\phi^j, \phi^{j+1}, \tau/2) = \prod_{j=1}^{N-1} e^{-\tau V_{j,j+1}(\phi^j, \phi^{j+1})/2} \tag{1.61}$$

Collecting all the factorizations in Eq. (1.56) and taking the limit of $P \to \infty$ so that the Trotter error vanishes, we get our imaginary-time path integral form of the density,[11,56]

$$\begin{aligned} \rho(\boldsymbol{\phi}, \boldsymbol{\phi}', \beta) = \lim_{P \to \infty} \int d\vec{\boldsymbol{\phi}}_{P-1} \prod_{i=0}^{P-1} \Bigg(\prod_{j=1}^{N} \rho_K^j(\phi_i^j, \phi_{i+1}^j, \tau) \\ \times \prod_{j=1}^{N-1} \rho_V^j(\phi_i^j, \phi_i^{j+1}, \tau/2) \rho_V^j(\phi_{i+1}^j, \phi_{i+1}^{j+1}, \tau/2) \Bigg) \end{aligned} \tag{1.62}$$

Here, we have used the notation $\boldsymbol{\phi} = \boldsymbol{\phi}_0$ and $\boldsymbol{\phi}' = \boldsymbol{\phi}_P$. While we used the symmetric Trotter approximation in this construction, it should be noted that we could also have used other factorizations.[57–59] In particular, we analyze the pair approximation in the next

chapter which, while more involved, yields faster convergence.[11,60] Using Eq. (1.62) for ρ in Eq. (1.54) and imposing the constraint $\boldsymbol{\phi}_0 = \boldsymbol{\phi}_P$, we can express our partition function in path integral form as well,[11,18]

$$Z = \lim_{P\to\infty} \int d\vec{\boldsymbol{\phi}}_P \prod_{i=0}^{P-1} \left(\prod_{j=1}^{N} \rho_K^j(\phi_i^j, \phi_{i+1}^j, \tau) \prod_{j=1}^{N-1} \rho_V^j(\phi_i^j, \phi_i^{j+1}, \tau/2) \rho_V^j(\phi_{i+1}^j, \phi_{i+1}^{j+1}, \tau/2) \right) \tag{1.63}$$

Up till now, our derivation has been largely system agnostic; we need only change the bounds of the path integral to recover the case of translational motion,[11,56]

$$\begin{aligned} \rho(\boldsymbol{x}, \boldsymbol{x}', \beta) = \lim_{P\to\infty} \int_{\mathbb{R}^{N(P-1)}} d\vec{\boldsymbol{x}}_{P-1} \prod_{i=0}^{P-1} \Bigg(\prod_{j=1}^{N} \rho_K^j(x_i^j, x_{i+1}^j, \tau) \\ \times \prod_{j=1}^{N-1} \rho_V^j(x_i^j, x_i^{j+1}, \tau/2) \rho_V^j(x_{i+1}^j, x_{i+1}^{j+1}, \tau/2) \Bigg) \end{aligned} \tag{1.64}$$

However, unlike rotations, for translations, the free propagator ρ_K^j is a Gaussian with a variance proportional to the imaginary time τ,[11,16]

$$\rho_K^j(x^j, x'^j, \tau) = \langle x^j | e^{-\tau K} | x'^j \rangle = \frac{1}{2\pi} \int_{\mathbb{R}} dp \; e^{-\tau p^2} e^{ip(x^j - x'^j)} = \frac{1}{\sqrt{4\pi\tau}} e^{-\frac{1}{4\tau}(x^j - x'^j)^2} \tag{1.65}$$

where we have set $m = \frac{1}{2}$ for simplicity like we do for the moment of inertia I in the case of circular motion. It is instructive to use translational motion as an example to develop some intuition for imaginary-time path integrals before deriving the free propagator for rotations.

To this end, note that the Gaussian form of the free propagator is suggestive of a probabilistic interpretation; it represents the diffusive displacement of a classical particle in time τ.[11,61] If we assume that $\rho_K(x_i, x_i', \tau)$ is proportional to the probability of a particle moving from x_i to x_i' in time τ, then the product over factors ρ_K^j for $j \in \{0, ..., P-1\}$ in Eq. (1.64) is the probability of that particle following some trajectory $x(\tau)$ such that $x(j\tau) = x_j$ (up to a normalization factor). Then, taking the limit of $P \to \infty$ while holding $\beta = \tau P$ constant is equivalent to considering finer and finer partitions of the time interval: $[0, \beta]$ until we reach the continuum limit.[11,56] Moreover, integrating over all possible values of the configuration variable (x for translational motion) at each bead index $i \in \{1, ..., P-1\}$ as $P \to \infty$ is equivalent to integrating over all possible paths this particle can follow in going

from x to x' in time β.[56,61] We can determine the normalization factor in this statistical construction by integrating the probability of a given path, over all possible paths starting at x and ending at x',

$$A = \int dx(\tau) P(x(\tau)) = \lim_{P\to\infty} \int dx_1 ... dx_{P-1} \prod_{i=0}^{P-1} \rho_K(x_i, x_{i+1}, \tau) \tag{1.66}$$

$$= \lim_{\tau\to 0} \int dx_1 ... dx_{P-1} \prod_{i=0}^{P-1} \langle x_i | e^{-\tau K} | x_{i+1} \rangle = \langle x | e^{-\beta H} | x' \rangle = \rho_K(x, x', \beta) \tag{1.67}$$

In the above calculation $dx(\tau)$ is the measure indicating an integration over all possible paths denoted $x(\tau)$ between $x(0) = x$ and $x(\beta) = x'$. The integrations over each variable can be done by expanding out the product and recognizing that each factor of $e^{-\tau K}$ is separated by a resolution of identity in the position basis. Since x_0 and x_P are fixed to be x and x' respectively and the limit represents taking finer partitions of the paths $x(t)$, the resulting function $\rho_K(x_0, x_P, \beta) = \rho_K(x, x', \beta)$ is unaffected by the limit of $P \to \infty \Leftrightarrow \tau \to 0$ which gives $\lim_{\tau\to 0} \rho_K(x, x', \beta) = \rho_K(x, x', \beta)$. Dividing both sides of Eq. (1.64) by this normalization (for each particle) gives us the statistical interpretation of our imaginary time path integral in the form of the Feynman-Kac theorem,[11,62]

$$\frac{\rho(\boldsymbol{x}, \boldsymbol{x'}, \beta)}{\rho_K(\boldsymbol{x}, \boldsymbol{x'}, \beta)} = \lim_{P\to\infty} \int_{\mathbb{R}^{N(P-1)}} d\vec{\boldsymbol{x}}_{P-1} P(\boldsymbol{x}_0, ..., \boldsymbol{x}_P) e^{-\frac{\tau}{2}\sum_{i=0}^{P-1}(V(\boldsymbol{x}_i)+V(\boldsymbol{x}_{i+1}))} \tag{1.68}$$

$$= \int_{\boldsymbol{x}(0)=\boldsymbol{x}}^{,\boldsymbol{x}(\beta)=\boldsymbol{x}'} d\boldsymbol{x}(\tau) P(\boldsymbol{x}(\tau)) e^{-\int_0^\beta V(\boldsymbol{x}(\tau))d\tau} = \left\langle e^{-\int_0^\beta V(\boldsymbol{x}(\tau))d\tau} \right\rangle \tag{1.69}$$

Here, angled brackets denote averaging over all Brownian paths. The distribution of these paths is given by the limit as $P \to \infty$ of the translational diffusion processes for each particle,[61,62]

$$P(\boldsymbol{x}(\tau)) = \prod_{j=1}^{N} P(x^j(\tau)) = \prod_{j=1}^{N} \frac{1}{\rho_K(x^j, x'^j, \beta)} \lim_{P\to\infty} \prod_{i=0}^{P-1} \rho_K(x_i^j, x_{i+1}^j, \tau) \tag{1.70}$$

The Feynman-Kac theorem and the theory of Brownian motion can also be constructed for manifolds other than $\mathbb{R}$ albeit with a different free particle transition probability.[63] For planar rotations, since the momenta are discrete, the free propagator is given by,

$$\rho_K(\phi^j, \phi'^j, \tau) = \frac{1}{2\pi} \sum_{m=-\infty}^{\infty} e^{-\tau m^2} e^{-im(\phi^j - \phi'^j)} \tag{1.71}$$

This free rotor density can be expressed as a sum over displaced Gaussians using the Poisson summation formula.[64–66] To see this, note that,

$$\rho_K(\phi^j, \phi'^j, \tau) = \frac{1}{2\pi} \sum_{m=-\infty}^{\infty} \int_{-\infty}^{\infty} e^{-\tau x^2 - ix\Delta\phi^j} \delta(x-m) dx \tag{1.72}$$

Here, we have simply introduced an integral with a delta function in the free propagator equation and defined $\Delta\phi^j = \phi^j - \phi'^j$. Since the delta function is the only component that depends on m, we can re-express the above as follows,

$$\rho_K(\phi^j, \phi'^j, \tau) = \frac{1}{2\pi} \int_{-\infty}^{\infty} e^{-\tau x^2 - ix\Delta\phi^j} \left(\sum_{m=-\infty}^{\infty} \delta(x-m) \right) dx \tag{1.73}$$

The function in the parentheses is the Dirac comb which we denote $f(x)$.[66] It is a periodic function with period 1,

$$f(x+1) = \sum_{k=-\infty}^{\infty} \delta(x+1-k) = \sum_{k=\infty}^{\infty} \delta(x-k) = f(x) \tag{1.74}$$

Therefore, it admits a Fourier series,

$$f(x) = \sum_{k=-\infty}^{\infty} f_k e^{-i2\pi kx} \tag{1.75}$$

We can express the coefficients f_k using the usual Fourier relation,

$$\int_{-1/2}^{1/2} f(x) e^{i2\pi lx} dx = \sum_{k=-\infty}^{\infty} f_k \int_{-1/2}^{1/2} e^{-i2\pi(k-l)x} dx = \sum_{k=-\infty}^{\infty} f_k \delta_{kl} = f_l \tag{1.76}$$

$$\Rightarrow f_l = \int_{-1/2}^{1/2} f(x) e^{i2\pi lx} dx \tag{1.77}$$

Using this with the definition of the Dirac comb, we get,

$$f_k = \sum_{m=-\infty}^{\infty} \int_{-1/2}^{1/2} \delta(x-m) e^{i2\pi kx} dx = \int_{-1/2}^{1/2} \delta(x) e^{i2\pi kx} dx = 1 \tag{1.78}$$

$$\Rightarrow f(x) = \sum_{k=-\infty}^{\infty} e^{-i2\pi kx} \tag{1.79}$$

Now, replacing the Dirac comb in Eq. (1.72) with the Fourier series definition yields the desired form of the free propagator,[67]

$$\begin{aligned}\rho_K(\phi^j, \phi'^j, \tau) &= \frac{1}{2\pi} \sum_{m=-\infty}^{\infty} \int_{-\infty}^{\infty} e^{-\tau x^2 - ix(\Delta\phi^j + 2\pi m)} dx \\ &= \frac{1}{\sqrt{4\pi\tau}} \sum_{m=-\infty}^{\infty} e^{-(\phi^j - \phi'^j + 2\pi m)^2/4\tau} \end{aligned} \tag{1.80}$$

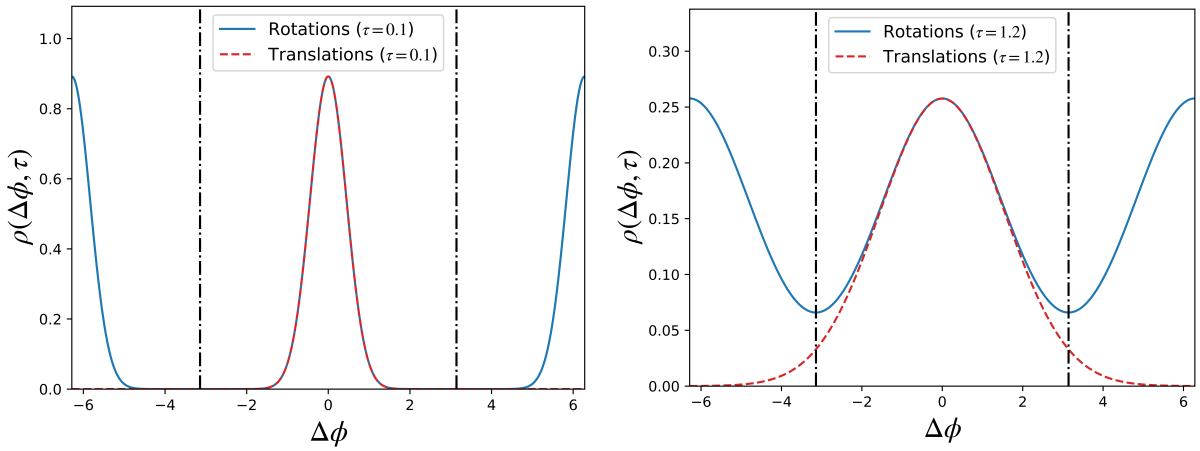


Figure 1.2: Rotational free propagator compared to the translational propagator for $\tau = 0.1$ (left panel) and $\tau = 1.2$ (right panel). The black lines indicate $\Delta\phi = -\pi$ and $\Delta\phi = \pi$. Restricted to this interval, for small τ, the rotational free propagator agrees with the translational free propagator. For larger τ it does not. The peaks at -2π and 2π are a consequence of the periodicity of the rotational propagator. For a circle, displacing by $2\pi - \epsilon$ is the same as displacing by $+\epsilon$ for $-\pi \leq \epsilon \leq \pi$ which is reflected in the additional peaks.

This shows that ρ_K for planar rotations is the periodization of the free propagator for translational motion; a series of Gaussians with variance 2τ displaced by 2π when expressed as a function of $\Delta\phi^j$. In the limit of $\tau \to \infty$, all of these Gaussians will become sufficiently local such that none of these translational propagators significantly affect the value of the rotational propagator in a 2π interval different from the one that contains their mean value, as shown in Fig. 1.2. Consequently, for $\tau << 1$, we can re-express the rotational

free propagator as,

$$\rho_K(\phi^j, \phi'^j, \tau) \approx \frac{1}{\sqrt{4\pi\tau}} e^{-d(\phi^j, \phi'^j)^2/4\tau}, \quad d(\phi^j, \phi'^j) = \min_{k\in\{-1,0,1\}} \{|\phi^j - \phi'^j - 2\pi k|\} \tag{1.81}$$

Here $d(\phi^j, \phi'^j)$ represents the metric (also called the geodesic distance) over polar angles which is simply the acute angle associated with $\Delta\phi^j = \phi^j - \phi'^j$. We use the S^1 metric here since ϕ^j and ϕ'^j are both in the interval $[-\pi, \pi)$ which implies that $\Delta\phi^j$ can take any value in the interval $(-2\pi, 2\pi)$. Therefore, for small τ, the Gaussian that contributes to the probability can be the one centered at $0, 2\pi$ or -2π. All of these cases can be compactly encoded by using the geodesic distance as opposed to the Euclidean distance in $\mathbb{R}$. If we restrict the interval of $\Delta\phi^j$ to be $[-\pi, \pi)$, then we have the following in the limit of $\tau \to 0$,

$$\rho_K(\phi^j, \phi'^j, \tau) \approx \frac{1}{\sqrt{4\pi\tau}} e^{-(\phi^j - \phi'^j)^2/4\tau} \tag{1.82}$$

We use this form in the next chapter while deriving the partial differential equation (PDE) that gives us the Wigner-Kirkwood expansion (also sometimes referred to as the heat kernel expansion or the Seeley-DeWitt expansion) of the propagator.[67–70] Formally, this can be done for PDEs that contain no derivatives or multiplication operators over ϕ'^j by treating ϕ'^j as a parameter and changing variables $\phi^j \to \phi^j + \phi'^j$ so that ϕ^j is in the interval $[\phi'^j - \pi, \phi'^j + \pi)$ (which still covers the full circle).

This construction again alludes to a statistical interpretation of the paths in the imaginary time path integral similar to the case of translational motion. For a particle on the circle with τ small, we recover the diffusive displacement process in the form of Eq. (1.82) with the probability being determined by the shortest distance between the two points in question as before. To construct the Feynman-Kac theorem, we must again treat the general free propagator forms given in Eqs. (1.71) and (1.80) as a transition probability density for a particle on a circle to go from ϕ^j to ϕ'^j in time τ. The product over beads in the limit of $\tau \to 0$ is then proportional to the probability of the particle following a particular continuous path on the circle. The normalization factor can be determined as done for translations in Eq. (1.71). Using this construction, we can now then write down the Feynman-Kac theorem for planar rotations,[11]

$$\frac{\rho(\boldsymbol{\phi}, \boldsymbol{\phi}', \beta)}{\rho_K(\boldsymbol{\phi}, \boldsymbol{\phi}', \beta)} = \lim_{P\to\infty} \int_{(S^1)^{N(P-1)}} d\vec{\boldsymbol{\phi}}_{P-1} P(\boldsymbol{\phi}_0, ..., \boldsymbol{\phi}_P) e^{-\frac{\tau}{2}\sum_{i=0}^{P-1}(V(\boldsymbol{\phi}_i)+V(\boldsymbol{\phi}_{i+1}))} \tag{1.83}$$

$$= \int_{\boldsymbol{\phi}(0)=\boldsymbol{x}}^{,\boldsymbol{\phi}(\beta)=\boldsymbol{\phi}'} d\boldsymbol{\phi}(\tau) P(\boldsymbol{\phi}(\tau)) e^{-\int_0^\beta V(\boldsymbol{\phi}(\tau))d\tau} = \left\langle e^{-\int_0^\beta V(\boldsymbol{\phi}(\tau))d\tau} \right\rangle \tag{1.84}$$

Now, the angled brackets denote averaging over all Brownian paths on a circle as depicted in Fig. 1.3. The distribution of these paths is given by the limit as $P \to \infty$, of the rotational diffusion process for each particle,

$$P(\boldsymbol{\phi}(\tau)) = \prod_{j=1}^{N} P(\phi^j(\tau)) = \prod_{j=1}^{N} \frac{1}{\rho_K(\phi^j, \phi'^j, \beta)} \lim_{P\to\infty} \prod_{i=0}^{P-1} \rho_K(\phi_i^j, \phi_{i+1}^j, \tau) \tag{1.85}$$

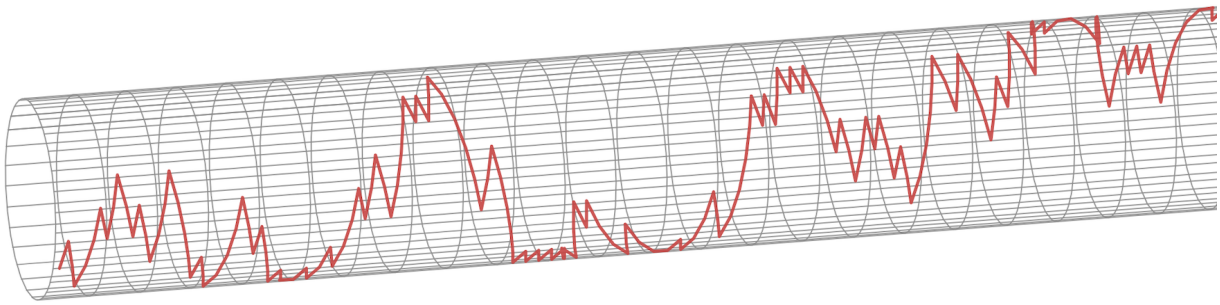


Figure 1.3: Schematic representation of a Brownian path on a circle. The axial direction of the cylinder represents imaginary time. The Weierstrass-like (fractal) appearance of the path emphasizes that the paths are not necessarily smooth.

In the next chapter, we will use this statistical formulation to derive the pair approximation. It is also instructive to mention here that the general theory of probability measures can be used to answer questions about the convergence of the limits as $\tau \to 0 \Leftrightarrow P \to \infty$ which we took for granted in our constructions.[56,71] While rigorous results pertaining to the convergence of imaginary time path integrals given by Brownian motion on $\mathbb{R}$ as well as S^1 have existed for decades, proofs about the convergence of real-time path integral measures (where the propagator is defined using the time-evolution operator instead of the canonical ensemble) are an open problem in mathematical physics.[56] Finally, it is important to note that the resulting paths need not be smooth; the limits of the measures discussed above yield Brownian motion which adheres to everywhere continuous but not necessarily differentiable functions.[11,71]

1.2.2 Path Integral Ground State

While we can use the construction provided in subsection 1.2.1 for ground state simulations (up to the systematic error due to a non-zero temperature T), here we introduce PIGS, a projective variant that has been shown to have better convergence properties in the context of ground state simulations.[16,52] In PIGS, operator expectation values are computed as follows,[16]

$$\langle O\rangle = \frac{1}{Z_0}\langle\Psi_T|e^{-\frac{\beta}{2}H}Oe^{-\frac{\beta}{2}H}|\Psi_T\rangle, \quad Z_0 = \langle\Psi_T|e^{-\beta H}|\Psi_T\rangle \tag{1.86}$$

Here, O is an arbitrary Hermitian operator (we omit the hats for brevity), H is the system Hamiltonian and Z_0 is the normalization which is sometimes also referred to as the pseudo-partition function. β is a projection parameter that will be increased until we converge to the ground state. $|\Psi_T\rangle$ is a trial state that can be picked to benefit convergence as we will see later. It is instructive at this point to show that the operator expectation value is well-defined i.e. that the convergence error when comparing the approximated result to the exact expectation value is bounded. To see this, let us expand the PIGS expectation value in the energy basis (with the assumption that the Hamiltonian is bounded from below and admits a non-trivial discrete spectrum),[16]

$$\langle\Psi_T|e^{-\frac{\beta}{2}H}Oe^{-\frac{\beta}{2}H}|\Psi_T\rangle = \sum_{i,j=0} c_i^* c_j e^{-\frac{\beta}{2}(E_i+E_j)}O_{ij} \tag{1.87}$$

$$= |c_0|^2 e^{-\beta E_0}O_{00} + \sum_{j=1}(c_j + c_j^*)e^{-\frac{\beta}{2}(E_0+E_j)}O_{ij} + \sum_{i,j=1} c_i c_j^* e^{\frac{-\beta}{2}(E_i+E_j)} \tag{1.88}$$

Here, we have used the notation: $O_{ij} = \langle E_i|O|E_j\rangle$ and $c_i = \langle E_i|\Psi_T\rangle$. In the second sum of Eq. (1.88), we have used $O_{ij} = O_{ji}$ since O is assumed to be Hermitian. The pseudo-partition function can also be expanded similarly,

$$\langle\Psi_T|e^{-\beta H}|\Psi_T\rangle = \sum_{i=0}|c_i|^2 e^{-\beta E_i} = |c_0|^2 e^{-\beta E_0} + \sum_{i=1}|c_i|^2 e^{-\beta E_i} \tag{1.89}$$

Dividing Eqs. (1.88) and (1.89) and factoring $e^{-\beta E_0}$ in the numerator and denominator yields,

$$\langle O\rangle = \frac{|c_0|^2 O_{00} + \sum_{j=1}(c_j + c_j^*)e^{-\frac{\beta}{2}(E_j-E_0)}O_{ij} + \sum_{i,j=1}^{N} c_i c_j^* e^{\frac{-\beta}{2}(E_i+E_j-2E_0)}}{|c_0|^2 + \sum_{i=1}|c_i|^2 e^{-\beta(E_i-E_0)}} \tag{1.90}$$

Now, if we take the limit of $\beta \to \infty$, we get the desired convergence to the ground state expectation value assuming $E_i > E_0$ for all $i \geq 1$,

$$\lim_{\beta\to\infty} \langle O \rangle = \frac{|c_0|^2 O_{00}}{|c_0|^2} = \langle E_0|O|E_0\rangle \tag{1.91}$$

This shows that the convergence to the ground state is exponential in β which implies that the systematic error associated with β will quickly decrease to 0 as β is increased.[16] Furthermore, the only constraint this argument places on the trial state is that it should have a non-trivial overlap with the ground state. Beyond that, we are free to choose $|\Psi_T\rangle$ as needed. Since we will work exclusively in the position basis in our work, we will always pick $\Psi_T(\boldsymbol{\phi}) = \frac{1}{\sqrt{2\pi}}$ which is simple to implement from a path integral perspective. To compare this with the canonical ensemble approach, it is useful to re-express the PIGS operator expectation value using a trace,

$$\langle O \rangle = \mathrm{Tr}\Big(O|\Psi(\beta)\rangle\langle\Psi(\beta)|\Big), \quad Z_0 = \mathrm{Tr}\Big(|\Psi(\beta)\rangle\langle\Psi(\beta)|\Big), \quad |\Psi(\beta)\rangle = \frac{1}{\sqrt{Z_0}} e^{-\frac{\beta}{2}H}|\Psi_T\rangle \tag{1.92}$$

where we have used the cyclic property of the trace to re-write Eq. (1.86) in this form. This shows that the defining difference between the canonical ensemble approach and PIGS is the density matrix used to approximate the ground state; in PIGS, the canonical ensemble is replaced by the density matrix associated with the projected state $|\Psi(\beta)\rangle$. We will use this form when we discuss entanglement entropy in chapter 4.

While the construction above shows that the PIGS expectation value converges to the desired result, we have not yet shown that it has any benefit over using the canonical ensemble approach discussed in subsection 1.2.1. Indeed, because the canonical ensemble density matrix is an exponential function, that will also converge exponentially to the ground state in the limit of $\beta \to \infty$. To justify using PIGS then, observe that PIGS allows us to pick a trial state while the canonical ensemble approach does not. Moreover, in the quotient: Eq. (1.90), the higher energy states contribute to the error in the PIGS estimate for a given β. Therefore, if the ground state has a certain symmetry which is broken by the excited states, we can pick the trial state to be in the same symmetry sector as the ground state. This will lead to faster convergence to the ground state by allowing us to use a smaller value of β to attain the same accuracy threshold in our calculations as we would with the canonical ensemble approach with a larger β, especially while simulating systems with small energy gaps.

With PIGS, we can also use an approximate ground state if one is available. By virtue of being close to the ground state, $|c_j|$ for $j > 0$ will be small which will allow the simulation to converge to the correct ground state faster. Our trial function is an example of this; note that for g close to 0, the chain of rotors will have a ground state close to the ground state of the kinetic energy operator. Since the kinetic energy operator is the second derivative, $\langle \boldsymbol{\phi}|K|\Psi_T\rangle = -\sum_{i=1}^{N} \partial_{\phi_i}^2 \Psi_T = 0$ which implies that our trial state minimizes the energy for $g = 0$. Consequently for g close to 0, the constant trial function constitutes an approximate ground state which yields faster convergence.

The path integral construction for PIGS follows similarly to the case discussed in subsection 1.2.1. To see this, observe that we can use the time-slicing argument for the projector $e^{-\frac{\beta}{2}H}$ as well,[16]

$$e^{-\frac{\beta}{2}H} = \left(e^{-\tau H}\right)^{P/2}, \quad \tau = \beta/P \tag{1.93}$$

$$\Rightarrow \rho(\boldsymbol{\phi}, \boldsymbol{\phi}', \beta/2) = \langle \boldsymbol{\phi}|e^{-\frac{\beta}{2}H}|\boldsymbol{\phi}'\rangle = \int d\vec{\boldsymbol{\phi}}_{P/2-1} \prod_{i=0}^{P/2-1} \langle \boldsymbol{\phi}_i|e^{-\tau H}|\boldsymbol{\phi}_{i+1}\rangle \tag{1.94}$$

In the last line, we have used the notation $\boldsymbol{\phi}_0 = \boldsymbol{\phi}$, $\boldsymbol{\phi}_{P/2} = \boldsymbol{\phi}'$ and $d\vec{\boldsymbol{\phi}}_{P/2-1} = d\boldsymbol{\phi}_1 ... d\boldsymbol{\phi}_{P/2-1}$ for convenience. Since $P/2$ has to be an integer, P must be even. Now, if we resolve Eq. (1.86) in the position basis, we get,

$$\begin{aligned}\langle O\rangle = \frac{1}{Z_0}\int \langle \Psi_T|\boldsymbol{\phi}_0\rangle \left(\prod_{i=0}^{P/2-1} \langle \boldsymbol{\phi}_i|e^{-\tau H}|\boldsymbol{\phi}_{i+1}\rangle\right) \langle \boldsymbol{\phi}_{P/2}|O|\boldsymbol{\phi}_{P/2+1}\rangle \\ \times \left(\prod_{i=P/2+1}^{P} \langle \boldsymbol{\phi}_i|e^{-\tau H}|\boldsymbol{\phi}_{i+1}\rangle\right) \langle \boldsymbol{\phi}_{P+1}|\Psi_T\rangle \; d\vec{\boldsymbol{\phi}}_{P+1}\end{aligned} \tag{1.95}$$

Here, $d\vec{\boldsymbol{\phi}}_{P+1} = d\boldsymbol{\phi}_0 ... d\boldsymbol{\phi}_{P+1}$. We will be interested in expectation values of operators that are diagonal in the position representation. Therefore, we can set $\langle \boldsymbol{\phi}_{P/2}|O|\boldsymbol{\phi}_{P/2+1}\rangle = \delta(\boldsymbol{\phi}_{P/2} - \boldsymbol{\phi}_{P/2+1}) O(\boldsymbol{\phi}_{P/2})$ and integrate over the resulting delta function to get,

$$\langle O\rangle = \frac{1}{2\pi Z_0}\int d\vec{\boldsymbol{\phi}}_P \left(\prod_{i=0}^{P-1} \rho(\boldsymbol{\phi}_i, \boldsymbol{\phi}_{i+1}, \tau)\right) O(\boldsymbol{\phi}_{P/2}) \tag{1.96}$$

Here, we have used our trial function definition $\Psi_T(\boldsymbol{\phi}) = \frac{1}{\sqrt{2\pi}}$ and denoted the measure $d\boldsymbol{\phi}_0 .... d\boldsymbol{\phi}_P$ by $d\vec{\boldsymbol{\phi}}_P$. Now, we can use a factorization to compute ρ since the error in this

approximation will be bounded by some power of $\tau = \beta/P$ which is small for a large P as before. In subsection 1.2.1, we used the symmetric Trotter factorization as an example and in the next chapter we will use the pair factorization. For now, let us assume a general factorization of the form $\rho(\boldsymbol{\phi}, \boldsymbol{\phi}', \tau) = \rho_K(\boldsymbol{\phi}, \boldsymbol{\phi}', \tau)\rho_{\tilde{V}}(\boldsymbol{\phi}, \boldsymbol{\phi}', \tau) + \mathcal{O}(\tau^l)$ for $l \geq 1$, since both the Trotter and the pair factorization take this form.[11] The factor of ρ_K here represents the N-particle free propagator and $\rho_{\tilde{V}}$ corresponds to the residual factor that accounts for the existence of the potential. The expectation value of an operator O that is diagonal in the position basis then becomes,

$$\langle O \rangle \approx \frac{1}{2\pi Z_0} \int d\vec{\boldsymbol{\phi}}_P \left(\prod_{i=0}^{P-1} \rho_K(\boldsymbol{\phi}_i, \boldsymbol{\phi}_{i+1}, \tau)\rho_{\tilde{V}}(\boldsymbol{\phi}_i, \boldsymbol{\phi}_{i+1}, \tau) \right) O(\boldsymbol{\phi}_{P/2}) \tag{1.97}$$

We could also expand the pseudo-partition function in this manner but since we will use Markov Chain Monte Carlo (MCMC) algorithms which rely on relative probabilities, the normalization will not be consequential.[16,72] For our ground state energy calculations using PIGS, note that the above estimator can not be used since the Hamiltonian is not diagonal in the position representation. However, to evaluate $\langle H \rangle$, we can use the fact that the projector $e^{-\frac{\beta}{2}H}$ and H commute to derive a new estimator as follows,[20]

$$\langle H \rangle = \frac{1}{Z_0} \langle \Psi_T | e^{-\frac{\beta}{2}H} H e^{-\frac{\beta}{2}H} | \Psi_T \rangle = \frac{1}{Z_0} \langle \Psi_T | e^{-\beta H} H | \Psi_T \rangle \tag{1.98}$$

Now, we follow our usual time-slicing scheme to get the PIGS estimator,

$$\langle H \rangle = \frac{1}{Z_0} \int d\vec{\boldsymbol{\phi}}_P \ \langle \Psi_T | \boldsymbol{\phi}_0 \rangle \left(\prod_{i=0}^{P-1} \langle \boldsymbol{\phi}_i | e^{-\tau H} | \boldsymbol{\phi}_{i+1} \rangle \right) \langle \boldsymbol{\phi}_P | H | \Psi_T \rangle \tag{1.99}$$

As before, $d\vec{\boldsymbol{\phi}}_P = d\boldsymbol{\phi}_0 ... d\boldsymbol{\phi}_P$ and $\tau = \beta/P$. Since our trial function is constant, the action of the Hamiltonian can be simplified,

$$\langle \boldsymbol{\phi} | H | \Psi_T \rangle = \langle \boldsymbol{\phi} | K | \Psi_T \rangle + \langle \boldsymbol{\phi} | V | \Psi_T \rangle \tag{1.100}$$

$$\langle \boldsymbol{\phi} | K | \Psi_T \rangle = -\sum_{i=1}^{N} \frac{\partial^2 \Psi_T}{\partial \phi_i^2}\bigg|_{\boldsymbol{\phi}} = 0, \quad \langle \boldsymbol{\phi} | V | \Psi_T \rangle = V(\boldsymbol{\phi})\Psi_T(\boldsymbol{\phi}) = \frac{1}{\sqrt{2\pi}} V(\boldsymbol{\phi}) \tag{1.101}$$

$$\Rightarrow \langle \boldsymbol{\phi} | H | \Psi_T \rangle = \frac{1}{\sqrt{2\pi}} V(\boldsymbol{\phi}) \tag{1.102}$$

This yields for the ground state energy estimator,[16,20]

$$\langle H\rangle = \frac{1}{2\pi Z_0}\int d\vec{\boldsymbol{\phi}}_P \left(\prod_{i=0}^{P-1}\rho_K(\boldsymbol{\phi}_i,\boldsymbol{\phi}_{i+1},\tau)\rho_{\tilde{V}}(\boldsymbol{\phi}_i,\boldsymbol{\phi}_{i+1},\tau)\right)V(\boldsymbol{\phi}_P) \tag{1.103}$$

It is instructive to note here that for the PIGS estimators, the paths are open i.e. $\boldsymbol{\phi}_0$ does not necessarily equal $\boldsymbol{\phi}_P$ because there is no trace operation. Therefore, the paths can start and end at different locations.[16] If we constructed the path integral for the expectation value of an arbitrary operator O using the canonical ensemble (see Eq. (1.53)), that would involve closed paths.[11] Calculations involving open paths require one extra variable that needs to be integrated over. However, since we need a large P for convergence in τ and because PIMC techniques scale polynomially in the number of integration variables, this does not appreciably affect the efficiency of our simulations. Another key difference between open and closed paths calculations is that for closed paths, all the beads are equivalent. Therefore, the operator can be evaluated on any one of them (or all of them with appropriate scaling) without affecting the results.[11] As we showed, for open paths, if O is a function of position, it needs to be evaluated at the middle bead. For our energy estimator, the potential needs to be evaluated at either the first or the last bead.[20]

1.2.3 Quantum Phase Transitions

For the $\mathbb{Z}_2$ chain, the quantum phase transition of interest is the one associated with the (1+1)d Ising universality class.[19] This is a continuous phase transition resulting from the spontaneous breaking of the $\mathbb{Z}_2$ symmetry of the chain at zero temperature for large g.[3] In this section, we provide a non-rigorous limit analysis to motivate the existence of a continuous phase transition as g is varied. To this end, we will analyze the limit as $g \to 0$ and the limit as $g \to \infty$. For $g = 0$, there are no interactions and the Hamiltonian is,

$$H = \sum_{i=1}^{N} l_i^2 = \sum_{i=1}^{N}\sum_{m_i=\infty}^{\infty} m_i^2 |m_i\rangle\langle m_i| \tag{1.104}$$

Here, we have resolved the Hamiltonian in the momentum representation. The ground state is then simply given by the product state that minimizes the energy,

$$|E_0\rangle = \bigotimes_{i=1}^{N} |m_i = 0\rangle \tag{1.105}$$

We can determine the wave-function associated with this state: $\langle \boldsymbol{\phi} | \vec{m} = 0^N \rangle = \psi_0(\boldsymbol{\phi}) = 1$. This is symmetric under the transformation: $\boldsymbol{\phi} \rightarrow \boldsymbol{\phi} + (\pi, ..., \pi)$. Therefore, in the limit of $g \rightarrow 0$, the ground state preserves the $\mathbb{Z}_2$ symmetry of the Hamiltonian. If we compute the ground state polarization $M = \frac{1}{N} \sum_{i=1}^{N} \cos(\phi_i)$, we get,

$$\langle M \rangle = \frac{1}{2N} \sum_{i=1}^{N} \langle m_i = 0 | e^{i\phi} + e^{-i\phi} | m_i = 0 \rangle = \frac{1}{2N} \sum_{i=1}^{N} \left(\langle 0 | 1 \rangle + \langle 0 | - 1 \rangle \right) = 0 \tag{1.106}$$

Because of this zero net polarization, the ground state in the limit of $g \rightarrow 0$ is often referred to as the disordered or the paraelectric state.[19,73] To analyze the opposite limit ($g \rightarrow \infty$), we first divide the Hamiltonian H by g to get,

$$H' = \frac{1}{g} \sum_{i=1}^{N} l_i^2 + \sum_{i=1}^{N-1} V_{i,i+1} \tag{1.107}$$

$$\Rightarrow \lim_{g \rightarrow \infty} H' = \sum_{i=1}^{N-1} V_{i,i+1} = \sum_{i=1}^{N-1} (\sin(\phi_i) \sin(\phi_{i+1}) - 2 \cos(\phi_i) \cos(\phi_{i+1})) \tag{1.108}$$

The ground state can again be determined by inspection. The potential energy is minimized by any linear combination of the states: $|\boldsymbol{\phi} = (0, ..., 0)\rangle$ and $|\boldsymbol{\phi} = (\pi, ..., \pi)\rangle$. Therefore, the ground state is two-fold degenerate and the $\mathbb{Z}_2$ symmetry preserving state is given by,

$$|\psi\rangle = \frac{1}{\sqrt{2}} \left(|\boldsymbol{\phi} = (0, ..., 0)\rangle + |\boldsymbol{\phi} = (\pi, ..., \pi)\rangle \right) \tag{1.109}$$

While the exact ground state is as specified by Eq. (1.109), in a physical system, this symmetry is spontaneously broken in the thermodynamic limit ($N \rightarrow \infty$) due to external perturbations which yields a non-zero net polarization.[19,73] To see this, let us apply a small external field as a mathematical device ($|h| << 1$),

$$H' = \sum_{i=1}^{N-1} (\sin(\phi_i) \sin(\phi_{i+1}) - 2 \cos(\phi_i) \cos(\phi_{i+1})) - h \sum_{i=1}^{N} \cos(\phi_i) \tag{1.110}$$

For $h > 0$, now the ground state is $|E_0\rangle = |\boldsymbol{\phi} = (0, ..., 0)\rangle$ and for $h < 0$, the ground state is $|E_0\rangle = |\boldsymbol{\phi} = (\pi, ..., \pi)\rangle$. Computing the expectation value of the polarization in these cases, we get,

$$\langle M \rangle_{h>0} = \frac{1}{N} \sum_{i=1}^{N} \cos(0) = 1, \quad \langle M \rangle_{h<0} = \frac{1}{N} \sum_{i=1}^{N} \cos(\pi) = -1 \tag{1.111}$$

The symmetry broken ground states that result as a consequence of the external perturbation have less symmetry than the Hamiltonian. This yields a non-zero polarization for large g. On the contrary, for the symmetry preserving state in Eq. (1.109), the polarization is identically zero. In theoretical models, this spontaneous symmetry breaking presents as an order of limits phenomenon.[3,4] One way to see this is by analyzing the relative probability of the system being in a state with a negative polarization ($\langle M \rangle = -1$) compared to a state corresponding to a positive polarization ($\langle M \rangle = 1$), in the presence of an external perturbation. To this end, let us first introduce a finite temperature so that we can use the canonical ensemble to compute the required probabilities (similar to our construction of the imaginary-time path integral in subsection 1.2.1). To compute the relative probability, first we re-express the perturbed Hamiltonian as follows,

$$H' = H'_0 + H'_1, \quad H'_0 = \sum_{i=1}^{N-1} (\sin(\phi_i)\sin(\phi_{i+1}) - 2\cos(\phi_i)\cos(\phi_{i+1})), \tag{1.112}$$

$$H'_1 = -h\sum_{i=1}^{N} \cos(\phi_i) = -hMN \tag{1.113}$$

Here, both H'_0 and H'_1 are diagonal in the position representation which implies that the canonical ensemble probabilities can be computed as,

$$P(M=-1) = \frac{1}{Z} e^{-\beta H'_0} e^{-\beta H'_1} = \frac{1}{Z} e^{-\beta H'_0} e^{-\beta hN} \tag{1.114}$$

$$P(M=1) = \frac{1}{Z} e^{-\beta H'_0} e^{-\beta H'_1} = \frac{1}{Z} e^{-\beta H'_0} e^{\beta hN} \tag{1.115}$$

We have suppressed the expectation value operator $\langle \cdot \rangle$ for M in the above equations. Note that $\langle M \rangle = 1$ implies $\boldsymbol{\phi} = (0, ..., 0)$ and $\langle M \rangle = -1$ implies $\boldsymbol{\phi} = (\pi, ..., \pi)$. Since $H'_0(0, ..., 0) = H'_0(\pi, ..., \pi)$, the relative probability only depends on the perturbation term and is given by,

$$P = \frac{P(M=-1)}{P(M=1)} = \frac{e^{-\beta hN}}{e^{\beta hN}} = e^{-2\beta hN} \tag{1.116}$$

In this analysis, we need to consider three limits: $\beta \to \infty$, $N \to \infty$ and $h \to 0$ to recover our system of interest. We will always take the limit of $\beta \to \infty$ last. If we take the limit of $h \to 0$ first and then take the limit of $N \to \infty$, we get that the relative probability $P = 1$ which implies an equal probability of measuring the polarization to be positive or negative and an average polarization of zero. However, if we first take the limit of $N \to \infty$

and then take the limit $h \to 0$, we get that the relative probability $P = 0$. This implies a net positive polarization and realizes the physical case of a symmetry broken ground state. Due to the non-zero polarization, this system is referred to as the ordered or the ferroelectric state.[19,73]

The above calculation also shows that the spontaneous symmetry breaking phenomenon is only truly manifest in the thermodynamic limit ($N \to \infty$). For this limit, the symmetry preserving ground state is an unstable fixed point. Consequently, for a system in the thermodynamic limit, as the value of g is increased, the ground state goes from a disordered (symmetry preserving) state to an ordered (symmetry breaking) state. It is the crossover between these two regimes that yields the (1+1)d Ising universality class phase transition for this system.

It is instructive to note that the above non-rigorous analysis provided to motivate the existence of a continuous phase transition can be formalized using DMRG calculations.[19,73] Such computational studies rely on finite size effects which can be scaled to interrogate the exact nature of continuous phase transitions.[3,4] The above analysis, at least in the case of simpler models such as the TFIM, can also be formalized using theoretical tools based on renormalization group techniques.[2–4] In the next section, we discuss Monte Carlo (MC) sampling techniques which will allow us to use our path integral formalism to computationally probe some of the consequences of this transition in chapter 2.

1.3 Quantum Monte Carlo For Planar Rotations

Evaluating the PIGS estimators discussed above would require us to compute multi-dimensional integrals which becomes prohibitively expensive using typical integrators. One possible way to simulate the system is to use the Feynman-Kac formulation from Eq. (1.84) since the estimators discussed above can also be expressed in that statistical language.[11] This would involve picking a sufficiently fine mesh defined by $\tau = \beta/P$ for the interval $[0, \beta]$ and generating a large set of paths for each particle by sampling Eq. (1.85). To do this, we would first uniformly sample a starting position ϕ_0 (for a path associated with a single particle) and then sample $\rho_K(\phi_i, \phi_{i+1}, \tau)$ as the transition probability function to statistically determine the next point of the path: ϕ_1. Since for small τ, ρ_K is a Gaussian in the distance between two points on the circle, this can be done directly by sampling the normal distribution. Continuing this process iteratively for P steps will then yield a single

path for a single particle. Once we have a sufficiently large set of paths for each particle to bound the statistical error on our estimators within an acceptable margin of uncertainty, we can evaluate the required function for each path and average over the resulting values. The function in this case would be the estimator times the residual density $\rho_{\tilde{V}}$ arising from the existence of a non-trivial potential. To get the operator expectation value, we would also need to compute the pseudo-partition function by averaging the functional $\rho_{\tilde{V}}$ over all the paths.

While easy to parallelize, this approach turns out to be sub-optimal in practice because paths generated in this manner do not reflect the full distribution: ρ.[11] In particular, there could exist paths (or large sections of certain paths) for which $\rho_{\tilde{V}} \approx 0$. Sampling those leads to inefficiencies because such regions of the configuration space do not appreciably contribute to expectation values. Conversely, regions with larger residual density weights would be under-sampled if the number of paths generated is not sufficiently large. To circumvent these issues we must treat $\rho \approx \rho_K \rho_V$ as our probability density directly which requires sampling the distribution,

$$P(\boldsymbol{\phi}_0, ..., \boldsymbol{\phi}_P) = \frac{1}{2\pi Z_0} \prod_{i=0}^{P-1} \rho_K(\boldsymbol{\phi}_i, \boldsymbol{\phi}_{i+1}, \tau) \rho_{\tilde{V}}(\boldsymbol{\phi}_i, \boldsymbol{\phi}_{i+1}, \tau) \tag{1.117}$$

Note here that the pseudo-partition function needs to be included to normalize the probabilities. Due to the large number of variables and the complexity of the function, we can not sample it directly (like we would, for instance, a normal or a uniform distribution).[74] One way to circumvent this issue is to construct a Markov chain and sample that instead.[11,16] If the desired distribution (Eq. (1.117) in our case) is a stationary distribution of the constructed Markov chain and the chain is ergodic, then after some initial burn-in period, the drawn samples will be distributed according to the distribution of interest.[72] However, the samples drawn from the Markov chain are not independent; they are auto-correlated by construction.[72] Therefore, to only use independent draws in our calculations, we need to neglect a certain set of consecutive samples before averaging. In this section, we introduce two MCMC algorithms: the typically employed Metropolis-Hastings (MH) technique, and Gibbs sampling. In the next chapter, we will use the Gibbs sampling algorithm for our calculations.[72,74,75]

1.3.1 Metropolis-Hastings

MH is a rejection-based MCMC algorithm that is useful for sampling continuous distributions. It proceeds as follows:[74]

1. We start with an arbitrary value for each of the variables: $\vec{\boldsymbol{\phi}}(t=0) = (\boldsymbol{\phi}_0(t=0), ..., \boldsymbol{\phi}_P(t=0))$. Here t denotes the simulation step. For our simulation, there are $L = N(P+1)$ angular variables that specify the configuration space since we have $P+1$ beads and N rotors.

2. Then, for each simulation step $t > 0$, we iterate over each of the L angular variables. Each iteration involves suggesting a new value according to some easy-to-sample distribution (such as the normal or uniform distributions). If the configuration vector at simulation step t was $\vec{\boldsymbol{\phi}}$ and we are suggesting a new value for the kth variable (let us call it $\tilde{\phi}^k$), then the suggested configuration vector is:

$$\vec{\boldsymbol{\theta}} = (\phi_t^1, ..., \phi_t^{k-1}, \tilde{\phi}^k, \phi_t^{k+1}, ..., \phi_t^L) \tag{1.118}$$

   where we have used the following vectorized notation to represent the configuration at simulation time t while iterating over the kth variable (before the kth variable has been updated),

$$\vec{\boldsymbol{\phi}} = (\phi_{t+1}^1, ..., \phi_{t+1}^{k-1}, \phi_t^k, \phi_t^{k+1}, ..., \phi_t^L) \tag{1.119}$$

3. Following the suggestion, we compute the acceptance ratio:[74]

$$\alpha = \frac{P(\phi_{t+1}^1, ..., \phi_{t+1}^{k-1}, \tilde{\phi}^k, \phi_t^{k+1}, ..., \phi_t^L)}{P(\phi_{t+1}^1, ..., \phi_{t+1}^{k-1}, \phi_t^k, \phi_t^{k+1}, ..., \phi_t^L)} \tag{1.120}$$

   Note that due to the quotient, any normalization factor in $P(\boldsymbol{\phi}_0, ..., \boldsymbol{\phi}_P)$, as well as any function that does not depend on $\tilde{\phi}^k$ cancels.

4. Finally, we generate a uniform random number u between 0 and 1. If $u \leq \alpha$, we accept the new value: $\left(\phi_{t+1}^k \to \tilde{\phi}^k\right)$. Otherwise, we reject the suggested value and the kth value remains unchanged $\left(\phi_{t+1}^k \to \phi_t^k\right)$.[74]

Because each move relies on the state at the previous timestep, samples generated in this way are correlated as discussed above.[16,74] Therefore, to average over independent

configurations, we need to sparsely select samples from the full set, neglecting as many samples between draws as the Markov chain autocorrelation time. Typically, a certain set of samples from the beginning is also neglected to ensure that the Markov chain has converged to the desired distribution.[74] This is called the burn-in period. Both of these hyper-parameters need to be optimized until the desired properties have converged, in practice. It is also important to note that regardless of whether a move is accepted or not, it is still counted i.e. we also include samples associated with rejected moves when we compute expectation values.[16,74] Therefore, if the acceptance ratio is small (a large number of moves are rejected), this algorithm can become inefficient. The Gibbs sampling algorithm discussed in the next section is notably rejection-free and does not suffer from this potential inefficiency.

1.3.2 Gibbs Sampling

The Gibbs sampling algorithm requires the existence of a discrete state space which can be obtained by imposing a grid on the angular positions of the rotor chain problem. The algorithm proceeds as follows:[74,75]

1. We start with an arbitrary value for each of the variables. For the planar rotor lattice problem, this is the set of $L = N(P+1)$ angular variables that specify the configuration space.

2. For each variable, we construct the conditional probability distribution. While moving from simulation step t to simulation step $t+1$, the jth variable conditional probability is given by:[75]

$$\Pr\left(\phi_{t+1}^{j}|\phi_{t+1}^{1},...,\phi_{t+1}^{j-1},\phi_{t}^{j+1},...,\phi_{t}^{L}\right)=\frac{P\left(\phi_{t+1}^{1},...,\phi_{t+1}^{j-1},\phi_{t+1}^{j},\phi_{t}^{j+1},...,\phi_{t}^{L}\right)}{\sum_{\phi^{j}}P\left(\phi_{t+1}^{1},...,\phi_{t+1}^{j-1},\phi^{j},\phi_{t}^{j+1},...,\phi_{t}^{L}\right)} \quad (1.121)$$

   Again, note that since the probability density enters the algorithm as a quotient, normalization factors as well as any functions that do not depend on ϕ^j cancel. Moreover, there is a finite sum in the denominator due to the presence of a grid in ϕ.

3. Finally we generate a sample $\tilde{\phi}_{t+1}^{j}$ amongst the possible values of ϕ_{t+1}^{j} by uniformly sampling the list of grid points weighted by their relative conditional probabilities, and set $\phi_{t+1}^{j}=\tilde{\phi}_{t+1}^{j}$.

Comparing this to the MH algorithm, it is clear that there is no rejection step. This not only removes the need for optimizing the acceptance ratio of the simulation, but also leads to faster convergence due to the absence of redundant simulation time-steps. Finally, another benefit to using Gibbs sampling is that it typically leads to lower auto-correlation times between samples which further lowers the number of simulation time-steps.[20]

1.4 Thesis Outline

The remainder of this thesis is organized as follows: in chapter 2, we develop the pair factorization technique for planar rotations. We then use this method in conjunction with the DVR grid and Gibbs sampling to study the ground state properties of the $\mathbb{Z}_2$ chain of planar rotors. We also introduce the Wigner-Kirkwood expansion in chapter 2 to analyze the error in the pair approximation, and show that it is $O(\tau^3)$.

In Chapter 3, we discuss qubit encodings for dipolar planar rotor lattices. We introduce two mappings; the unary encoding and the binary encoding. Both encodings map a d-dimensional lattice of rotors to a $(d+1)$-dimensional lattice of qubits. Using sparse diagonalization, we compute the ground state energy in both qubit representations and briefly discuss resource requirements for quantum phase estimation (QPE) simulations targeting small rotor chains.

Chapter 4 is dedicated to conclusions and future research directions. These include entanglement entropy calculations using the pair-DVR approach introduced in chapter 2 and a potential approach for developing a SSE technique for simulating planar rotations based on the clock-shift representation of the Hamiltonian. We also discuss extensions of our path integral approach to higher dimensional lattices, and future research pertaining to the qubit encodings introduced in chapter 3.

Chapter 2

Pair Approximating The Action For Molecular Rotations In Path Integral Monte Carlo

This chapter has been reproduced from Muhammad Shaeer Moeed, Tobias Serwatka and Pierre-Nicholas Roy, "Pair approximating the action for molecular rotations in path integral Monte Carlo", Journal of Chemical Physics 162 (2), 024113 (2025), with the permission of AIP Publishing.[76]

2.1 Introduction

Path integral Monte Carlo (PIMC) simulations are ubiquitous in the study of finite-temperature as well as ground state properties of many-body quantum systems.[11,16,59,60,77] Typically, the high-temperature propagator is approximated using the symmetric Trotter factorization which, while theoretically guaranteed to converge, can lead to long simulations times in the presence of large numbers of degrees of freedom.[11,57] Moreover, path integral simulations aimed at numerically studying critical phenomena typically experience critical slowing down which causes the equilibration and auto-correlation times to become unfeasibly large.[21,22]

The pair approximation is an alternative factorization scheme to Trotter factorization.[59,60]

It was initially studied in the context of superfluidity because it accounts for all 2-body correlations exactly which improves PIMC convergence in imaginary time. It was shown numerically by Ceperley that paths sampled using the pair propagator are approximately 20 times more accurate than the primitive factorization.[11] The pair approximation was also later used to compute real time correlation functions for quantum fluids.[78] Finally, this factorization technique has been shown to be very useful for simulating systems with two-body zero range interactions.[79–81] However, these applications focused on factoring the many-body propagator in Cartesian coordinates.

Another problem that can be studied using PIMC is that of dipolar lattices. Such systems have recently garnered interest as potential platforms for quantum devices[82,83] and are conventionally constructed using optical traps[84,85] or via chemical confinement of molecules with a permanent dipole moment such as water.[86,87] Such dipolar lattices are also good models for examining the ferroelectric properties of naturally occurring crystals such as Beryl and Cordierite because they have cavities capable of confining water molecules.[23] Recent work has suggested that these confined water molecules behave like planar rotors interacting via their electric dipole moments.[24]

In these confined molecular systems, at low temperatures, the vibrational degrees of freedom of each molecule are restricted to their respective ground states. The orientational statistical mechanics of the many-body lattice is mostly determined by the rotational degrees of freedom of pinned molecules. Such effective Hamiltonians underscore the need to extend our PIMC capabilities to angular coordinates because those yield a natural parametrization of interacting rotational degrees of freedom. Recent Density Matrix Renormalization Group (DMRG) studies pertaining to 1d lattices (chains) of planar rotors interacting with a nearest neighbor dipole-dipole coupling have shown that the system admits a quantum phase transition[3] when the interaction strength between the rotors is approximately 0.5.[19]

PIMC techniques have been used to study rotations before, including the development of a 4th-order propagation scheme for linear rotors.[18,51,88–91] Here, we develop a pair product approximation for angular coordinates to study rotational motion because a pair propagation scheme will inherently account for all 2-body correlations exactly, at the expense of a modest computational overhead. Moreover, the techniques developed here for a chain of planar rotors can readily be extended to higher dimensional lattices to study the ground state properties of crystals such as Beryl and Cordierite. The paper is organized as follows. We present the theoretical formalism pertaining to the pair approximation in Sec. 2.2 and

report our computational results in Sec. 2.3. We conclude and discuss future research directions in Sec. 2.4.

2.2 Theory

2.2.1 Planar Rotor Chain

The Hamiltonian for a linear chain of N planar rotors with nearest neighbor dipole-dipole interactions is given by ($\hbar = 1$),[19]

$$H = \sum_{i=1}^{N} K_i + g \sum_{i=1}^{N-1} V_{i,i+1} \tag{2.1}$$

We use open boundary conditions for this work i.e. the first rotor doesn't interact with the last rotor in the chain. While the techniques discussed in this work can be used to simulate periodic boundaries as well, this is done so that we can compare our results to DMRG which is better suited to open boundary conditions. A depiction of this model system is given in Fig. (2.1). In angular position coordinates, the kinetic and potential energy operators take the form,

$$K_i = l_i^2 = -\frac{\partial^2}{\partial \phi_i^2} \tag{2.2}$$

$$V_{i,i+1} = (\sin(\phi_i)\sin(\phi_{i+1}) - 2\cos(\phi_i)\cos(\phi_{i+1})) \tag{2.3}$$

Here, ϕ_i represents the angular position of the ith rotor in the chain and g is the coupling strength which is proportional to the cubic inverse distance between successive rotors (r^{-3}).

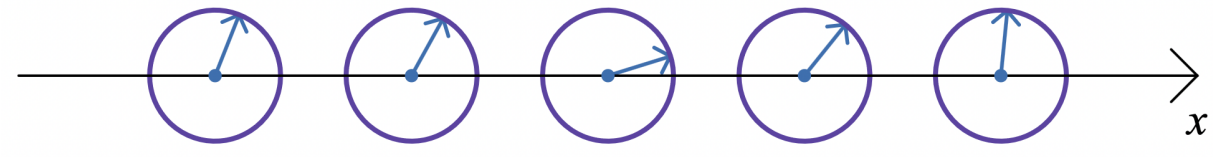


Figure 2.1: Schematic representation of a chain of planar rotors.

While dipolar interactions are longer range, we restrict ourselves to a nearest-neighbor coupling following previous DMRG studies[19] which have shown that this system undergoes a quantum phase transition at $g \approx 0.5$. Therefore, the above Hamiltonian is a good candidate for optimizing rotational PIGS simulations since it admits a non-trivial phase diagram and allows us to compare our results against existing DMRG literature.

2.2.2 The Pair Approximation

The pair propagator can be derived using the Feynman-Kac theorem. Our construction follows the discussion provided in Ceperley's review[11] closely. To this end, consider the low-temperature density operator $e^{-\beta H}$ expressed as a convolution of high temperature density operators,

$$\begin{aligned} \rho(\boldsymbol{\phi}, \boldsymbol{\phi}', \beta) &= \langle \boldsymbol{\phi} | e^{-\beta H} | \boldsymbol{\phi}' \rangle \\ &= \int d\boldsymbol{\phi}_1 ... d\boldsymbol{\phi}_{P-1} \langle \boldsymbol{\phi} | e^{-\tau H} | \boldsymbol{\phi}_1 \rangle ... \langle \boldsymbol{\phi}_{P-1} | e^{-\tau H} | \boldsymbol{\phi}' \rangle \end{aligned} \tag{2.4}$$

where $\tau = \beta/P = 1/(PT)$ is the imaginary time and T is the temperature. Note that in Eq. (2.4), we have inserted P beads and $\boldsymbol{\phi}_j = \left(\phi_j^1, ..., \phi_j^N\right)$ is the vector valued coordinate associated with the jth bead. For the remainder of this section, we will reserve superscripts for particle indices and subscripts for bead indices whenever we refer to the configuration variables (denoted $\boldsymbol{\phi}$). We can express the high temperature density matrix as a continuum path integral,

$$\rho(\boldsymbol{\phi}, \boldsymbol{\phi}', \tau) = \int D\boldsymbol{\phi}_\tau \; e^{-\int_0^\tau d\tau' V(\boldsymbol{\phi}(\tau'))} \tag{2.5}$$

where the measure of the integral corresponds to N independent Brownian motions on a circle. The path integral above is equivalent to the Feynman-Kac theorem,

$$\rho(\boldsymbol{\phi}, \boldsymbol{\phi}', \tau) = \rho_0(\boldsymbol{\phi}, \boldsymbol{\phi}', \tau) \left\langle e^{-\int_0^\tau d\tau' V(\boldsymbol{\phi}(\tau'))} \right\rangle_{\mu(\boldsymbol{\phi}, \boldsymbol{\phi}')} \tag{2.6}$$

where the angled brackets denote averaging over N independent Brownian motions on a circle starting at $\boldsymbol{\phi}$ and ending at $\boldsymbol{\phi}'$. The transition probability density for this stochastic

process (denoted $\mu(\boldsymbol{\phi}, \boldsymbol{\phi}')$) is simply the free propagator for a chain of N planar rotors,[92]

$$\mu(\boldsymbol{\phi}, \boldsymbol{\phi}') = \langle \boldsymbol{\phi} | e^{-\tau K} | \boldsymbol{\phi}' \rangle = \prod_{j=1}^{N} \langle \phi^j | e^{-\tau K_j} | \phi'^j \rangle \tag{2.7}$$

$$\langle \phi^j | e^{-\tau K_j} | \phi'^j \rangle = \frac{1}{2\pi} \sum_{m=-\infty}^{\infty} e^{-\tau m^2 + im(\phi^j - \phi'^j)} \tag{2.8}$$

Eq. (2.8) is a Jacobi-Theta function.[93] In Eq. (2.6), note that we have simply restated the path integral in terms of statistics; the free propagator term represents the probability of taking any path between $\boldsymbol{\phi}$ and $\boldsymbol{\phi}'$ and the second term is the conditional expectation of the functional $\exp\left(-\int V(\tau')\, d\tau'\right)$ over all such paths. Since our potential is pairwise additive,

$$e^{\left(-\int_0^\tau d\tau'\ V(\boldsymbol{\phi}(\tau'))\right)} = e^{\left(-\sum_{j=1}^{N-1} \int_0^\tau d\tau'\ V_{j,j+1}(\boldsymbol{\phi}(\tau'))\right)} = \prod_{j=1}^{N-1} e^{\left(-\int_0^\tau d\tau'\ V_{j,j+1}(\boldsymbol{\phi}(\tau'))\right)} \tag{2.9}$$

The pair approximation relies on ignoring all correlations that are higher than 2-body in the averaging operation[11] of Eq. (2.6),

$$\left\langle \prod_{j=1}^{N-1} e^{\left(-\int_0^\tau d\tau'\ V_{j,j+1}(\boldsymbol{\phi}(\tau'))\right)} \right\rangle_{\mu(\boldsymbol{\phi},\boldsymbol{\phi}')} \approx \prod_{j=1}^{N-1} \left\langle e^{\left(-\int_0^\tau d\tau'\ V_{j,j+1}(\boldsymbol{\phi}(\tau'))\right)} \right\rangle_{\mu_j(\boldsymbol{\phi},\boldsymbol{\phi}')} \tag{2.10}$$

Here, the final averaging operation is taken to be over 2 body random walks on a circle denoted μ_j where,

$$\mu_j(\boldsymbol{\phi}, \boldsymbol{\phi}') = \langle \phi^j | e^{-\tau K_j} | \phi'^j \rangle \langle \phi^{j+1} | e^{-\tau K_{j+1}} | \phi'^{j+1} \rangle \tag{2.11}$$

Now we can again use the Feynman-Kac theorem from Eq. (2.6) to express the average over random walks as a product of two-body densities,

$$\prod_{j=1}^{N-1} \left\langle e^{\left(-\int_0^\tau d\tau'\ V_{j,j+1}(\boldsymbol{\phi}(\tau'))\right)} \right\rangle_{\mu_j(\boldsymbol{\phi},\boldsymbol{\phi}')} = \prod_{j=1}^{N-1} \frac{\rho_j^{(2)}(\boldsymbol{\phi}, \boldsymbol{\phi}', \tau)}{\rho_{0,j}^{(2)}(\boldsymbol{\phi}, \boldsymbol{\phi}', \tau)} \tag{2.12}$$

Here, $\rho_j^{(2)}$ is the two-body density operator,

$$\rho_j^{(2)}(\boldsymbol{\phi}, \boldsymbol{\phi}', \tau) = \langle \phi^j, \phi^{j+1} | e^{-\tau H_j^{(2)}} | \phi'^j, \phi'^{j+1} \rangle \tag{2.13}$$

$$H_j^{(2)} = K_j + K_{j+1} + V_{j,j+1} \tag{2.14}$$

Similarly, $\rho_{0,j}^{(2)}$ is the free two-body density operator,

$$\rho_{0,j}^{(2)}(\boldsymbol{\phi}, \boldsymbol{\phi}', \tau) = \langle \phi^j, \phi^{j+1} | e^{-\tau K_j^{(2)}} | \phi'^j, \phi'^{j+1} \rangle \tag{2.15}$$

$$K_j^{(2)} = K_j + K_{j+1} \tag{2.16}$$

This finally yields the pair approximated form of the high-temperature density operator matrix elements,

$$\rho(\boldsymbol{\phi}, \boldsymbol{\phi}', \tau) \approx \rho_0(\boldsymbol{\phi}, \boldsymbol{\phi}', \tau) \prod_{j=1}^{N-1} \frac{\rho_j^{(2)}(\boldsymbol{\phi}, \boldsymbol{\phi}', \tau)}{\rho_{0,j}^{(2)}(\boldsymbol{\phi}, \boldsymbol{\phi}', \tau)} \tag{2.17}$$

The pair approximation is mainly motivated by the form of the pairwise nature of the potential. The two-body correlations are entirely accounted for by construction. However, many-body correlations which are often less relevant are ignored. It would be interesting to explore the utility of the pair approximation in the presence of many-body interactions.

2.2.3 Pair Density Error

Usual approaches for path integral simulations employ the symmetric Trotter approximation,

$$\langle \boldsymbol{\phi} | e^{-\tau H} | \boldsymbol{\phi}' \rangle \approx e^{-\frac{\tau}{2}(V(\boldsymbol{\phi}) + V(\boldsymbol{\phi}'))} \langle \boldsymbol{\phi} | e^{-\tau K} | \boldsymbol{\phi}' \rangle \tag{2.18}$$

for which it is easy to show that the error is $\mathcal{O}(\tau^3)$ using the Baker–Campbell–Hausdorff (BCH) formula. To compare the pair density with the symmetric Trotter factorization, it is instructive to derive the density error in the pair approximation. However, since the pair density is defined in terms of matrix elements, it is convenient to use the asymptotic Wigner-Kirkwood series for this purpose.[58,68,69] To this end, note first that the density operator satisfies the Bloch equation,

$$\left(\frac{\partial}{\partial \tau} + H \right) \rho(\boldsymbol{\phi}, \boldsymbol{\phi}', \tau) = 0 \tag{2.19}$$

$$\lim_{\tau \to 0} \rho(\boldsymbol{\phi}, \boldsymbol{\phi}', \tau) = \delta(\boldsymbol{\phi} - \boldsymbol{\phi}') \tag{2.20}$$

Since we want a series expansion for the quotient of the full propagator and the free propagator, we assume that the solution takes the form,

$$\rho(\boldsymbol{\phi}, \boldsymbol{\phi}', \tau) = \rho_0(\boldsymbol{\phi}, \boldsymbol{\phi}', \tau) F(\boldsymbol{\phi}, \boldsymbol{\phi}', \tau) \tag{2.21}$$

Then, using the Bloch equation for the free propagator as well as the full propagator, we get the following differential equation for F (see Supplementary Material, Sec. A for details),

$$\left(\frac{\partial}{\partial\tau} - \Delta_{\boldsymbol{\phi}} - 2\frac{\nabla_{\boldsymbol{\phi}}\rho_0}{\rho_0}\cdot\nabla_{\boldsymbol{\phi}} + V\right)F = 0 \tag{2.22}$$

where we have used the notation,

$$\nabla_{\boldsymbol{\phi}} = \left(\frac{\partial}{\partial\phi_1}, ..., \frac{\partial}{\partial\phi_N}\right), \quad \Delta_{\boldsymbol{\phi}} = \sum_{i=1}^{N}\frac{\partial^2}{\partial\phi_i^2} \tag{2.23}$$

It can be shown using properties of Jacobi-Theta functions that to first order in τ (see Supplementary Material, Sec. B for details),

$$\left(\frac{\nabla_{\boldsymbol{\phi}}\rho_0}{\rho_0}\right) \approx -\frac{1}{2\tau}(\boldsymbol{\phi} - \boldsymbol{\phi}') \tag{2.24}$$

To understand this approximation in more detail, note that the free propagator can be written as follows using the Poisson summation formula,[65]

$$\rho_0^{(1)}(\phi^j, \phi'^j, \tau) = \frac{1}{\sqrt{4\pi\tau}}\sum_{k=0}^{\infty} e^{-(\phi^j - \phi'^j - 2\pi k)^2/4\tau} \tag{2.25}$$

This is a sum over Gaussians, each with variance 2τ and mean $2\pi k$ for $k \in \mathbb{Z}$. When $\tau << 2\pi$, each of these Gaussians are localized to their respective 2π intervals which yields Eq. (2.24) for $\left(\frac{\nabla_{\boldsymbol{\phi}}\rho_0}{\rho_0}\right)_j$ on the interval $[-\pi, \pi)$ again. Therefore, this approximation is valid whenever τ is small enough such that these Gaussians are sufficiently peaked in their 2π intervals that they do not appreciably affect the free propagator in other 2π intervals. Since in our path integral simulations, we expand the high temperature propagator using the pair factorization, we can use this to analyze the τ error in our approximation.

Using this, we get the same differential equation for F as in the case of Cartesian coordinates for linear motion,[69]

$$\left(\frac{\partial}{\partial\tau} - \Delta_{\boldsymbol{\phi}} + \frac{1}{\tau}(\boldsymbol{\phi} - \boldsymbol{\phi}')\cdot\nabla_{\boldsymbol{\phi}} + V\right)F = 0 \tag{2.26}$$

Now, we can expand F as a power series in τ,

$$F = \sum_{n=0}^{\infty}\frac{(-\tau)^n}{n!}P_n(\boldsymbol{\phi}, \boldsymbol{\phi}') \tag{2.27}$$

Note that we can set $P_0(\boldsymbol{\phi}, \boldsymbol{\phi}') = F(\boldsymbol{\phi}, \boldsymbol{\phi}', 0) = 1$ because as $\tau \to 0$, the system becomes classical and $F \to e^{-\tau V} \approx 1 - \tau V$. This differential equation can be solved using Perelomov's recursion relation,[69]

$$P_n(\boldsymbol{\phi}, \boldsymbol{\phi}') = n \int_0^1 dt\ t^{n-1} V(\boldsymbol{\theta}(t)) P_{n-1}(\boldsymbol{\theta}(t), \boldsymbol{\phi}') - n \int_0^1 dt\ t^{n-1} \Delta_{\boldsymbol{\theta}} P_{n-1}(\boldsymbol{\theta}(t), \boldsymbol{\phi}') \tag{2.28}$$

where $\boldsymbol{\theta}(t) = t\boldsymbol{\phi} + (1-t)\boldsymbol{\phi}'$. Since $P_0 = 1$, P_1 can be readily computed using Eq. (2.28),

$$P_1(\boldsymbol{\phi}, \boldsymbol{\phi}') = \int_0^1 V(\boldsymbol{\theta}(t))\ dt = \sum_{i=1}^{N-1} W_{i,i+1}(\boldsymbol{\phi}, \boldsymbol{\phi}') \tag{2.29}$$

$$W_{i,i+1}(\boldsymbol{\phi}, \boldsymbol{\phi}') = \int_0^1 V_{i,i+1}(\theta_i(t), \theta_{i+1}(t)) dt \tag{2.30}$$

where we have used the fact that for us, the potential is pairwise additive. For P_2, we can now use P_1 and integrate the first term by parts to get (see Supplementary Material, Sec. C for details),

$$\begin{aligned} P_2(\boldsymbol{\phi}, \boldsymbol{\phi}') = &\sum_{j=1}^{N-1} W_{j,j+1}^2 + 2 \sum_{i<j}^{N-1} W_{i,i+1} W_{j,j+1} \\ &-2 \sum_{i=1}^{N-1} \int_0^1 dt\ t \left(\frac{\partial^2 W_{i,i+1}}{\partial \theta_i^2} + \frac{\partial^2 W_{i,i+1}}{\partial \theta_{i+1}^2} \right) \end{aligned} \tag{2.31}$$

where $W_{j,j+1} = W_{j,j+1}(\boldsymbol{\theta}(t), \boldsymbol{\phi}')$. Now, we can return to our original goal of comparing the two sides of Eq. (2.17) in powers of τ. For the right side, we have products over pair densities. We can construct a power series for this product as well,

$$\prod_{n=1}^{N-1} \frac{\rho_j^{(2)}}{\rho_{0,j}^{(2)}} = \prod_{n=1}^{N-1} F_n^{(2)} = \sum_{l=0}^{\infty} \frac{(-\tau)^l}{l!} Q_l \tag{2.32}$$

To compute Q_l, we first expand each $F_n^{(2)}$ as a power series,

$$F_n^{(2)} = \sum_{k=0}^{\infty} \frac{(-\tau)^n}{n!} P_{k,n}^{(2)} \tag{2.33}$$

Here, the terms $P_{k,n}^{(2)}$ are determined using the Perelomov recursion relation as well since $F_n^{(2)}$ is the restriction of F to the case of 2 rotors. Taking the product over all pair terms

as required by Eq. (2.32) yields $Q_0 = 1$. For the first order term, we get,

$$Q_1 = \sum_{n=1}^{N-1} P_{1,n}^{(2)} \tag{2.34}$$

From Eq. (2.29), it can be seen that for the 2-body problem,

$$P_{1,n}^{(2)} = \int_0^1 V_{n,n+1}(\theta_n(t), \theta_{n+1}(t))\ dt = W_{n,n+1} \tag{2.35}$$

which implies that the series in Eqs. (2.27) and (2.32) agree to first order. For the second order term, note that Q_2 takes the form,

$$Q_2 = \sum_{n=1}^{N-1} P_{2,n}^{(2)} + 2 \sum_{n<m}^{N-1} P_{1,n}^{(2)} P_{1,m}^{(2)} \tag{2.36}$$

As before, we can determine $P_{2,n}^{(2)}$ from Eq. (2.31). Substituting this and $P_{1,n}^{(2)}$ into Eq. (2.36) gives the right side of Eq. (2.31) which shows that the pair density is exact to second order. We can also use this approach to show that the error in the pair approximation is $\mathcal{O}(\tau^3)$. To see this, it is sufficient to compare the diagonal terms ($\boldsymbol{\phi} = \boldsymbol{\phi}'$) of the Wigner-Kirkwood expansion. These can be computed by taking the limit $\boldsymbol{\phi} \to \boldsymbol{\phi}'$. In particular for P_3, we get,[69]

$$P_3 = V^3 - V\Delta_{\boldsymbol{\phi}} V - \frac{1}{2}(\nabla_{\boldsymbol{\phi}} V)^2 + \frac{1}{10}\Delta_{\boldsymbol{\phi}}^2 V \tag{2.37}$$

To compare $P_3(\boldsymbol{\phi}, \boldsymbol{\phi})$ to $Q_3(\boldsymbol{\phi}, \boldsymbol{\phi})$, we need to express Q_3 using products and sums of 2-body terms as before,

$$Q_3 = \sum_{n=1}^{N-1} P_{3,n}^{(2)} + 6 \sum_{n<m<l} P_{1,n}^{(2)} P_{1,m}^{(2)} P_{1,l}^{(2)} + \ 3 \sum_{n<m}^{N-1} (P_{2,n}^{(2)} P_{1,m}^{(2)} + P_{1,n}^{(2)} P_{2,m}^{(2)}) \tag{2.38}$$

Using Eqs. (2.37) and (2.38), we find that P_3 and Q_3 agree for all terms in Eq. (2.37) except for $(\nabla_{\boldsymbol{\phi}} V)^2/2$ (see Supplementary Material, Sec. D for details). The exact difference between P_3 and Q_3 takes the form,

$$P_3 - Q_3 = -\sum_{n=2}^{N-1} (\nabla V_{n-1,n})_n (\nabla V_{n,n+1})_n \neq 0 \tag{2.39}$$

Therefore, the error in the pair density is $\mathcal{O}(\tau^3)$. It is also instructive to note that the error function in Eq. (2.39) is a sum of terms that correspond to 3-body correlations. This is unsurprising since we derived the pair approximation by neglecting all higher than 2-body correlations. Moreover, in the higher order terms in τ the pair factorization again accounts for 2-body correlations exactly. Consequently, for those terms as well, we expect that the error would arise due to higher than 2-body correlations. This means that the pair factorization leads to much smaller error coefficients (in powers of τ) when 2-body correlations dominate the behavior of a system. Therefore, for a given τ, we see far less systematic error in such regimes compared to the symmetric Trotter factorization even though the latter also has error $\mathcal{O}(\tau^3)$. In regimes where many-body correlations become significant, the pair factorization error increases.

2.2.4 Path Integral Ground State Estimators

We will use the pair approximation to compute ground state properties via Path Integral Ground State (PIGS). In this paradigm, ground state operator expectation values are computed as,[16]

$$\langle O \rangle = \frac{1}{Z} \langle \Psi_T | e^{-\frac{\beta H}{2}} O e^{-\frac{\beta H}{2}} | \Psi_T \rangle \tag{2.40}$$

where Z is the pseudo-partition function,

$$Z = \langle \Psi_T | e^{-\beta H} | \Psi_T \rangle \tag{2.41}$$

For this work, we will restrict to the constant trial wave-function in the position representation ($\langle \boldsymbol{\phi} | \Psi_T \rangle = 1/\sqrt{2\pi}$). The PIGS ground state energy estimator is given by,[16,20]

$$E_0 = A \int d\boldsymbol{\phi}_0 ... d\boldsymbol{\phi}_P \prod_{i=0}^{P-1} \rho(\boldsymbol{\phi}_i, \boldsymbol{\phi}_{i+1}, \tau)\ V(\boldsymbol{\phi}_P) \tag{2.42}$$

where $A = 1/2\pi Z$. Expanding $\rho(\tau)$ using the pair approximation from Eq. (2.17), we get,

$$E_0 = A \int d\boldsymbol{\phi}_0 ... d\boldsymbol{\phi}_P \prod_{i=0}^{P-1} \rho_0(\boldsymbol{\phi}_i, \boldsymbol{\phi}_{i+1}, \tau) \prod_{j=1}^{N-1} \frac{\rho_j^{(2)}(\phi_i^j, \phi_i^{j+1}, \phi_{i+1}^j, \phi_{i+1}^{j+1}, \tau)}{\rho_{0,j}^{(2)}(\phi_i^j, \phi_i^{j+1}, \phi_{i+1}^j, \phi_{i+1}^{j+1}, \tau)}\ V(\boldsymbol{\phi}_P) \tag{2.43}$$

In addition to the energy, we also want to study structural properties. Since these are diagonal in the position representation, they can be evaluated using Eq. (2.40). In particular,

we need to compute the angular correlation,

$$C = \sum_{i=1}^{N-1} \cos(\phi^i - \phi^{i+1}) \tag{2.44}$$

The PIGS estimator for this is given by,

$$C_0 = A \int d\boldsymbol{\phi}_0 ... d\boldsymbol{\phi}_P \prod_{i=0}^{P-1} \rho_0(\boldsymbol{\phi}_i, \boldsymbol{\phi}_{i+1}, \tau) \prod_{j=1}^{N-1} \frac{\rho_j^{(2)}(\phi_i^j, \phi_i^{j+1}, \phi_{i+1}^j, \phi_{i+1}^{j+1}, \tau)}{\rho_{0,j}^{(2)}(\phi_i^j, \phi_i^{j+1}, \phi_{i+1}^j, \phi_{i+1}^{j+1}, \tau)} \, C(\boldsymbol{\phi}_{P/2}) \tag{2.45}$$

Finally, we also need to compute the Binder ratio defined as,[19,94]

$$U = 1 - \frac{\langle M_x^4 \rangle}{3\langle M_x^2 \rangle^2} \tag{2.46}$$

where $M_x = \frac{1}{N} \sum_{i=1}^{N} \cos(\phi_i)$ is the net polarization across the chain. The second and fourth powers of the polarization are given by,

$$M_x^2 = \frac{1}{N^2} \sum_{i,j=1}^{N} \cos(\phi_i) \cos(\phi_j) \tag{2.47}$$

$$M_x^4 = \frac{1}{N^4} \sum_{i,j,k,l=1}^{N} \cos(\phi_i) \cos(\phi_j) \cos(\phi_k) \cos(\phi_l) \tag{2.48}$$

M_x^k for $k \in \{2, 4\}$ is diagonal in the position representation so it can be computed using an estimator analogous to Eq. (2.45),

$$\begin{aligned} M_{x,0}^k = A \int d\boldsymbol{\phi}_0 ... d\boldsymbol{\phi}_P \prod_{i=0}^{P-1} \rho_0(\boldsymbol{\phi}_i, \boldsymbol{\phi}_{i+1}, \tau) \\ \times \prod_{j=1}^{N-1} \frac{\rho_j^{(2)}(\phi_i^j, \phi_i^{j+1}, \phi_{i+1}^j, \phi_{i+1}^{j+1}, \tau)}{\rho_{0,j}^{(2)}(\phi_i^j, \phi_i^{j+1}, \phi_{i+1}^j, \phi_{i+1}^{j+1}, \tau)} \, M_x^k(\boldsymbol{\phi}_{P/2}) \end{aligned} \tag{2.49}$$

The Binder parameter defined above measures the excess kurtosis of the net polarization distribution. It is typically used in Monte Carlo (MC) simulations of continuous phase transitions for identifying the transition point as well as for determining the correlation length critical exponent via scaling analyses.

2.2.5 Discrete Variable Representation

To optimize our path integral simulations, we use the Colbert-Miller[44] Discrete Variable Representation (DVR)[45,46] to discretize the continuous angular degrees of freedom. In this discretization scheme, the grid points for each ϕ are linearly spaced,

$$\{\phi : \phi \in [0, 2\pi)\} \to \{2\pi j/M : j \in 0, ..., M-1\} \tag{2.50}$$

where $M = 2l + 1$ and l is the number of kinetic energy eigenstates used to construct the DVR representation. The 1-body kinetic energy operator is given by the matrix,[44]

$$\begin{aligned} K^{(1)}_{i,j} &= \langle 2\pi i/M | K^{(1)} | 2\pi j/M \rangle \\ &= \frac{d(d+1)}{3}, \text{ for } i = j \qquad (2.51) \\ &= (-1)^{i-j} \frac{\cos(\pi(i-j)/M)}{2\sin^2(\pi(i-j)/M)}, \text{ for } i \neq j \qquad (2.52) \end{aligned}$$

The 2-body potential operator is diagonal in this representation,

$$V^{(2)}_{ijkl} = \langle 2\pi i/M, 2\pi j/M | V^{(2)} | 2\pi k/M, 2\pi l/M \rangle = V^{(2)}(2\pi i/M, 2\pi j/M)\delta_{ik}\delta_{jl} \tag{2.53}$$

where $V^{(2)}$ here is given by the Eq. (2.3). We will use this discretization scheme to cast our path integrals into path sums.[20]

To do this, first note that the required 2-body Hamiltonian $H^{(2)}$ (Eq. (2.14)) can be computed as a matrix using the DVR representations of K and V provided above. Then, the corresponding 2-body propagator required for the pair approximation can be numerically tabulated in the DVR position representation. Similarly, we can diagonalize the matrix associated with K_i in the DVR to compute the 1-body free propagator. To use the pair density in path integral simulations, we need to tabulate the following two tensors,

$$A^{kl}_{ij} = \frac{\langle 2\pi i/M, 2\pi j/M | e^{-\tau H^{(2)}} | 2\pi k/M, 2\pi l/M \rangle}{\langle 2\pi i/M, 2\pi j/M | e^{-\tau K^{(2)}} | 2\pi k/M, 2\pi l/M \rangle} \tag{2.54}$$

$$B^j_i = \langle 2\pi i/M | e^{-\tau K^{(1)}} | 2\pi j/M \rangle \tag{2.55}$$

B allows us to sample the free propagator part in Eq. (2.17) and A is stored to sample the 2-body effective potential part in Eq. (2.17). Note that B is a rank 2 tensor which can be

stored as a table as specified. To store A as a matrix, we can use lexicographic ordering to get,

$$A_i^j = A_{i_1,i_2}^{j_1,j_2} \tag{2.56}$$

$$i_1 = \lfloor i/M \rfloor, \quad i_2 = i - i_1 M, \quad j_1 = \lfloor j/M \rfloor, \quad j_2 = j - j_1 M \tag{2.57}$$

Both A_i^j and B_i^j are computed and tabulated before the MC run to minimize on-the-fly calculations.

2.2.6 Sequentially Gibbs Sampling The Pair Density

To estimate the ground state properties specified by Eqs. (2.42), (2.45) and (2.49), we use Markov chain Monte Carlo (MCMC) integration[74] with a sequential Gibbs sampler.[75] Consider the pair factorization probability density,

$$P(\Omega, \tau) = \prod_{i,j} \rho_0(\boldsymbol{\phi}_i, \boldsymbol{\phi}_{i+1}, \tau) \frac{\rho_j^{(2)}(\boldsymbol{\phi}_i, \boldsymbol{\phi}_{i+1}, \tau)}{\rho_{0,j}^{(2)}(\boldsymbol{\phi}_i, \boldsymbol{\phi}_{i+1}, \tau)} \tag{2.58}$$

Here, i is the bead index, j is the particle index and $\Omega = (\boldsymbol{\phi}_1, ..., \boldsymbol{\phi}_P)$. In Gibbs sampling, the system moves are determined using conditional probabilities on a discrete state space. We can use our pre-computed probability tables A_{ijkl} and B_{ij} to determine the conditional probabilities for the pth bead and nth rotor coordinate as follows,

$$P(\phi_p^n(t+1) = 2\pi j/M | \Phi(t, t+1)) = \frac{P_B P_A}{P_M} \tag{2.59}$$

where, t is the MC simulation time-step and P_A, P_B and P_M are given by,

$$P_B = B_{i_2}^j B_j^{i_8} \tag{2.60}$$

$$P_A = A_{i_1,i_2}^{i_4,j} A_{i_2,i_3}^{j,i_6} A_{i_4,j}^{i_7,i_8} A_{j,i_6}^{i_8,i_9} \tag{2.61}$$

$$P_M = \sum_k A_{i_1,i_2}^{i_4,k} A_{i_2,i_3}^{k,i_6} A_{k,i_6}^{i_8,i_9} A_{i_4,k}^{i_7,i_8} B_{i_2}^k B_k^{i_8} \tag{2.62}$$

The variable being conditioned on in Eq. (2.59) is the configuration vector $\Phi(t, t+1)$,

$$\Phi(t, t+1) = (\boldsymbol{\phi}_0(t+1), ..., \tilde{\boldsymbol{\phi}}_p(t, t+1), ..., \boldsymbol{\phi}_P^N(t)) \tag{2.63}$$

Here, the components of the vector in Eq. (2.63) take the form,

$$\boldsymbol{\phi}_k(s) = (\phi_k^1(s), ..., \phi_k^N(s)),\ 0 \leq k \leq P, k \neq p \tag{2.64}$$

$$\tilde{\boldsymbol{\phi}}_p(t, t+1) = (\phi_p^1(t+1), ..., \phi_p^{n-1}(t+1), \phi_p^{n+1}(t), ..., \phi_p^N(t)) \tag{2.65}$$

The indices i_l for $l \in \{1, 2, 3, 7, 8, 9\}$ in Eqs. (2.60), (2.61) and (2.62) are defined by,

$$\phi_{p-1}^{n-2+l}(t) = \frac{2\pi i_l}{M}, \quad l \in \{1, 2, 3\} \tag{2.66}$$

$$\phi_{p+1}^{n-8+l}(t+1) = \frac{2\pi i_l}{M}, \quad l \in \{7, 8, 9\} \tag{2.67}$$

Similarly, indices i_4 and i_6 are defined by,

$$\phi_p^{n-1}(t+1) = \frac{2\pi i_4}{M}, \quad \phi_p^{n+1}(t) = \frac{2\pi i_6}{M} \tag{2.68}$$

Eqs. (2.60), (2.61) and (2.62) above correspond to n, p such that $0 < p < P$, $1 < n < N$. For the terminal bead and rotor indices ($p = 0$, $p = P$, $n = 1$ or $n = N$), at least one of $p \pm 1$ or $n \pm 1$ would be undefined. Therefore, terms containing i_l for such an l would simply be excluded. In the sequential Gibbs sampling algorithm, we iterate over all the beads and all the rotors in each step.[75] For each of the $N(P+1)$ variables, we then compute the conditional probabilities of the M possible moves (Eq. (2.59)) and then uniformly sample the distribution associated with said probabilities.[95]

Fig. 2.2 compares the sampling approaches for the pair and symmetric Trotter factorization in the context of Gibbs sampling. For the pair factorization, to calculate each transition probability, we need to account for the configurations of all the surrounding particles in NP-space. In this context, the symmetric Trotter propagator is simpler since the transition probability only depends on the $(p, n \pm 1)$ and $(p \pm 1, n)$ particle configurations. Note that in Fig 2.2, we exhibit the case for $(p, n) = (0, 1)$ for simplicity. For non-terminal beads and rotors, analogous terms for other surrounding variables would also be present as in Eqs. (2.60), (2.61) and (2.62). The advantage of Gibbs sampling is that it is rejection-free. Moreover, using an optimized grid such as the Colbert-Miller DVR means that M is small which also optimizes the simulation performance. In particular, for this problem, $M = 5$ is sufficient to converge to the exact results.[20]

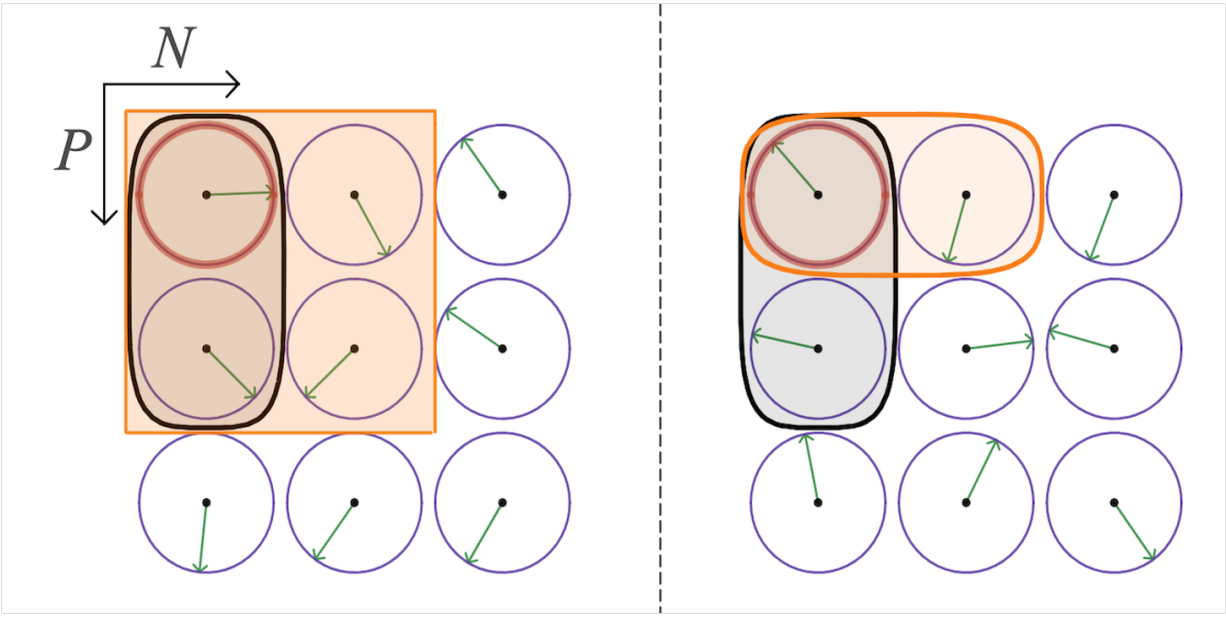


Figure 2.2: Comparison of sampling probability calculations between the pair and symmetric Trotter factorizations in the context of Gibbs sampling. For simplicity, we compare the $p = 0, n = 1$ variable in NP-space. The left panel corresponds to the pair factorization while the right panel exhibits the case for symmetric Trotter factorization. The top-left 4 shaded rotors in the left panel represent A^{i_7,i_8}_{j,i_6} whereas the grey vertical region encapsulating the first rotor represents $B^{i_7}_j$. $B^{i_7}_j$ is also present in the Trotter case since it represents the free particle density. However, for symmetric Trotter, we have a 2-body term: $e^{-\tau V_{j,i_6}}$ instead of the 4-body A^{i_7,i_8}_{j,i_6} term needed for the pair approximation case.

2.2.7 The Sign Problem

It is worth noting that using the DVR representation for computing propagators can lead to negative density matrix elements when τ is very small (which happens when the number of beads being used is large). This can be seen by considering the first order Taylor expansion of the 1-body free propagator in τ,

$$\langle 2\pi i/M|e^{-\tau K^{(1)}}|2\pi j/M\rangle \approx \delta_{ij} - \tau K^{(1)}_{ij} \tag{2.69}$$

Since $K^{(1)}_{ij}$ is non-stoquastic[96] (has positive off-diagonal matrix elements), the off-diagonal matrix elements of Eq. (2.69) can be negative for small τ. This is problematic because

density matrix elements are used to assign probabilities to different configurations in a MC simulation which makes negative definite densities unusable in this context. It can also be shown that when τ is large, there is no sign problem in the free propagator. Moreover, the critical value of τ such that this issue arises in the free propagator depends on the number of grid points M. It was computationally shown in Ref. 20 that for $M = 5$, the critical τ value is approximately 0.2.

The same argument as that used for the free propagator shows that for small enough τ, the 2-body effective potential part of the pair propagator given in Eq. (2.54) can have negative density matrix elements. However, unlike the free propagator, this can not be circumvented by increasing the number of grid points. For our simulations, when we encounter the sign problem with the pair propagator, we keep track of the overall sign of Eq. (2.17) during the simulation and multiply the estimators by that sign.[97] While we can use this approach for mild sign problems such as the one we encounter in our simulations, it should be noted that if the sign problem is severe, this approach can make the integrand oscillatory and lead to an exponential slowdown in MC convergence.

It is important to note here that the sign problem discussed above is not an inherent quality of the propagators. It arises due to the non-stoquastic nature of the DVR representation of the kinetic energy operator. This also, in turn, makes the 2-body Hamiltonian matrix in the DVR representation non-stoquastic because the off-diagonal entries of the Hamiltonian correspond to the off-diagonal entries of the kinetic energy operator in the position basis. Since the sign problem is a basis dependent property, it is entirely possible that there exists a different representation which does not suffer from this non-stoquasticity and the corresponding sign-problem.

2.2.8 Numerical Matrix Multiplication

For small systems, we test our approach using Numerical Matrix Multiplication (NMM).[98] This involves casting our path integral (Eq. (2.40)) as a matrix multiplication problem,

$$\langle f \rangle = \frac{1}{Z} \left(\prod_{j=1}^{P/2} \hat{\rho} \right) \hat{f} \left(\prod_{j=1}^{P/2} \hat{\rho} \right) \tag{2.70}$$

where $\hat{\rho}$ is the high temperature density matrix in the position representation and $\hat{f}$ represents the matrix associated with the property f in the position representation. The

product in Eq. (2.70) is matrix multiplication. For our work, we construct the pair density for 3 rotors as follows,

$$\rho_{ijk}^{lmn} = B_i^l B_j^m B_k^n A_{ij}^{lm} A_{jk}^{mn} \tag{2.71}$$

where B and A are the matrices constructed in Sec. 2.2.5. ρ_{ijk}^{lmn} can be represented as a matrix using lexicographic ordering,

$$\hat{\rho}_{rs} = \rho_{ijk}^{lmn}, \quad r = iM^2 + jM + k, \quad s = lM^2 + mM + n \tag{2.72}$$

2.3 Results & Discussion

2.3.1 Convergence Studies

We first determine the PIGS ground state energy estimator (as defined in Eq. (2.42)) extrapolation function in the limit of $\tau \to 0$ computationally. This is done by fitting the pair propagated NMM energy results for $66 \leq P \leq 100$. As for all other results in this work, we use $\beta = 10.0$ since that has been shown to be sufficient for PIGS convergence in past work.[20] Fig. 2.3 show the convergence fits corresponding to $N = 3$, $M = 5$ and $g = 1.0$. We compare three different fitting functions: linear ($E_0(\tau) = E_0 + \tau b$), quadratic ($E_0(\tau) = E_0 + \tau^2 b$) and cubic ($E_0(\tau) = E_0 + \tau^3 b$).

The error bars at $\tau = 0$ represent the fitting errors for each of the extrapolations. The quadratic function fits the NMM data and converges to the correct energy. This is unsurprising since the density error (as in the case of the symmetric Trotter approximation) is $O(\tau^3)$ and we know from previous work that the asymptotic behaviour in the limit of $\tau \to 0$ is well described by quadratic fitting functions for the symmetric Trotter factorization.[55,99] The exact ground state energy for this result is calculated by diagonalizing the 3-body Hamiltonian to calculate the corresponding PIGS estimate using Eq. (2.40),

$$\langle E_0 \rangle = \frac{1}{Z} \sum_{i,j,k} \langle \boldsymbol{\phi}_i | E_k \rangle \langle E_k | \boldsymbol{\phi}_j \rangle E_k e^{-\beta E_k} \tag{2.73}$$

$$Z = \sum_{i,j,k} \langle \boldsymbol{\phi}_i | E_k \rangle \langle E_k | \boldsymbol{\phi}_j \rangle e^{-\beta E_k} \tag{2.74}$$

This is done instead of obtaining E_0 by diagonalizing H so as to include the effects of using a finite β in the fit comparison.

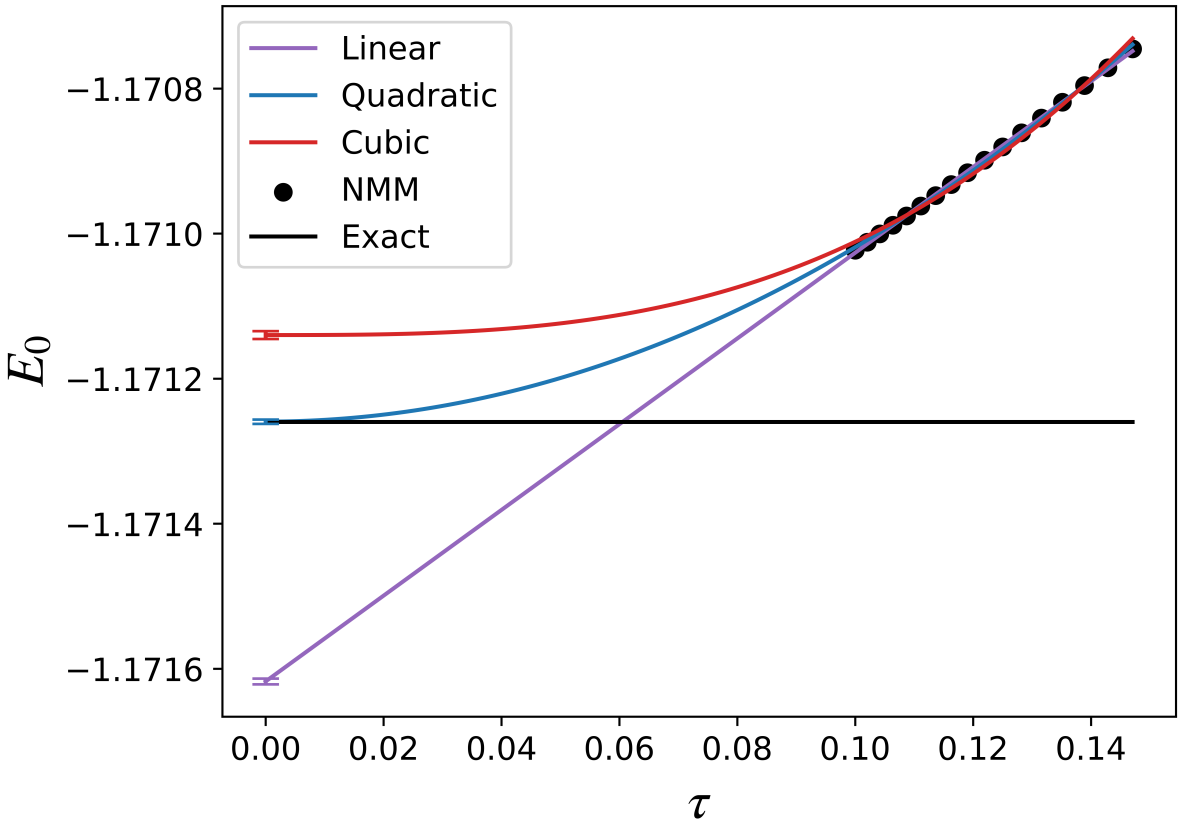


Figure 2.3: NMM fit comparison results with the pair propagator for $N = 3$, $g = 1.0$ and $M = 5$. Exact ground state energy results are plotted for comparison.

To benchmark the performance of the pair action against the symmetric Trotter factorization scheme, we first use NMM to compute the ground state energy for 3 rotors. Fig. 2.4 shows the results with $M = 5$ and $g = 1.0$. Exact Diagonalization (ED) results are plotted for comparison. The primitive propagator here corresponds to the symmetric Trotter approximation and both extrapolations used quadratic fitting functions. The pair factorization converges much faster than the typically used primitive factorization. As discussed above, this is because our potential is pair-wise additive which means that the 2-body correlation effects are significant. These are accounted for exactly by the pair approximation.

Practically, this implies that the pair approximation should yield a significant benefit in

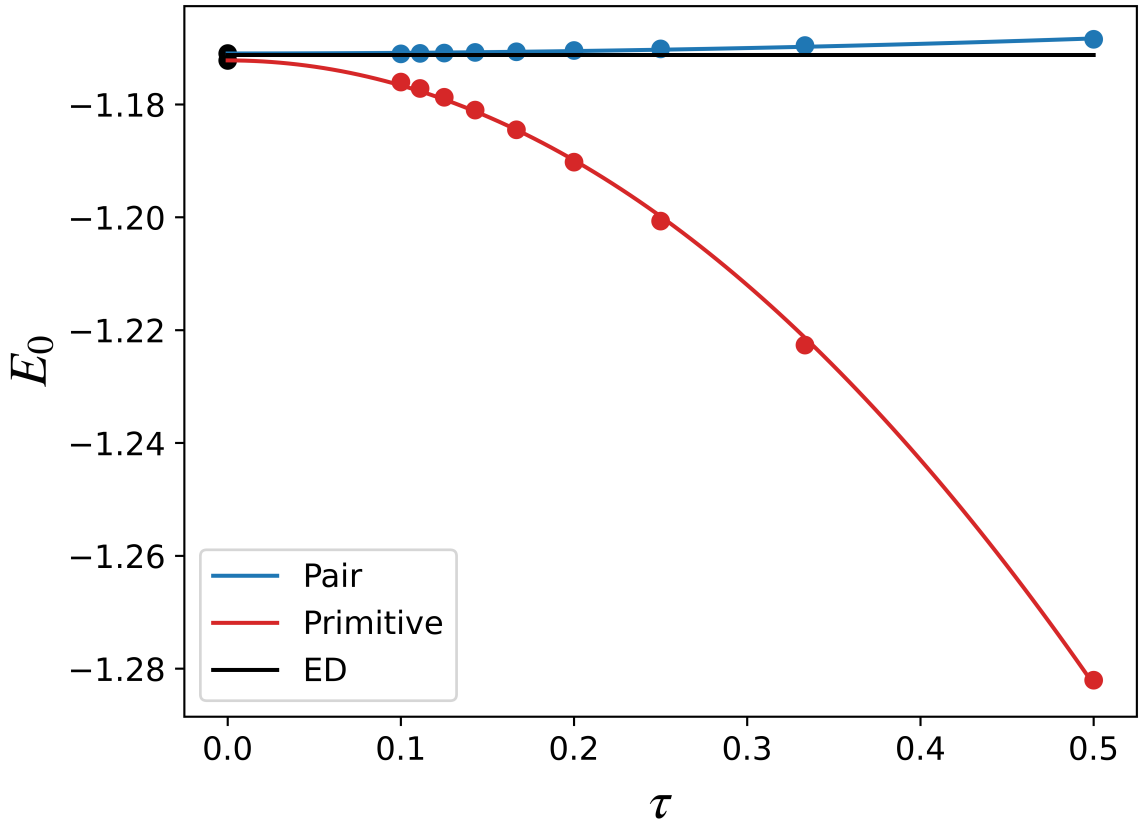


Figure 2.4: Comparison of NMM ground state energy convergence in τ for the pair and primitive propagators for $N = 3$. Here, $M = 5$ and $g = 1.0$.

terms of efficiency when simulating many-body systems of rotating molecules with pairwise interactions. This is particularly useful in PIMC simulations where smaller τ values correspond to more degrees of freedom in the simulation. Therefore, improving convergence via better actions can greatly increase the efficiency of MC simulations and allow us to computationally probe previously intractable regimes.[11]

Fig. 2.5 exhibits the τ convergence comparison between the primitive and pair propagators for $N = 100$. The ground state energy here was calculated using DVR-Gibbs MC simulations. DMRG results are used to estimate the exact ground state energy for this case since ED is unfeasible in the many-body regime. For these simulations as well, $g = 1.0$ and $M = 5$. Note that the primitive approximation requires more beads for convergence

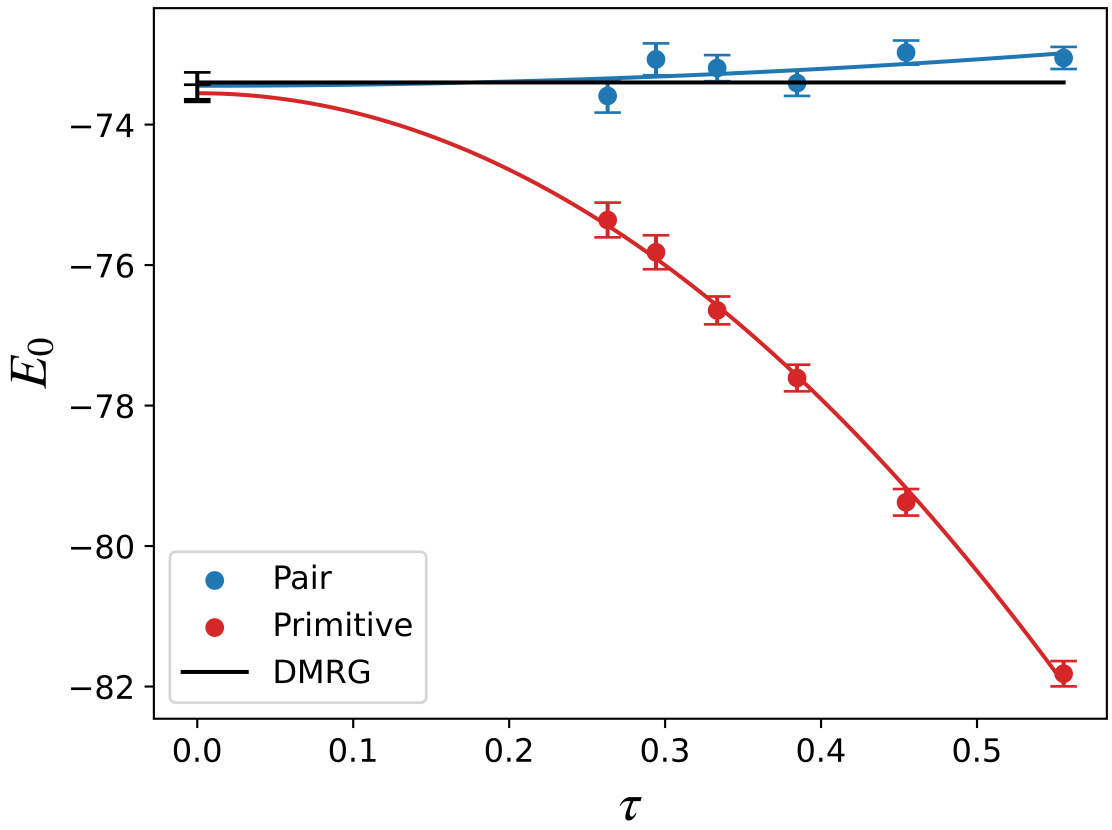


Figure 2.5: Comparison of MC ground state energy convergence in τ for the pair and primitive propagators for $N = 100$. Here, $M = 5$ and $g = 1.0$. DMRG results are plotted to exhibit the exact value of the ground state energy.

compared to the pair approximation. However, using larger numbers of beads leads to simulations with smaller τ which, in the context of DVR-Gibbs can result in the sign problem causing an exponential slowdown in convergence. Using a better action such as the pair propagator is very useful for such cases as well since it could then be used to attain convergence with a larger τ, thus circumventing the sign problem.

2.3.2 Energetic Properties

Fig. 2.6 shows the ground state energy computed using the pair propagator for a chain of 150 planar rotors. For these results $M = 10$ and 200000 steps were used in the MC

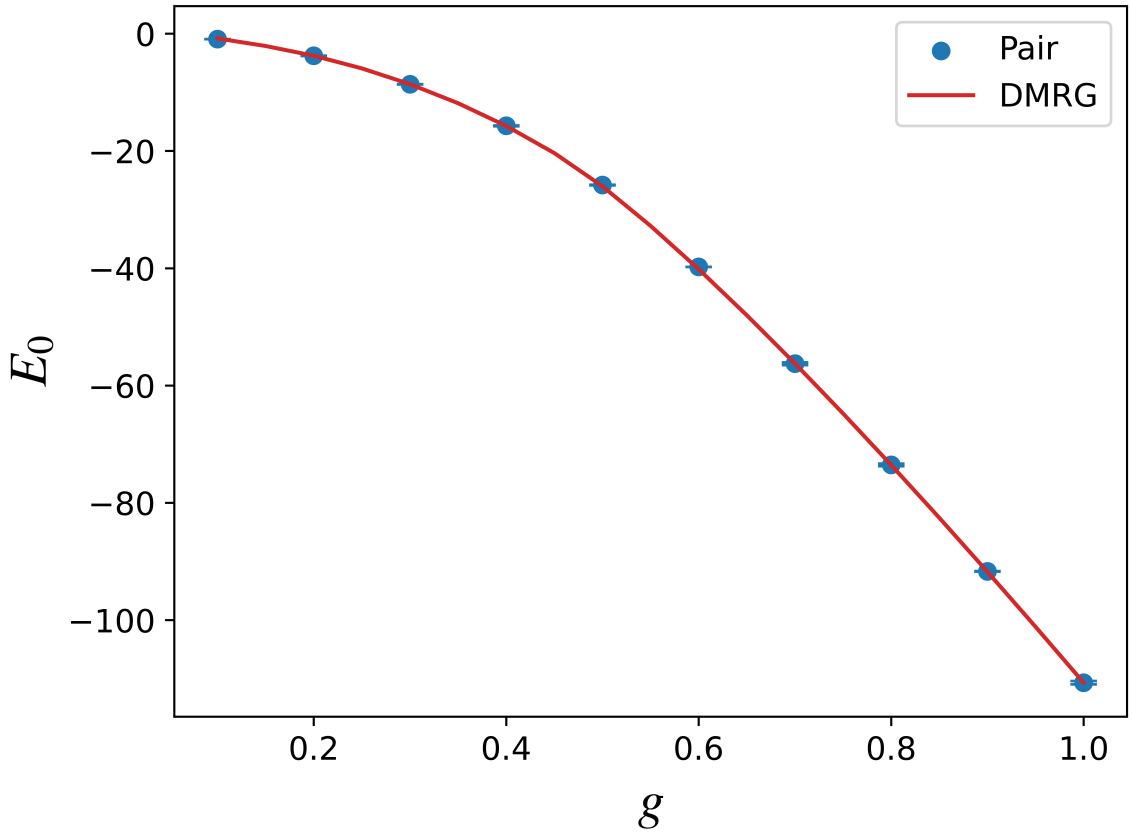


Figure 2.6: Ground state energy as a function of g for $N = 150$ computed using the pair factorization compared to DMRG results.

simulation. All of the MC energy results were computed by extrapolation using quadratic fits with $P \in \{20, 40, 60\}$. The larger value of M was used to avoid the sign problem in the free DVR propagator for $P = 60$. DMRG results are plotted for comparison which were calculated using $M = 5$. Details about our DMRG implementation can be found in Ref. 19, which uses the iTensor package[100] for calculations. The pair DVR MC approach yields excellent agreement with our DMRG simulations.

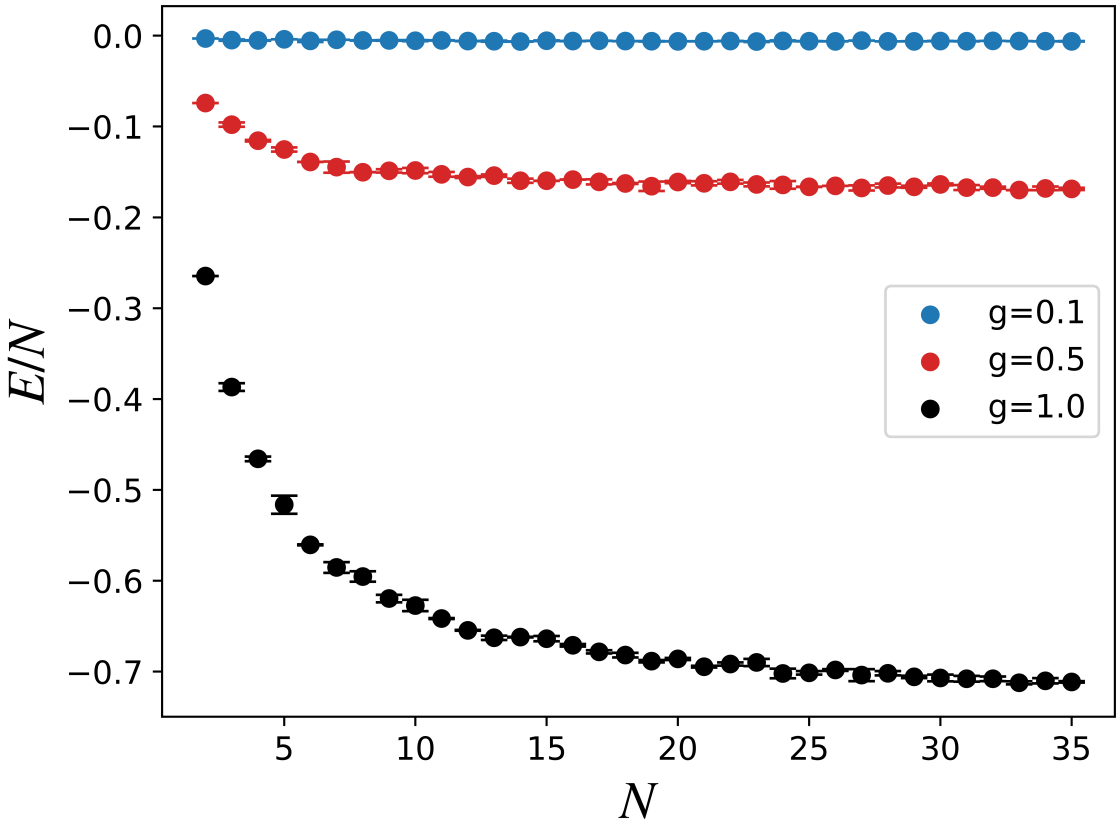


Figure 2.7: Ground state energy per particle as a function of N computed using the pair factorization approach for $g = 0.1$, $g = 0.5$ and $g = 1.0$.

Fig. 2.7 shows the energy per particle for this system computed using the pair propagator for $g \in \{0.1, 0.5, 1.0\}$. For $g = 0.1$, the energy per particle converges very quickly due to the weak interactions. The $1/N$ behaviour of E/N suggests a linear model for the ground state energy as a function of N,

$$E = \mu N + c \tag{2.75}$$

where μ is the chemical potential. As g is increased, larger values of N are necessary for convergence to μ. In particular for this system, we find that $N = 35$ is sufficient in all three of these cases to see reasonable convergence in E/N.

2.3.3 Structural Properties

Fig. 2.8 shows the correlation as a function of coupling strength compared to DMRG. For $g < 0.5$, the system is in the disordered phase where the orientational correlation is close to 0. For $g > 0.6$, the system is in the ordered phase which corresponds to higher orientational correlations. For both of these regimes, we found that simulating the system with 60 beads was sufficient for convergence to DMRG results. Three parallel simulation results were aggregated for all values of g to generate the results shown in Fig. 2.8; one initialized with all rotors oriented along the $+x$ axis, another with all rotors oriented along the $-x$ direction and a final one with all starting rotor orientations selected randomly using a uniform distribution. These starting configurations were picked to mimic the ground states of the system in the disordered and ordered phases. The former corresponds to randomly selected rotor orientations while the latter corresponds to the left and right polarized configurations.[19]. For each of these runs, we used 100000 steps. The error bars in Fig. 2.8 correspond to the statistical errors from the MC simulation.

For $g = 0.5$ and $g = 0.6$, we see a drop in convergence to the DMRG results. However, increasing the number of beads from $P = 60$ to $P = 100$ improves the agreement between the two simulations at $g = 0.6$. One possible reason for this is that near criticality, many-body correlations become significant as the correlation length increases.[19] The pair factorization only accounts for all 2-body correlations exactly and (as indicated by the error term in the series expansion given in Eq. (2.39)), higher than 2-body correlations determine the error in the pair propagated paths. Therefore, when we increase the number of beads, we decrease this systematic error by reducing τ. At $g = 0.5$, the improvement due to increasing P is less significant since we are closer to the transition point. For the simulation with $P = 100$, we used $M = 14$ and kept track of the sign to account for the mild sign problem despite the larger M value. This calculation was initialized with all rotors pointing in the $+x$ direction. The error bars for all g correspond to statistical errors from the MC simulations. The number of simulation steps used for the $P = 100$ run was 300000. We used a standard binning procedure[74] to compute the statistical estimates for the orientational correlation throughout. We neglected the first 10000 points in all of our correlation simulations to allow for the Markov chain to sufficiently equilibrate.

Fig. 2.9 shows the Binder ratio as a function of g computed using the pair propagator compared to DMRG for $N = 150$. For this system, previous work has shown that in the disordered phase, $U = 0$ and for the ordered phase, $U > 0$.[19] For all of these points, the MC

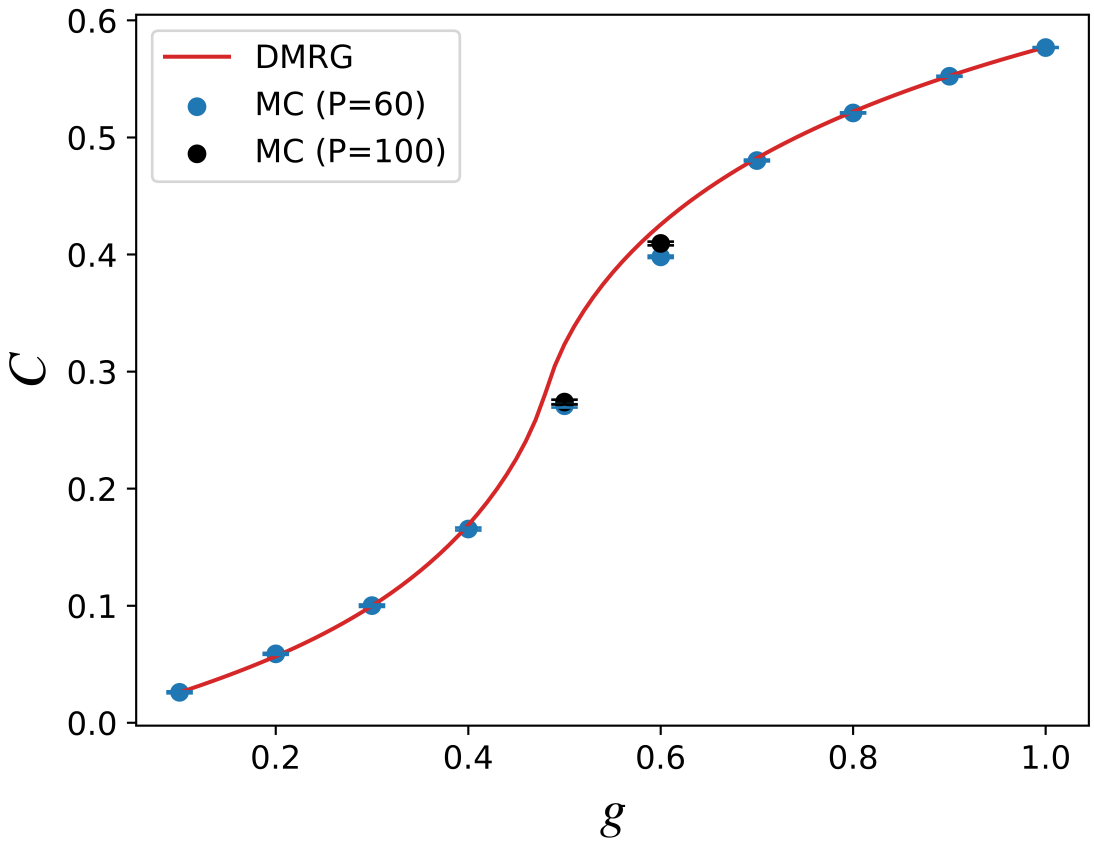


Figure 2.8: Correlation as a function of g for $N = 150$ computed using the pair factorization compared to DMRG results. The MC results corresponding to $P = 60$ were computed with $M = 10$, and 3 parallel simulations (100000 steps each) with different starting configurations. The MC points corresponding to $P = 100$ were computed with $M = 14$ and 300000 steps.

results were computed with $P = 60$, $M = 10$ and 100000 steps. The system was initialized with all rotors along the $+x$ direction. We see good agreement with DMRG here as well and we find that we do not need to increase P to converge to the DMRG results for the Binder ratio. However, the Binder ratio is more sensitive to the equilibration procedure and Markov chain auto-correlation near the phase transition. For $g < 0.5$, we use a burn-in period of 20000 points for equilibration. For $g > 0.5$, we do not need to equilibrate at all since the starting configuration mimics the ground state configuration of the physical

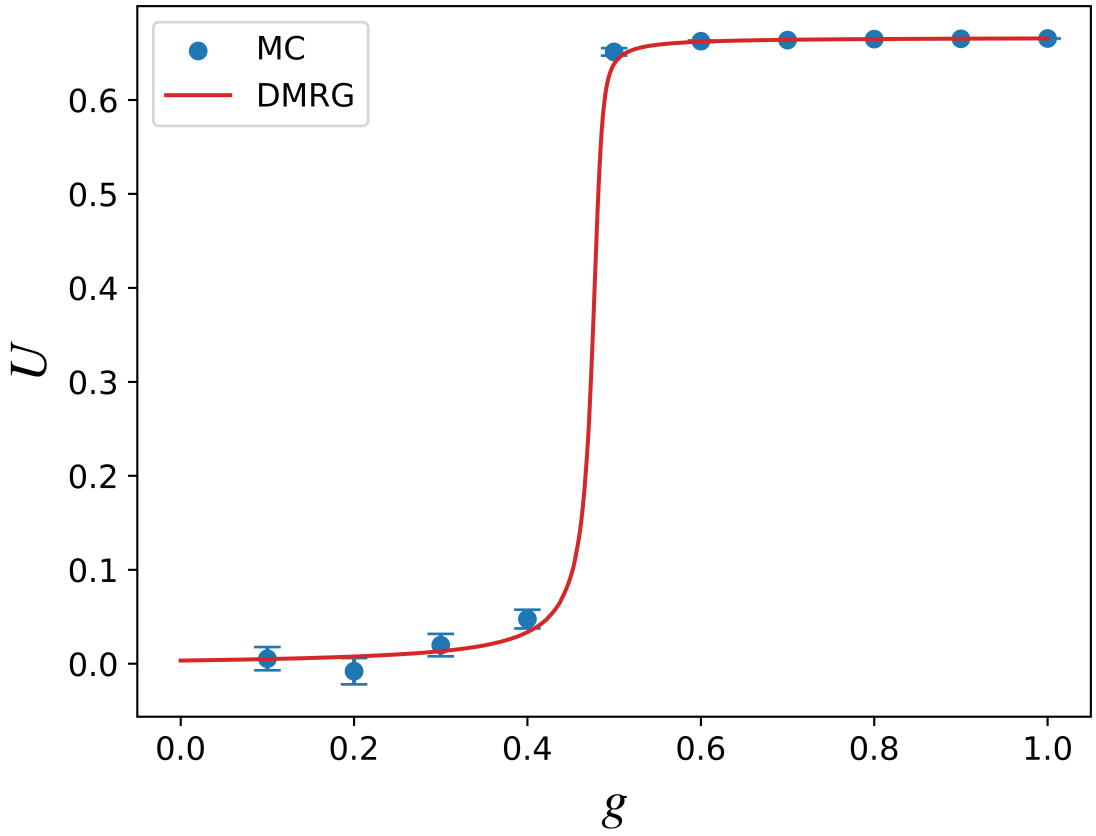


Figure 2.9: Binder ratio as a function of g for $N = 150$ computed using the pair factorization compared to DMRG results. For all values of g, the MC results were computed with $P = 60$, $M = 10$, and 100000 steps. The system was initialized with all rotors pointing in the $+x$ direction.

system. For $g = 0.5$ and $g = 0.6$, we are close to the critical region where the system has longer range correlations.[19] Consequently, we need a much larger burn-in period for the chain to converge to the equilibrium distribution since our algorithm relies on local moves. For the Binder ratio at $g = 0.5$ and $g = 0.6$ in Fig. 2.9, we found that we needed to neglect the first 99000 points to see good agreement with the DMRG results. For the Binder ratio estimates, we used jack-knife analysis[74] since that is more suitable for evaluating functions of random variables computed using correlated samples (we used the same simulation to compute $M^2_{x,0}$ and $M^4_{x,0}$ and the Binder ratio is a function of these two as specified in

Eq. (2.46)). We also neglected 5 points between consecutive samples to account for MC correlations.

2.4 Conclusions

In this work, we developed the pair-DVR PIMC approach to study the ground state properties of a linear chain of planar rotors with nearest-neighbor dipolar interactions. When it was initially introduced, the pair density was used in the context of Cartesian coordinates. We also analyzed the pair factorization path integral density error in powers of imaginary time using Wigner-Kirkwood expansions[68,69] and showed that the error is $\mathcal{O}(\tau^3)$ for our simulations. Computationally, we used the DVR-Gibbs sampling paradigm[20] to study the energetic and structural properties of our system as functions of g and N. We also showed that the pair factorization converges much faster than the symmetric Trotter approximation in τ. This is because for a pair-wise interaction, the equilibrium configuration is dominated by 2-body correlations which are captured exactly by the pair propagator. Therefore, the sampled paths are much closer to the exact paths ($\tau \to 0$ limit) than those sampled using the symmetric Trotter factorization, for a given P. We compared our results to DMRG and found good agreement for structural as well energetic properties in the large N limit. This was done not only to exhibit the utility of our approach in the context of improving our path integral simulation capabilities, but also to study the behavior of the pair approximation near criticality.

This system undergoes a quantum phase transition at $g \approx 0.5$.[19] Here, we find that we need more beads to converge to the correct results near the phase transition. One possible reason for this is that the correlations lengths get longer near the critical point and since the pair action only accounts for all 2-body correlations exactly, we have more systematic error in that region when using the pair factorization. Moreover, in our Binder ratio computations, we find that our sequential sampling techniques experience critical slowing down[21] near $g \approx 0.5$ because our simulations require a large number of steps for equilibration. This underscores the necessity for adapting algorithms suitable for quantitatively studying phase transitions (for instance, the Wolff algorithm[21]) to rotational degrees of freedom with chemically relevant potentials such as those that employ dipolar and quadrupolar interactions. However, further research is needed to determine the utility of such approaches for dipolar rotor lattices.

2.5 Supplementary Material

Here, we provide some additional results pertaining to the pair propagator asymptotic error analysis that were omitted from the main text for the sake of brevity.

2.5.1 Green's Function Differential Equation

In the main text, we use the following differential equation for the quotient ($F(\boldsymbol{\phi}, \boldsymbol{\phi}', \tau)$) given by dividing the density matrix elements corresponding to the full Hamiltonian ($\rho(\boldsymbol{\phi}, \boldsymbol{\phi}', \tau)$) by the free propagator matrix elements (($\rho_0(\boldsymbol{\phi}, \boldsymbol{\phi}', \tau)$),

$$\left(\frac{\partial}{\partial \tau} - \Delta_{\boldsymbol{\phi}} - 2\frac{\nabla_{\boldsymbol{\phi}}\rho_0}{\rho_0} \cdot \nabla_{\boldsymbol{\phi}} + V\right) F = 0, \quad F = \rho/\rho_0 \tag{2.76}$$

This can be derived using the Bloch equation for the free and the full propagators,

$$\left(\frac{\partial}{\partial \tau} + H\right) \rho(\boldsymbol{\phi}, \boldsymbol{\phi}', \tau) = 0, \quad \lim_{\tau \to 0} \rho(\boldsymbol{\phi}, \boldsymbol{\phi}', \tau) = \delta(\boldsymbol{\phi} - \boldsymbol{\phi}') \tag{2.77}$$

$$\left(\frac{\partial}{\partial \tau} + K\right) \rho_0(\boldsymbol{\phi}, \boldsymbol{\phi}', \tau) = 0, \quad \lim_{\tau \to 0} \rho_0(\boldsymbol{\phi}, \boldsymbol{\phi}', \tau) = \delta(\boldsymbol{\phi} - \boldsymbol{\phi}') \tag{2.78}$$

To see this, note that $H = K + V$ and $K = -\Delta_{\boldsymbol{\phi}}$. Moreover, using our ansatz, we have that $\rho = F\rho_0$. Using this with Eq. (2.77), we get,

$$F\left(\frac{\partial \rho_0}{\partial \tau} - \Delta_{\boldsymbol{\phi}}(\rho_0)\right) + \frac{\partial F}{\partial \tau}\rho_0 - \rho_0 \Delta_{\boldsymbol{\phi}}(F) - 2\nabla_{\boldsymbol{\phi}}(\rho_0) \cdot \nabla_{\boldsymbol{\phi}}(F) + VF\rho_0 = 0 \tag{2.79}$$

Eq. (2.78) implies that the first term in the above equation is 0. Dividing the resulting equation by ρ_0 yields Eq. (2.76).

2.5.2 Rotational Free Propagator Asymptotics

The many-body free propagator is a product of single particle free propagators which yields,

$$\rho_0(\boldsymbol{\phi}, \boldsymbol{\phi}', \tau) = \prod_{i=1}^{N} \rho_0^{(1)}(\phi^i, \phi'^i, \tau) \Rightarrow \left(\frac{\nabla_{\boldsymbol{\phi}}\rho_0}{\rho_0}\right)_j = \frac{1}{\rho_0^{(1)}(\phi^j, \phi'^j, \tau)} \frac{\partial \rho_0^{(1)}}{\partial \phi_j}(\phi^j, \phi'^j, \tau)$$

where $\rho_0^{(1)}$ is the single rotor free propagator. Using properties of Jacobi-Theta functions, it can be shown that,[93]

$$\left(\frac{\nabla_{\boldsymbol{\phi}}\rho_0}{\rho_0}\right)_j = \sum_{n=1}^{\infty}(-1)^n \mathrm{csch}(\tau n)\sin(n(\phi^j - \phi'^j)) \tag{2.80}$$

Since we want an asymptotic expansion in τ, we can use the series expansion of $\mathrm{csch}(n\tau)$ and retain the first non-trivial term to get:

$$\left(\frac{\nabla_{\boldsymbol{\phi}}\rho_0}{\rho_0}\right)_j \approx \frac{1}{\tau}\sum_{n=1}^{\infty}(-1)^n \frac{\sin(n(\phi^j - \phi'^j))}{n} \tag{2.81}$$

The above equation is just the Fourier series of the saw-tooth function divided by τ which, when restricted to $[-\pi, \pi)$ becomes:

$$\left(\frac{\nabla_{\boldsymbol{\phi}}\rho_0}{\rho_0}\right)_j \approx -\frac{1}{2\tau}(\phi^j - \phi'^j) \tag{2.82}$$

2.5.3 Second Term Of The Wigner-Kirkwood Expansion

As discussed in the main text, Eq. (2.76), can be solved recursively using the Perelomov relation,

$$P_n(\boldsymbol{\phi}, \boldsymbol{\phi}') = n\int_0^1 dt\ t^{n-1}V(\boldsymbol{\theta}(t))P_{n-1}(\boldsymbol{\theta}(t), \boldsymbol{\phi}') - n\int_0^1 dt\ t^{n-1}\Delta_{\boldsymbol{\theta}}P_{n-1}(\boldsymbol{\theta}(t), \boldsymbol{\phi}') \tag{2.83}$$

where P_n is the nth term in the series expansion of F in powers of τ ($F = \sum_n \frac{(-\tau)^n}{n!}P_n(\boldsymbol{\phi}, \boldsymbol{\phi}')$). Using Perelomov's recursion relation for $n = 1$ and $n = 2$ gives,

$$P_1(\boldsymbol{\phi}, \boldsymbol{\phi}') = \sum_{i=1}^{N-1}\int_0^1 V_{i,i+1}(\boldsymbol{\theta}(t))\ dt = \sum_{i=1}^{N-1} W_{i,i+1}(\boldsymbol{\phi}, \boldsymbol{\phi}') \tag{2.84}$$

$$P_2(\boldsymbol{\phi}, \boldsymbol{\phi}') = 2\sum_{i,j=1}^{N-1}\int_0^1 dt\ t\ V_{i,i+1}W_{j,j+1} - 2\sum_{i=1}^{N-1}\int_0^1 dt\ t\left(\frac{\partial^2 W_{i,i+1}}{\partial\theta_i^2} + \frac{\partial^2 W_{i,i+1}}{\partial\theta_{i+1}^2}\right) \tag{2.85}$$

where, $V_{i,i+1} = V_{i,i+1}(\boldsymbol{\theta}(t))$, $W_{j,j+1} = W_{j,j+1}(\boldsymbol{\theta}(t), \boldsymbol{\phi}')$ in the above equation. We can simplify the above expression for P_2. To see this, define I_{ij} to be a single term in the first summation of Eq. (2.85),

$$I_{ij} = \int_0^1 dt\ t\ V_{i,i+1}(\boldsymbol{\theta}(t))W_{j,j+1}(\boldsymbol{\theta}(t), \boldsymbol{\phi}') \tag{2.86}$$

Using the definition of $W_{j,j+1}(\boldsymbol{\theta}(t), \boldsymbol{\phi}')$ where $\boldsymbol{\theta}(t)$ represents a point on the line between $\boldsymbol{\phi}$ and $\boldsymbol{\phi}'$, we get,

$$W_{j,j+1}(\boldsymbol{\theta}(t), \boldsymbol{\phi}') = \frac{1}{t}\int_0^t V_{j,j+1}(\boldsymbol{\theta}(t'))dt' \tag{2.87}$$

Using Eq. (2.87) and integrating Eq. (2.86) by parts yields:

$$I_{ij} + I_{ji} = W_{i,i+1}W_{j,j+1}, \quad I_{jj} = \frac{W_{j,j+1}^2}{2} \tag{2.88}$$

$$\Rightarrow 2\sum_{i,j=1}^{N-1} I_{ij} = 2\sum_{i<j}^{N-1}(I_{ij} + I_{ji}) + 2\sum_{j=1}^{N-1} I_{jj} = \sum_{j=1}^{N-1} W_{j,j+1}^2 + 2\sum_{i<j}^{N-1} W_{i,i+1}W_{j,j+1} \tag{2.89}$$

This gives the equation for P_2 provided in the main text,

$$P_2(\boldsymbol{\phi}, \boldsymbol{\phi}') = \sum_{j=1}^{N-1} W_{j,j+1}^2 + 2\sum_{i<j}^{N-1} W_{i,i+1}W_{j,j+1} - 2\sum_{i=1}^{N-1}\int_0^1 dt\; t\left(\frac{\partial^2 W_{i,i+1}}{\partial\theta_i^2} + \frac{\partial^2 W_{i,i+1}}{\partial\theta_{i+1}^2}\right) \tag{2.90}$$

2.5.4 Pair Density Error

The diagonal terms ($\boldsymbol{\phi} = \boldsymbol{\phi}'$) of the Wigner-Kirkwood expansion are:[69]

$$P_1 = V \tag{2.91}$$

$$P_2 = V^2 - \frac{1}{3}\Delta V \tag{2.92}$$

$$P_3 = V^3 - V\Delta_{\boldsymbol{\phi}}V - \frac{1}{2}(\nabla_{\boldsymbol{\phi}}V)^2 + \frac{1}{10}\Delta_{\boldsymbol{\phi}}^2 V \tag{2.93}$$

We can express V^3 from P_3 as follows:

$$\begin{aligned} V^3 = &\sum_n V_{n,n+1}^3 + 6\sum_{n<m<l} V_{n,n+1}V_{m,m+1}V_{l,l+1} \\ &+3\sum_{n<m}(V_{n,n+1}^2 V_{m,m+1} + V_{m_m+1}^2 V_{n,n+1}) \end{aligned} \tag{2.94}$$

$V\Delta_{\boldsymbol{\phi}}V$ can be expressed as:

$$V\Delta_{\boldsymbol{\phi}}V = \sum_n V_{n,n+1}(\Delta V)_{n,n+1} + \sum_{n<m}(V_{n,n+1}(\Delta V)_{m,m+1} + V_{m,m+1}(\Delta V)_{n,n+1}) \tag{2.95}$$

where we have used the notation:

$$(\Delta V)_{m,m+1} = \frac{\partial^2 V_{m,m+1}}{\partial \phi_m^2} + \frac{\partial^2 V_{m,m+1}}{\partial \phi_{m+1}^2} \tag{2.96}$$

Moreover, the bi-laplacian term $\Delta_{\boldsymbol{\phi}}^2 V$ is given by:

$$\Delta_{\boldsymbol{\phi}}^2 V = \sum_m (\Delta^2 V)_{m,m+1} \tag{2.97}$$

$$(\Delta^2 V)_{m,m+1} = \frac{\partial^2 (\Delta V)_{m,m+1}}{\partial \phi_m^2} + \frac{\partial^2 (\Delta V)_{m,m+1}}{\partial \phi_{m+1}^2} \tag{2.98}$$

To compare $P_3(\boldsymbol{\phi}, \boldsymbol{\phi})$ and $Q_3(\boldsymbol{\phi}, \boldsymbol{\phi})$, first note that:

$$Q_3 = \sum_{n=1} P_{3,n}^{(2)} + 6 \sum_{n<m<l} P_{1,n}^{(2)} P_{1,m}^{(2)} P_{1,l}^{(2)} + \; 3 \sum_{n<m}^{N-1} (P_{2,n}^{(2)} P_{1,m}^{(2)} + P_{1,n}^{(2)} P_{2,m}^{(2)}) \tag{2.99}$$

The first term in Eq. (2.99) can be expressed as,

$$\begin{aligned} \sum_n P_{3,n}^{(2)} = \sum_n (V_{n,n+1}^3 - V_{n,n+1} (\Delta V)_{n,n+1}) + \frac{1}{10} \sum_n (\Delta^2 V)_{n,n+1} \\ - \frac{1}{2} \sum_n \left((\nabla V_{n,n+1})_n^2 + (\nabla V_{n,n+1})_{n+1}^2 \right) \end{aligned} \tag{2.100}$$

where $(\nabla V_{n,n+1})_n^2 = (\partial_n V_{n,n+1})^2$ (∂_n here represents the derivative with respect to ϕ_n). The second term in Eq. (2.99) can be written as,

$$6 \sum_{n<m<l} P_{1,n}^{(2)} P_{1,m}^{(2)} P_{1,l}^{(2)} = 6 \sum_{n<m<l} V_{n,n+1} V_{m,m+1} V_{l,l+1} \tag{2.101}$$

The final term in Eq. (2.99) can be written as,

$$\begin{aligned} 3 \sum_{n<m} (P_{2,n}^{(2)} P_{1,m}^{(2)} + P_{1,n}^{(2)} P_{2,m}^{(2)}) = 3 \sum_{n<m} (V_{n,n+1}^2 V_{m,m+1} + V_{m_m+1}^2 V_{n,n+1}) \\ - \sum_{n<m} (V_{n,n+1} (\Delta V)_{m,m+1} + V_{m,m+1} (\Delta V)_{n,n+1}) \end{aligned} \tag{2.102}$$

Using these, we find that P_3 and Q_3 agree for all terms in equation (2.93) except for $-(\nabla_{\boldsymbol{\phi}} V)^2/2$. The exact difference between P_3 and Q_3 is:

$$P_3 - Q_3 = -\sum_{n=2}^{N-1} (\nabla V_{n-1,n})_n (\nabla V_{n,n+1})_n \neq 0 \tag{2.103}$$

where we have used:

$$(\nabla_{\boldsymbol{\phi}} V)^2 = \sum_{n=1}^{N-1} \left((\nabla V_{n,n+1})_n^2 + (\nabla V_{n,n+1})_{n+1}^2 \right) + 2 \sum_{n=2}^{N-1} (\nabla V_{n-1,n})_n (\nabla V_{n,n+1})_n \tag{2.104}$$

Eq. (2.103) is the error term provided in the main text.

Chapter 3

Qubit Encodings For Planar Rotor Lattices

3.1 Introduction

While Quantum Monte Carlo (QMC) and Density Matrix Renormalization Group (DMRG) techniques are currently state-of-the-art for investigating the many-body physics of lattice systems, they are not without deficiencies. For instance, path integral techniques are famously inefficient in the presence of a sign problem and DMRG is difficult to extend to higher lattice dimensions.[14,97,101] These constraints necessitate the development of tools that can extend our investigative capabilities to such difficult-to-probe regimes. One such potential avenue for improvements is offered by relatively recent advances in the development of quantum algorithms and devices.[47,102,103]

In recent years, numerous qubit mappings have been developed and optimized for typical quantum chemistry problems, for instance, the Jordan-Wigner mapping and the generalized superfast encoding, with the goal of simulating such systems using Quantum Phase Estimation (QPE) as well as hybrid approaches such as Variational Quantum Eigensolver (VQE).[104–107] Since electronic structure problems typically involve fermionic degrees of freedom, these mappings target second quantized Hamiltonians. For bosonic systems, because the occupation number is not bounded by an exclusion principle, encoding schemes require a truncation after which the unary mapping embeds the system into a qubit lattice

Hilbert space.[108,109] In this chapter, we develop two qubit encoding schemes for the first quantized planar rotor lattice Hamiltonian.

The first approach relies on representing the discrete momentum basis in binary.[110] Then, the projectors used to express the Hamiltonian can be mapped to spin-1/2 projection operators. The number of qubits required to encode the rotor lattice Hamiltonian grows linearly in system size and logarithmically in the single rotor basis set size. The second mapping is constructed by embedding the truncated rotor Hilbert space in a larger qubit Hilbert space as done for bosonic systems.[109] Then, the resulting spin-1/2 lattice is projected to recover the subspace corresponding to the physical space. The number of qubits required by this second encoding scales linearly in the number of rotors as well as the single rotor basis set size.

This chapter is organized as follows: Sec. 3.2 discusses the dipolar planar rotor lattice and the two qubit encodings. Here, we also discuss quantum phase estimation, a polynomially scaling algorithm that can be used to compute ground state energies and prepare the exact ground state for further computations on a quantum device. In Sec. 3.3, we discuss our computational results. We first calculate the ground state energy for small coplanar chains in the qubit representations using sparse diagonalization, to assess the veracity of our approaches. Then, we perform state vector QPE calculations with the binary mapping and discuss the register requirements for simulating this system using a quantum device. Finally, in Sec. 3.4, we conclude and discuss future research directions in the context of these qubit encodings.

3.2 Theoretical Framework

3.2.1 Planar Rotor Lattice

In this work, we consider a d-dimensional lattice ($d \in \{1, 2, 3\}$) of planar rotors with a dipole-dipole interaction. The system is defined by the Hamiltonian,

$$H = B \sum_{i=1}^{N} l_i^2 + \sum_{i<j}^{N_b} V_{i,j} \tag{3.1}$$

where l_i is the angular momentum of a single rotor and V_{ij} is the dipole interaction between sites i and j. N_b here denotes the number of bonds in the rotor lattice. In a general system,

this is the number of pairs of rotors: $N_b = \binom{N}{2}$. The pair-wise dipole-dipole interaction is given by,[37]

$$V_{ij} = \frac{g_0}{R_{ij}^3}(\boldsymbol{r}_i \cdot \boldsymbol{r}_j - 3(\boldsymbol{r}_i \cdot \boldsymbol{R}_{ij})(\boldsymbol{r}_j \cdot \boldsymbol{R}_{ij})) \tag{3.2}$$

Here, $g_0 = 1/4\pi\epsilon_0$ is a site-independent constant, R_{ij} is the distance between sites i and j, $\boldsymbol{r}_i$ is the dipole moment corresponding to site i and $\boldsymbol{R}_{ij}$ is the vector connecting sites i and j. Expressing the dipole moment for each site in components ($\boldsymbol{r}_i = (x_i, y_i)$), we get the following interaction for a general 3-dimensional lattice,

$$\begin{aligned} V_{ij} = \frac{g_0}{R_{ij}^3}[&(1 - 3\cos^2(\gamma_{ij}^1)\sin^2(\gamma_{ij}^2))x_i x_j + (1 - 3\sin^2(\gamma_{ij}^1)\sin^2(\gamma_{ij}^2))y_i y_j \\ &-3\cos(\gamma_{ij}^1)\sin(\gamma_{ij}^1)\sin^2(\gamma_{ij}^2)(x_i y_j + x_j y_i)] \end{aligned} \tag{3.3}$$

Here, γ_{ij}^1 is the polar angle and the γ_{ij}^2 is the azimuthal angle associated with the vector $\boldsymbol{R}_{ij}$. For a coplanar chain of rotors with a pairwise nearest neighbor interaction, we get,

$$V = \sum_{i=1}^{N-1}(x_i x_j - 2y_i y_j) \tag{3.4}$$

Since each dipole moment is a unit vector, we can parameterize it by a polar angular coordinate ϕ to get $x_i = \cos(\phi_i)$ and $y_i = \sin(\phi_i)$. In the momentum representation, the diagonal angular momentum operator admits a discrete basis due to periodic boundaries in position space,

$$l_i = \sum_{m_i=-\infty}^{\infty} m_i|m_i\rangle\langle m_i| \approx \sum_{m_i=-l}^{n} m_i|m_i\rangle\langle m_i| \tag{3.5}$$

Because we are interested in studying the ground state properties of such systems computationally, we have introduced a basis set cut-off, $-l \leq m \leq n$, in the momentum representation as the higher energy single rotor states do not contribute appreciably to the many-body ground state.[43] In particular, for 1d chains, it has been shown that using $m \in [-4, 4]$ is sufficient for convergence via DMRG studies in previous work.[19] To construct the interaction term we use the momentum representation of the position operators which can be expressed as linear combinations of the increment and decrement operators

(S_j^+ and S_j^-),[47,111]

$$x_j = \frac{1}{2}(S_j^+ + S_j^-) = \frac{1}{2}\sum_{m_j=-l}^{n} |m_j+1\rangle\langle m_j| + h.c. \tag{3.6}$$

$$y_j = \frac{1}{2i}(S_j^+ - S_j^-) = \frac{1}{2i}\sum_{m_j=-l}^{n} |m_j+1\rangle\langle m_j| + h.c. \tag{3.7}$$

Here, the state $|n+1\rangle$ is identified with $|-l\rangle$ and $|-l-1\rangle$ is identified with $|n\rangle$ so that the momentum states obey periodic boundary conditions (as they do in the DVR representation discussed in chapter 1). This is equivalent to constructing a Fourier series for band-limited functions and has the effect of imposing a discretization in position space. The interaction operators x_ix_j, y_iy_j and $(x_iy_j + x_jy_i)$ are then given by,

$$x_ix_j = \frac{1}{4}\sum_{m_i,m_j} |m_i+1, m_j-1\rangle\langle m_i, m_j| + |m_i+1, m_j+1\rangle\langle m_i, m_j| + h.c. \tag{3.8}$$

$$y_iy_j = \frac{1}{4}\sum_{m_i,m_j} |m_i+1, m_j-1\rangle\langle m_i, m_j| - |m_i+1, m_j+1\rangle\langle m_i, m_j| + h.c. \tag{3.9}$$

$$(x_iy_j + x_jy_i) = \frac{i}{2}\sum_{m_i,m_j} |m_i-1, m_j-1\rangle\langle m_i, m_j| + h.c. \tag{3.10}$$

It is instructive to specify the momentum representation of the coplanar chain since we use that system for our computational analysis,

$$H = \sum_{i=1}^{N} K_i + \sum_{i=1}^{N-1} V_{i,i+1}, \qquad K_i = \sum_{m_i=0}^{d-1} (m_i - l)^2 |m_i\rangle\langle m_i| \tag{3.11}$$

$$V_{i,i+1} = -\frac{1}{4}\sum_{m_i,m_{i+1}=0}^{d-1} (|m_i+1, m_j-1\rangle\langle m_i, m_j|)$$

$$+\frac{3}{4}\sum_{m_i,m_{i+1}=0}^{d-1} (|m_i+1, m_j-1\rangle\langle m_i, m_j|) + h.c. \tag{3.12}$$

Note that the terms m_i+1 and m_i-1 here correspond to addition and subtraction modulo $d = n+l+1$ (the number of states) because we use periodic boundaries in momentum space. Moreover, we have transformed the sum in K_i such that $m_i \to m_i + l$ for convenience.

3.2.2 Binary Qubit Encoding

Since we have a finite basis set (in the momentum representation), we can construct a qubit mapping by representing each single rotor state $|m\rangle$ for $-l \leq m \leq n$ in binary.[110] For $d = n + l + 1$ states, we need $k = \lceil \log_2(d) \rceil$ qubits.[109] This yields for the single rotor kinetic energy operator,

$$\begin{aligned} l_j^2 &= \sum_{m_j=-l}^{n} m_j^2 |m_j\rangle\langle m_j| = \sum_{m_j=0}^{d-1} (m_j - l)^2 |m_j\rangle\langle m_j| \\ &= \sum_{i_1^j,...,i_k^j} \left(\sum_{r=1}^{k} 2^{k-r} i_r - l \right)^2 |i_1^j, ..., i_k^j\rangle\langle i_1^j, ..., i_k^j| \end{aligned} \tag{3.13}$$

where we have re-expressed the eigenvalues $(m_j - l)^2$ using the binary representation of $m_j \in \{0, ..., d-1\}$,

$$m_j = \sum_{r=1}^{k} 2^{k-r} i_r^j \tag{3.14}$$

To construct the qubit operators, we can expand the square in Eq. (3.13) to get,

$$l_j^2 = \sum_{i_1^j,...,i_k^j} \sum_{r,s=1}^{k} 2^{2k-r-s} i_r^j i_s^j |i_1^j, ..., i_k^j\rangle\langle i_1^j, ..., i_k^j| - 2l \sum_{i_1^j,...,i_k^j} \sum_{r=1}^{k} 2^{k-r} i_r^j |i_1^j, ..., i_k^j\rangle\langle i_1^j, ..., i_k^j| + l^2$$

$$\Rightarrow l_j^2 = 2^{2k} \sum_{r,s} 2^{-r-s} \sum_{i_r^j, i_s^j} i_r^j i_s^j |i_r^j, i_s^j\rangle\langle i_r^j, i_s^j| - 2^{k+1} l \sum_{r} 2^{-r} \sum_{i_r^j} i_r^j |i_r^j\rangle\langle i_s^j| + l^2 \tag{3.15}$$

Since $i_r, i_s \in \{0, 1\}$, and using the fact that $|1\rangle\langle 1| = \frac{1}{2}(I - \sigma_z)$, we get,

$$l_j^2 = 2^{2k} \sum_{r,s} 2^{-r-s} |1_r^j, 1_s^j\rangle\langle 1_r^j, 1_s^j| - 2^{k+1} l \sum_{r} 2^{-r} |1_r^j\rangle\langle 1_r^j| + l^2 \tag{3.16}$$

$$\Rightarrow l_j^2 = 2^{2(k-1)} \sum_{r,s} 2^{-r-s} (I - \sigma_{r,j}^z)(I - \sigma_{s,j}^z) - 2^k l \sum_{r} 2^{-r} (I - \sigma_{r,j}^z) + l^2 \tag{3.17}$$

Expanding out the products yields,

$$l_j^2 = 2^{2(k-1)} \sum_{r,s} 2^{-r-s} \sigma_{r,j}^z \sigma_{s,j}^z - 2^{2k-1} \sum_{s=1}^{k} 2^{-s} \sum_r 2^{-r} \sigma_{r,j}^z$$
$$+2^k l \sum_r 2^{-r} \sigma_{r,j}^z + 2^{2k-2} \left(\sum_{r=1}^{k} 2^{-r} \right)^2 - 2^k l \sum_{r=1}^{k} 2^{-r} + l^2 \tag{3.18}$$

If we restrict d to be a power of 2 and collect terms linear in σ^z, we get,

$$-2^{k-1}(2^{k-1} - 1 - 2l) \sum_{r=1}^{k} 2^{-r} \sigma_{r,j}^z = -\frac{(n+l+1)(n-l)}{2} \sum_{r=1}^{k} 2^{-r} \sigma_{r,j}^z \tag{3.19}$$

where we have used the following,

$$\sum_{r=1}^{k} 2^{-r} = 1 - 2^{-k}, \quad 2^k = n + l + 1 \tag{3.20}$$

For the constant term in Eq. (3.18), we similarly get,

$$\frac{1}{4}(2^k - (2l+1))^2 = \frac{1}{4}(n-l)^2 \tag{3.21}$$

This finally gives the following for the kinetic energy operator,

$$l_j^2 = \left(\frac{n+l+1}{2} \right)^2 \sum_{r,s} 2^{-r-s} \sigma_{r,j}^z \sigma_{s,j}^z - \frac{(n+l+1)(n-l)}{2} \sum_{r=1}^{k} 2^{-r} \sigma_{r,j}^z + \frac{1}{4}(n-l)^2 \tag{3.22}$$

It is instructive to note here that while Eq. (3.22) corresponds to the kinetic energy of a single rotor, it contains 2-body Ising-like interaction terms between the spins used to represent the rotor basis states. These result from the squaring of the angular momentum operator as can be seen by factoring Eq. (3.22),

$$l_j^2 = \left(\frac{n+l+1}{2} \left(\sum_{r=1}^{k} 2^{-r} \sigma_{r,j}^z - \frac{n-l}{n+l+1} \right) \right)^2 \tag{3.23}$$

The fact that the kinetic energy operator is a perfect square shows that the mapping is well-defined because representing l_j in binary and then squaring it should be identical to directly constructing the kinetic energy operator as we have done above.

For the potential energy operators, it is sufficient to construct the binary representation of the single rotor increment and decrement terms (S_j^+ and S_j^-) since the many-body potential is always a linear combination of products of those operators. Representing m_j using k bits, we get $|m_j\rangle = |i_1^j, ..., i_k^j\rangle$. We can then construct the binary representation of $|m_j + 1\rangle$, by flipping all the qubits in the binary representation of $|m_j\rangle$ up to and including the first $|0\rangle$ starting from the right. Therefore, the increment operator is given by,

$$S_j^+ = \sum_{m_j=0}^{d-1} |m_j + 1\rangle\langle m_j| = \sum_{r=1}^{k} \sigma_{r,j}^+ \left(\prod_{s=r+1}^{k} \sigma_{s,j}^- \right) + \left(\prod_{s=1}^{k} \sigma_{s,j}^- \right) \tag{3.24}$$

Here, the operators $\sigma_{r,j}^{\pm}$ are defined as $\frac{1}{2}(\sigma_{r,j}^x \pm i\sigma_{r,j}^y)$. It is instructive to note that for an arbitrary qubit string basis state $|i_1^j, ..., i_k^j\rangle$ with $i_a = 0$ and $i_b = 1$ for all $b > a$, the action of the above sum of Pauli strings is 0 for all terms except for the operator corresponding to $r = a$ because $\sigma_{r,j}^+|1\rangle = \sigma_{r,j}^-|0\rangle = 0$. The term containing no $\sigma_{r,j}^+$ operators is equivalent to $|n + 1\rangle\langle n| = |-l\rangle\langle n| = |0^k\rangle\langle 1^k|$ in Eqs. (3.6) and (3.7). The decrement operator can similarly be constructed as follows,

$$S_j^- = \sum_{m_j=0}^{d-1} |m_j - 1\rangle\langle m_j| = \sum_{r=1}^{k} \sigma_{r,j}^- \left(\prod_{s=r+1}^{k} \sigma_{s,j}^+ \right) + \left(\prod_{s=1}^{k} \sigma_{s,j}^+ \right) \tag{3.25}$$

The operator x_j then takes the form,

$$x_j = \frac{1}{2} \sum_{r=1}^{k} \left(\sigma_{r,j}^+ \prod_{s=r+1}^{k} \sigma_{s,j}^- + \sigma_{r,j}^- \prod_{s=r+1}^{k} \sigma_{s,j}^+ \right) + \frac{1}{2} \prod_{s=1}^{k} \sigma_{s,j}^- + \frac{1}{2} \prod_{s=1}^{k} \sigma_{s,j}^+ \tag{3.26}$$

For each $1 \leq r \leq k$, we can construct the corresponding Pauli string using the definitions of $\sigma_r^{\pm}$. For each such term $(x_j)_r$ in the sum, we get,

$$\begin{aligned}(x_j)_r = &\frac{1}{2^{k-r+1}} \sigma_{r,j}^x \sum_{\gamma \in \{x,y\}^{k-r}} (-i)^{n_y} \prod_{s=r+1}^{k} \sigma_{s,j}^{\gamma(s)} + \frac{i}{2^{k-r+1}} \sigma_{r,j}^y \sum_{\gamma \in \{x,y\}^{k-r}} (-i)^{n_y} \prod_{s=r+1}^{k} \sigma_{s,j}^{\gamma(s)} \\ &+ \frac{1}{2^{k-r+1}} \sigma_{r,j}^x \sum_{\gamma \in \{x,y\}^{k-r}} i^{n_y} \prod_{s=r+1}^{k} \sigma_{s,j}^{\gamma(s)} - \frac{i}{2^{k-r+1}} \sigma_{r,j}^y \sum_{\gamma \in \{x,y\}^{k-r}} i^{n_y} \prod_{s=r+1}^{k} \sigma_{s,j}^{\gamma(s)}\end{aligned} \tag{3.27}$$

Here, we sum over all 2^{k-r} possible vectors $\gamma = (\gamma(r+1), ..., \gamma(k))$ with $\gamma(s) \in \{x, y\}$ for each term. n_y is the number of indices $s \in \{r + 1, s\}$ such that $\gamma(s) = y$. Adding the first

and third terms in the above equation yields a cancellation of all terms corresponding to an odd n_y. Similarly, adding the second and the last terms results in a cancellation of all terms associated with an even n_y. This gives,

$$x_j = \sum_{r=1}^{k} \frac{1}{2^{k-r}} \left(\sum_{\gamma \text{ even}} (-1)^{n_y/2} \sigma_{r,j}^{x} \prod_{s=r+1}^{k} \sigma_{r,j}^{\gamma(s)} + \sum_{\gamma \text{ odd}} (-1)^{(n_y-1)/2} \sigma_{r,j}^{y} \prod_{s=r+1}^{k} \sigma_{s,j}^{\gamma(s)} \right) + \frac{1}{2^k} \sum_{\gamma \text{ even}} (-1)^{n_y/2} \prod_{s=1}^{k} \sigma_{s,k}^{\gamma(s)} \tag{3.28}$$

where the last term comes from the operator strings corresponding to the cyclic terms: $|-l\rangle\langle n|$ and $|n\rangle\langle -l|$ in the definition of the increment and decrement operators. In the above equation γ even denotes index strings with an even number of elements equaling y and vice versa for γ odd. For y_j, we similarly get,

$$y_j = \sum_{r=1}^{k} \frac{1}{2^{k-r}} \left(\sum_{\gamma \text{ odd}} (-1)^{(n_y+1)/2} \sigma_{r,j}^{x} \prod_{s=r+1}^{k} \sigma_{r,j}^{\gamma(s)} + \sum_{\gamma \text{ even}} (-1)^{n_y/2} \sigma_{r,j}^{y} \prod_{s=r+1}^{k} \sigma_{s,j}^{\gamma(s)} \right) + \frac{1}{2^k} \sum_{\gamma \text{ odd}} (-1)^{(n_y+1)/2} \prod_{s=1}^{k} \sigma_{s,k}^{\gamma(s)} \tag{3.29}$$

The matrix elements of x_j are all real and the matrix elements of y_j are all imaginary as expected from their respective definitions in the momentum representation. We can now construct the required potential operators as specified in Eqs. (3.8), (3.9) and (3.10) to simulate any lattice of planar rotors. Since the potential is two-body, and because the largest Pauli weight for a single rotor position operator is k, the largest Pauli string we will have for a k bit representation is $2k$ for any planar rotor lattice in this encoding.

3.2.3 Unary Qubit Encoding

The binary encoding discussed in section 3.2.2 maps the on-site kinetic energy operator to a quadratic Hamiltonian. Therefore, the single rotor kinetic energy operator in that representation has spin-spin interaction terms. Moreover, the weight of the Pauli strings in the dipole-dipole interaction increases linearly with $k = \log_2(n + l + 1)$. In this section, we construct another encoding (often referred to as the one-hot or unary encoding) that

yields a constant interaction Pauli weight and results in a kinetic energy term linear in spin operators. However, the cost associated with this simplicity is a larger qubit Hilbert space; this encoding requires $d = n + l + 1$ qubits to represent each rotor. These extra degrees of freedom later need to be projected out to recover the many-body rotor Hilbert space from the embedding. To construct this mapping, first note that the angular momentum operator for this Hamiltonian can be identified with the shifted bosonic number operator (truncated appropriately),

$$l_j = \sum_{m_j=0}^{d} (m_j - l)|m_j\rangle\langle m_j| = (n_j - l) \tag{3.30}$$

$$n_j|k\rangle = k|k\rangle \tag{3.31}$$

Therefore, we can use the typical qubit encoding for bosonic modes to map this system to a lattice of spin-1/2 particles as well. To this end, we identify the single rotor momentum basis states $|m\rangle$ for $1 \leq m \leq d$ with a d-qubit product state,

$$|m\rangle \to |i_0, ..., i_{d-1}\rangle, \quad i_k = \delta_{m,k} \tag{3.32}$$

where the mth qubit is in state $|1\rangle$ and the remaining $d-1$ qubits are in state $|0\rangle$. This state encoding is exhibited in Fig. 3.1. Using this identification, the projection operators $|m_j\rangle\langle m_j|$ needed for the truncated bosonic number operator become,

$$|m_j\rangle\langle m_j| = |0, ..., 1, ..., 0\rangle\langle 0, ..., 1, ..., 0| = \frac{1}{2^d}(I + \sigma^z_{0,j})...(I - \sigma^z_{m_j,j})...(I + \sigma^z_{d-1,j}) \tag{3.33}$$

The kinetic energy operator in this representation can then be expressed as,

$$l_j^2 = \sum_{m_j=0}^{d-1} \frac{(m_j - l)^2}{2^d}(I - \sigma^z_{m_j,j}) \prod_{k \neq m_j}^{d-1} (I + \sigma^z_{k,j}) \tag{3.34}$$

Note that the qubit Hilbert space we have mapped to here is $\mathcal{H}_Q = (\mathbb{C}^2)^{\otimes d}$ with dimension 2^d while our single rotor system Hilbert space $\mathcal{H}_S$ has dimension d. This discrepancy arises because only a small number of vectors in $\mathcal{H}_Q$ are relevant physical states for our rotor system. The extra degrees of freedom correspond to the set $V \subset \mathcal{H}_Q$ defined by the span of all product states with more than one qubit in state $|1\rangle$ and the vacuum state $|0, ..., 0\rangle$,

$$V = \text{Span}\left\{|i_0^j, ..., i_{d-1}^j\rangle \mid i_0^j + i_1^j + ... + i_{d-1}^j \neq 1\right\} \tag{3.35}$$

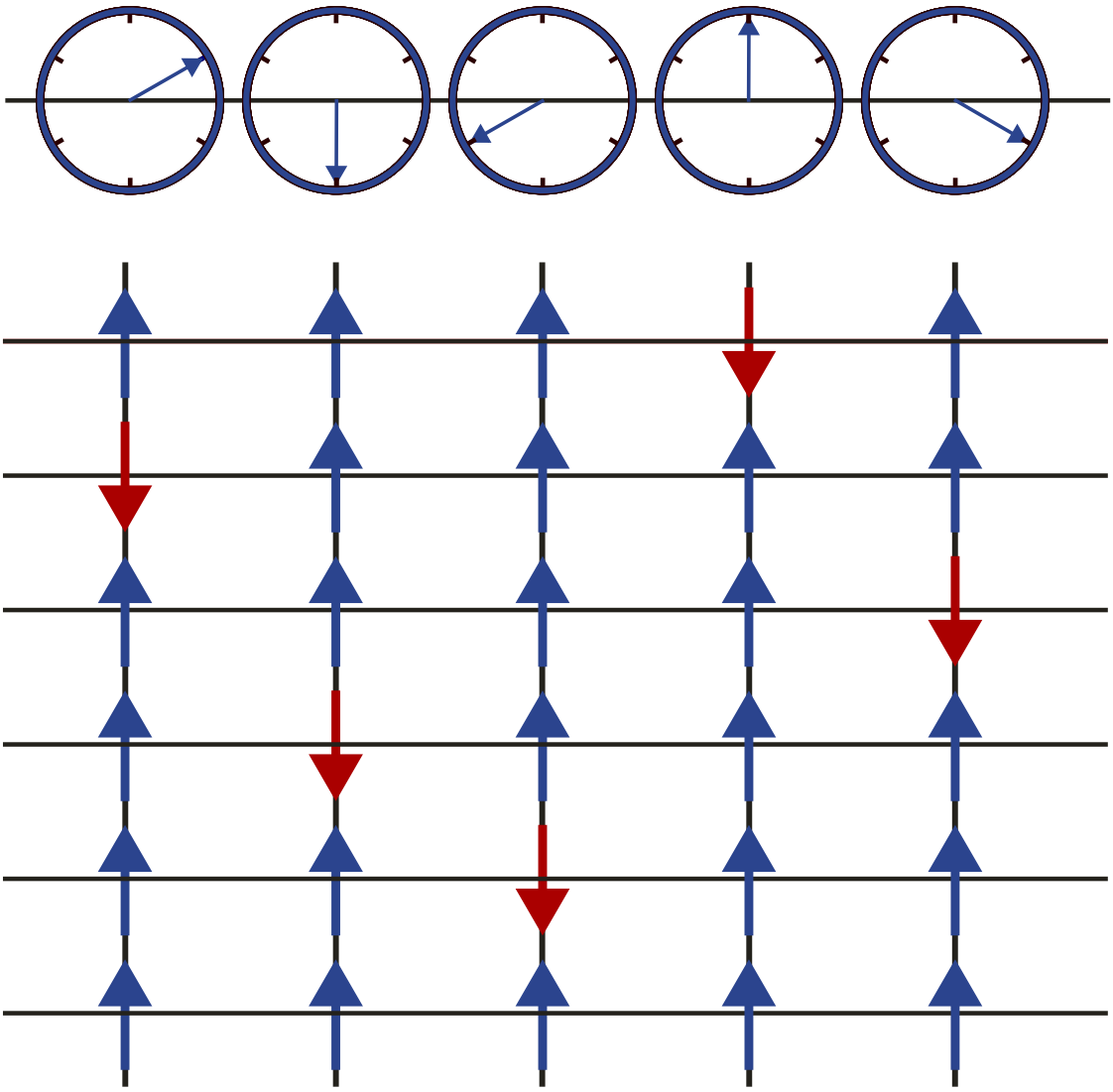


Figure 3.1: Schematic representation of a chain of planar rotors encoded into a lattice of spins using the unary mapping approach. Each of the ticks on the clocks represent different momentum eigenstates. The spin-down states correspond to the state $|1\rangle$ and the spin-up states correspond to the state $|0\rangle$ in the qubit encoding. A single rotor momentum eigenstate is mapped to a constrained chain of spins with exactly one excited spin site.

To recover $\mathcal{H}_S$, we can quotient the qubit Hilbert space $\mathcal{H}_Q$ by V and since $\mathcal{H}_Q = \mathcal{H}_S \oplus V$, the quotient $\mathcal{H}_Q/V$ is isomorphic to $\mathcal{H}_S$, which can be concretely represented as follows,[112]

$$\mathcal{H}_S = \text{Span}\left\{|i_0^j, ..., i_{d-1}^j\rangle \mid i_0^j + ... + i_{d-1}^j = 1\right\} \tag{3.36}$$

While we could work with $\mathcal{H}_Q$, projecting down to $\mathcal{H}_S$, yields a tremendous simplification of the qubit Hamiltonian. To see this, first note that for any state $|\psi\rangle \in \mathcal{H}_S$, the action of l_j^2 as defined in Eq. (3.34) is given by,

$$l_j^2|\psi\rangle = \sum_{m_j=0}^{d-1} (m_j - l)^2 \frac{(I - \sigma_{m_j,j}^z)}{2}|\psi\rangle \tag{3.37}$$

where we have expressed $|\psi\rangle$ as an arbitrary linear combination of product states in $\mathcal{H}_S$ and used the fact that for a product state $|\psi_r\rangle \in \mathcal{H}_S$,

$$\left(\frac{I - \sigma_{m_j,j}^z}{2}\right) \prod_{k \neq m_j}^{d-1} \left(\frac{I + \sigma_{k,j}^z}{2}\right) |\psi_r\rangle = \left(\frac{I - \sigma_{m_j,j}^z}{2}\right) |\psi_r\rangle \tag{3.38}$$

for all $0 \leq m_j, r \leq d-1$. Note that for $|\psi\rangle \in V$, such that $|\psi\rangle = |i_0^j, ..., i_{d-1}^j\rangle$ with $i_{m_j}^j \neq 0$, the above equality does not hold,

$$\left(\frac{I - \sigma_{m_j,j}^z}{2}\right) \prod_{k \neq m_j}^{d-1} \left(\frac{I + \sigma_{k,j}^z}{2}\right) |\psi\rangle = 0 \tag{3.39}$$

$$\left(\frac{I - \sigma_{m_j,j}^z}{2}\right) |\psi\rangle = |\psi\rangle \neq 0 \tag{3.40}$$

Therefore, only if we restrict to $\mathcal{H}_S$ can we neglect terms corresponding to $|0_k\rangle\langle 0_k|$ in our Hamiltonian. Using this projection, our kinetic energy is linear in Pauli operators,

$$l_j^2 = -\frac{1}{2} \sum_{m_j=0}^{d-1} (m_j - l)^2 \sigma_{m_j,j}^z + \frac{n(n+1)(2n+1) + l(l+1)(2l+1)}{12} \tag{3.41}$$

where we have used Faulhaber's formula to compute the constant energy offset.[113] For $n = l + 1$, we get,

$$l_j^2 = -\frac{1}{2} \sum_{m_j=0}^{d-1} (m_j - l)^2 \sigma_{m_j,j}^z + \frac{(2n^2+1)n}{6} \tag{3.42}$$

For the potential operators, we again need to encode the increment and decrement operators. To this end, consider the projection operators $|m_j+1\rangle\langle m_j|$ in this representation,

$$|m_j+1\rangle\langle m_j| = \sigma^+_{m_j+1,j}\sigma^-_{m_j,j}\prod_{k\neq m_j,m_{j+1}}^{d-1}\left(\frac{I+\sigma^z_{k,j}}{2}\right) = \sigma^+_{m_j+1,j}\sigma^-_{m_j,j}\prod_{k\neq m_j,m_{j+1}}^{d-1}\sigma^-_{k,j}\sigma^+_{k,j} \quad (3.43)$$

Restricting to $\mathcal{H}_S$, we get,

$$|m_j+1\rangle\langle m_j| = \sigma^+_{m_j+1,j}\sigma^-_{m_j,j} \quad (3.44)$$

$$\Rightarrow S^+ = \sum_{m_j=0}^{d}\sigma^+_{m_j+1,j}\sigma^-_{m_j,j}, \quad S^- = \sum_{m_j=0}^{d}\sigma^+_{m_j,j}\sigma^-_{m_j+1,j} \quad (3.45)$$

where the index $m_j = d+1$ is identified with $m_j = 0$ and the sum contains $d+1$ terms to account for the periodicity of the momentum states. Finally, we can express the interaction operators x_ix_j, y_iy_j and $(x_iy_j + x_jy_i)$ using this encoding,

$$x_ix_j = \frac{1}{4}\sum_{m_i,m_j=0}^{d}\sigma^+_{m_i+1,i}\sigma^-_{m_i,i}\sigma^+_{m_j+1,j}\sigma^-_{m_j,j} + \sigma^+_{m_i+1,i}\sigma^-_{m_i,i}\sigma^+_{m_j,j}\sigma^-_{m_j+1,j} + h.c. \quad (3.46)$$

$$y_iy_j = \frac{1}{4}\sum_{m_i,m_j=0}^{d}\sigma^+_{m_i+1,i}\sigma^-_{m_i,i}\sigma^+_{m_j,j}\sigma^-_{m_j+1,j} - \sigma^+_{m_i+1,i}\sigma^-_{m_i,i}\sigma^+_{m_j+1,j}\sigma^-_{m_j,j} + h.c. \quad (3.47)$$

$$(x_iy_j + x_jy_i) = \frac{i}{2}\sum_{m_i,m_j=0}^{d}\sigma^+_{m_i,i}\sigma^-_{m_i+1,i}\sigma^+_{m_j,j}\sigma^-_{m_j+1,j} + h.c. \quad (3.48)$$

Unlike the binary encoding, this mapping results in constant interaction operator Pauli weights and the kinetic energy operator maps to a linear combination of on-site spin operators (no interaction terms). As discussed above, this is a consequence of using a larger number of encoding qubits and then projecting down to the subspace corresponding to the physical states of the rotor lattice. It is also instructive to note here that this encoding relies on initializing the system in the subspace $\mathcal{H}_S$. Then, evolving the state unitarily (such as in quantum phase estimation) would necessarily restrict our system to the physical subspace.

3.2.4 Quantum Phase Estimation

QPE is a polynomial scaling quantum algorithm that can be used for extracting the phase φ associated with the eigenvalue $e^{i2\pi\varphi}$ of a unitary operator U, given an eigenstate of U.[47,114] If the unitary in question is the time-evolution operator e^{iHt}, this can be used to estimate the energy of a given eigenstate.[115] Fig. 3.2 shows the circuit diagram for the algorithm. First, each of the r qubits in the ancilla are Hadamard transformed. Then, a multiplicity-controlled U (with $t = 2\pi$) is applied to the full state followed by an inverse Fourier transform. Finally, the ancilla encoding the r-bit binary representation of the phase $\bar{\varphi}$ associated with the input state $|\varphi\rangle$ is measured. The size of the ancilla r is picked based on the desired accuracy of the phase φ.

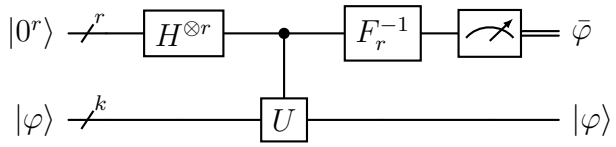


Figure 3.2: Circuit diagram for the quantum phase estimation algorithm applied to an eigenstate of U. The controlled-U operation depicts a multiplicity-controlled-U in this context and F_r^{-1} is the r-qubit inverse quantum Fourier transform. $\bar{\varphi}$ is the r-bit approximation of the phase φ.

Note that to compute the full spectrum of a bounded Hamiltonian H using QPE, we must shift and scale the spectral radius so that all the eigenvalues $\tilde{E}_i$ of the resulting Hamiltonian $\tilde{H}$ can be uniquely mapped to a phase $\varphi \in [0, 1)$.[114] This can be achieved by using the Hamiltonian,

$$\tilde{H} = \frac{1}{E^c_{max} - E^c_{min}}(H - E^c_{min}) \tag{3.49}$$

where E^c_{max} and E^c_{min} are the maximum and minimum classical energy bounds for the system. For a coplanar chain, the maximum classical energy is $E^c_{max} = Nn^2 + 2(N-1)g$, and the minimum classical energy is, $E^c_{min} = -2(N-1)g$. The multiplicity-controlled U requires the application of U^s for $0 \leq s \leq r$ to the state $|\varphi\rangle$. To implement these gates, we need to use an appropriate factorization technique[54,57] for the real time propagator. In our computations, we use the 4th order Trotter approximation with both encodings.

For an arbitrary state $|\psi\rangle$ such that $\langle\psi|E_0\rangle \neq 0$, we can also use QPE to prepare the exact ground state via repeated applications of the same circuit. The number of iterations of QPE

required to project out the exact ground state is polynomial in the overlap between the trial state and the ground state.[115] Consequently, QPE can also be used with an approximate ground state to estimate exact ground state properties. Numerous techniques have been proposed in the literature for preparing the QPE trial state for many-body problems such as DMRG and VQE, a hybrid quantum-classical approach that variationally determines the ground state using a classical device to solve the optimization problem, and a quantum device for measuring expectation values.[114,116]

If we are interested in ground state properties only and have an approximate ground state, we do not need to rescale or shift the Hamiltonian. For a state such that the overlap with the exact ground state is much larger than any of the excited states, repeated applications of QPE will result in a histogram of measured energies. The largest peak in that histogram will correspond to the ground state. Then, another polynomially large (as a function of the height of the corresponding peak) set of QPE simulations would be needed to prepare the state corresponding to the largest peak. Following that, measuring the expectation value of the Hamiltonian will yield the ground state energy. However, shifting the ground state energy (if it is known) so that it can be represented exactly using a small number of ancillary qubits available is still useful for optimizing phase estimation simulations and minimizing precision errors. If we do not possess a sufficiently good approximation of the ground state or knowledge of the exact ground state energy, we need to scale and shift the spectrum as shown in Eq. (3.49) and extract the minimum energy from the histogram constructed by repeated application of QPE to calculate the ground state energy.

3.3 Computational Results & Discussion

3.3.1 Sparse Diagonalization

To assess the validity of the qubit encodings discussed in Sec. 3.2.2 and Sec. 3.2.3, we compute the ground state energy using Lanczos diagonalization for a coplanar chain with $N = 2$ and $N = 3$.[117,118] Figs. 3.3 and 3.4 show the results for both mappings for $g \in [0.1, 1.0]$. Exact Diagonalization (ED) results calculated using the rotor momentum representation given in Eq. (3.11) are also plotted for comparison. For the binary mapping, both simulations used $n = 4$ and $l = 3$. For the unary mapping, we used $n = 4$ and $l = 3$

for $N = 2$ and $n = 3$ with $l = 2$ for $N = 3$. In all of these cases, the mapped Hamiltonians yield the same ground state energy as ED with the rotor representation.

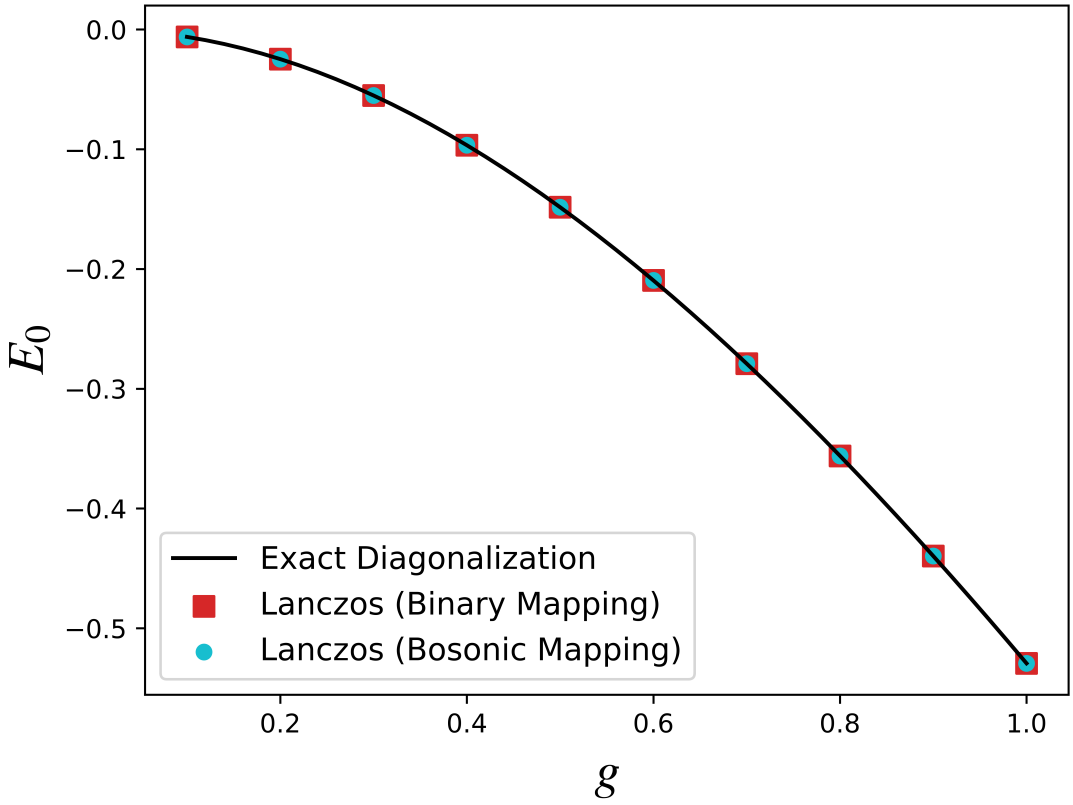


Figure 3.3: Ground state energy for $N = 2$ computed using Lanczos diagonalization in the binary as well as the unary qubit representations. Exact results computed using the rotor Hamiltonian are exhibited for comparison.

Note that the unary mapping yields a large Hilbert space dimension even for small systems. For $N = 3$, the Hilbert space dimension with $n = 4$ and $l = 3$ is 2^{24}. Consequently, we use linear operators for the sparse diagonalization simulations in Figs. 3.3 and 3.4 which can be constructed using the action of the Hamiltonian on an arbitrary vector in the lexicographically ordered computational qubit basis.

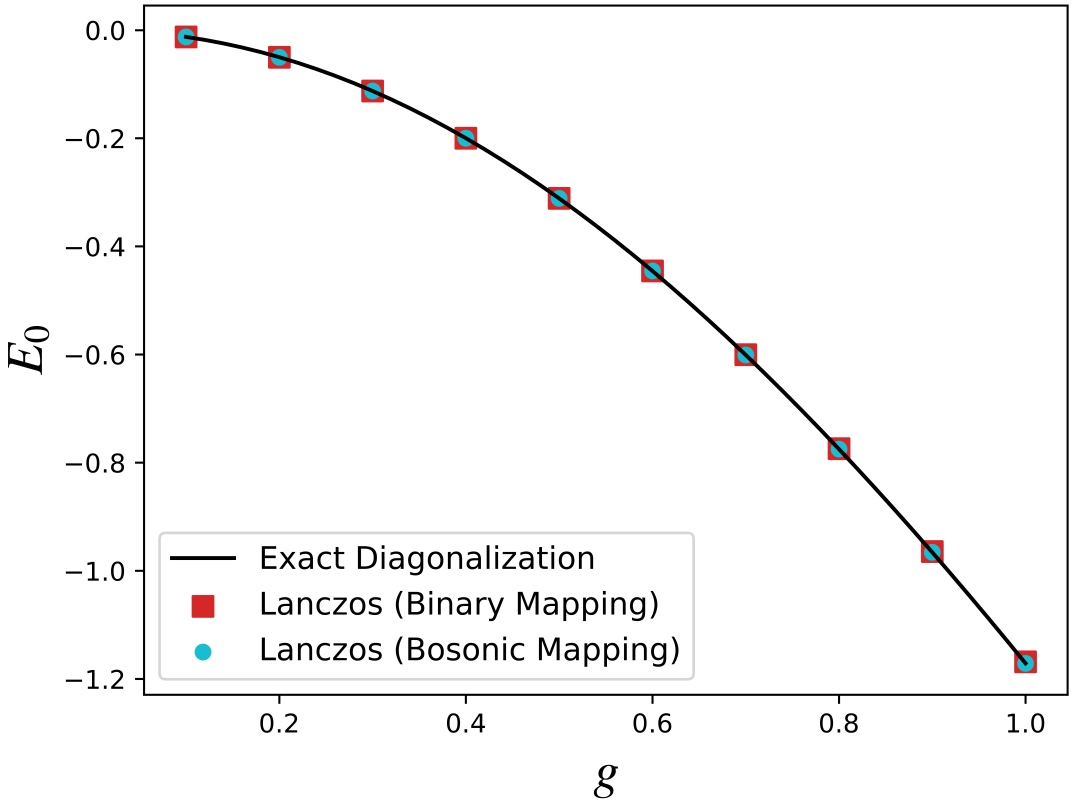


Figure 3.4: Ground state energy for $N = 3$ computed using Lanczos diagonalization in the binary as well as the unary qubit representations. Exact results computed using the rotor Hamiltonian are exhibited for comparison.

This action for the unary encoded Hamiltonian is given by,

$$(H_0 v)_t = ((i-l)^2 + (j-l)^2 + (k-l)^2) v_t, \tag{3.50}$$

$$(H_1 v)_t = \frac{3}{4}(v_a + v_b + v_c + v_d) - \frac{1}{4}(v_e + v_f + v_g + v_h) \tag{3.51}$$

Here, H_0 is the diagonal angular momentum operator and H_1 is the pairwise nearest neighbor dipole-dipole interaction. The above equations define the non-zero part of the action. The index t is constructed using the individual rotor indices $0 \leq i, j, k \leq d-1$ and is given by,

$$t = 2^{i+2d} + 2^{j+d} + 2^k \tag{3.52}$$

For all $t' \neq t$, $(Hv)_{t'} = 0$. The indices a to d correspond to either raising or lowering both indices associated with a single pair of rotors,

$$a = 2^{(i-1)\%d+2d} + 2^{(j-1)\%d+d} + 2^k, \quad b = 2^{(i+1)\%d+2d} + 2^{(j+1)\%d+d} + 2^k, \tag{3.53}$$

$$c = 2^{i+2d} + 2^{(j-1)\%d+d} + 2^{k-1}, \quad d = 2^{i+2d} + 2^{(j+1)\%d+d} + 2^{k+1} \tag{3.54}$$

Finally, the indices e to h correspond to raising one and lowering the other index associated with one pair of rotors,

$$e = 2^{(i-1)\%d+2d} + 2^{(j+1)\%d+d} + 2^k, \quad f = 2^{(i+1)\%d+2d} + 2^{(j-1)\%d+d} + 2^k, \tag{3.55}$$

$$g = 2^{i+2d} + 2^{(j-1)\%d+d} + 2^{k+1}, \quad h = 2^{i+2d} + 2^{(j+1)\%d+d} + 2^{k-1} \tag{3.56}$$

The case for $N = 2$ can be constructed analogously. To simulate the binary mapping, we use the sparse qubit operator implementation provided by OpenFermion and Tangelo.[119,120]

3.3.2 Phase Estimation

We used noiseless state vector simulations to assess the utility of quantum phase estimation with both qubit mappings. Figs. 3.5 and 3.6 show the convergence of the 4th order propagator to the exact ground state energy for $N = 2$ and $N = 3$ respectively, with the sparse mapping. We shift the spectrum so that the ground state energy is 0.5,

$$H \to H - (E_0 - 0.5) \tag{3.57}$$

which allows us to simulate the system with a small register. Larger registers would be needed for higher precision corrections to the measured energies. For both values of N in Figs. 3.5 and 3.6, $g = 2.0$, $n = 4$ and $l = 3$ which yields $k = 3$ and $d = 8$. The bar charts show the probability of measuring all 16 possible energy values given a 4 qubit register. The exact E_0 is also shown for reference. We find that $P = 20$ Trotter steps is sufficient for convergence in both cases. The insets show convergence in $\Delta t = 1/P$.

For all of the simulations shown in Figs. 3.5 and 3.6, the exact ground state was used as the input state $|\varphi\rangle$. As discussed above, in the absence of an approximate ground state, we need to rescale and shift the spectrum (see Eq. (3.49)) so that all of the eigenvalues $\tilde{E}_i$ of the resulting Hamiltonian $\tilde{H}$ can be uniquely mapped to phases $\varphi \in [0.0, 1.0)$. This places a lower bound on the number of ancilla qubits required for QPE. For ground state calculations, note that the energy gap that needs to be resolved is $\Delta\tilde{E}_1 = \tilde{E}_1 - \tilde{E}_0$.

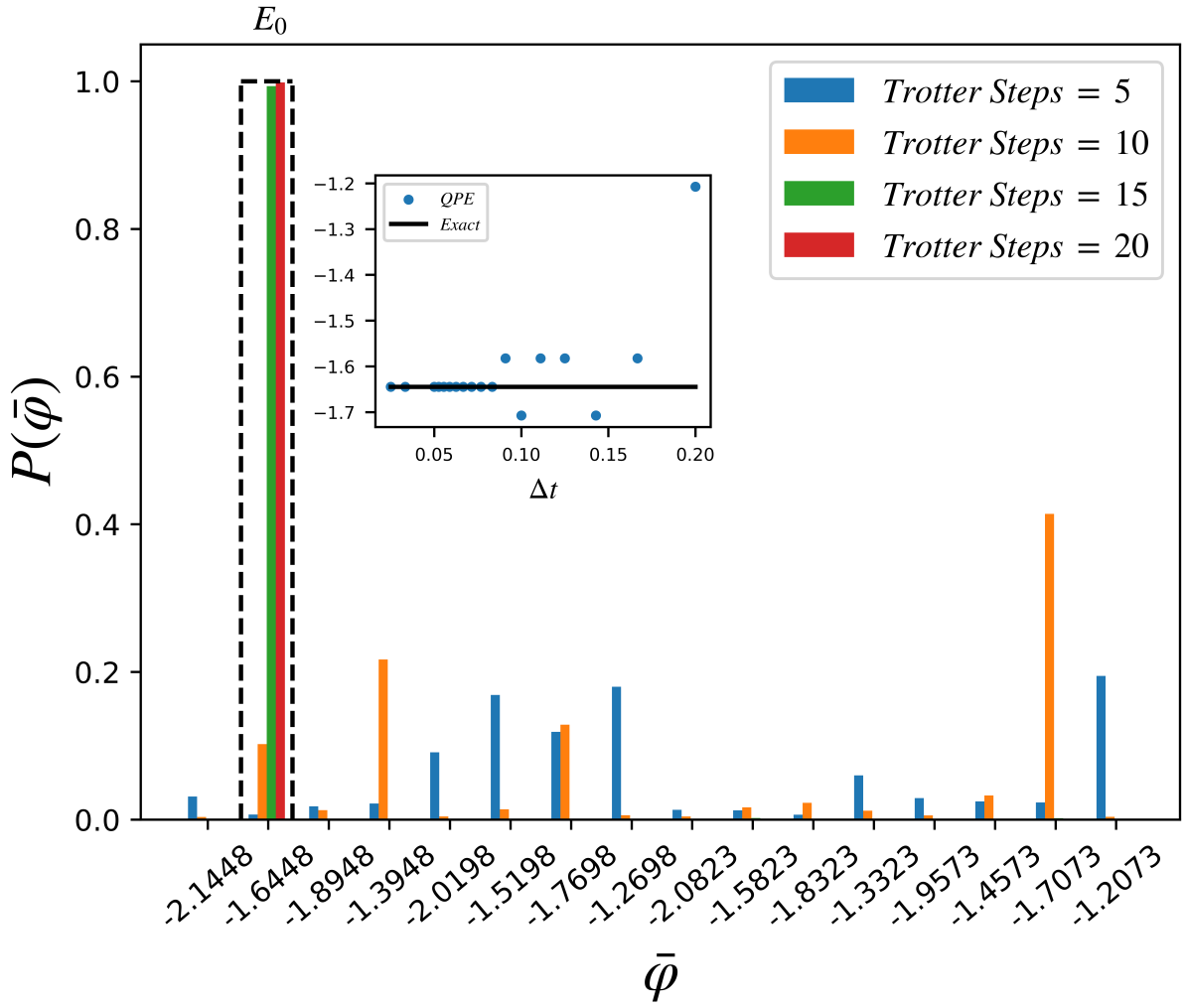


Figure 3.5: Probability of measuring any of the 16 possible values of the phase $\bar{\varphi} = E_0$ associated with $U = e^{-i2\pi H}$ for $g = 2.0$, $N = 2$ with the binary mapping representation for different numbers of Trotter steps. The insets show convergence with Δt, the reciprocal number of Trotter steps. The exact E_0 value is indicated for reference.

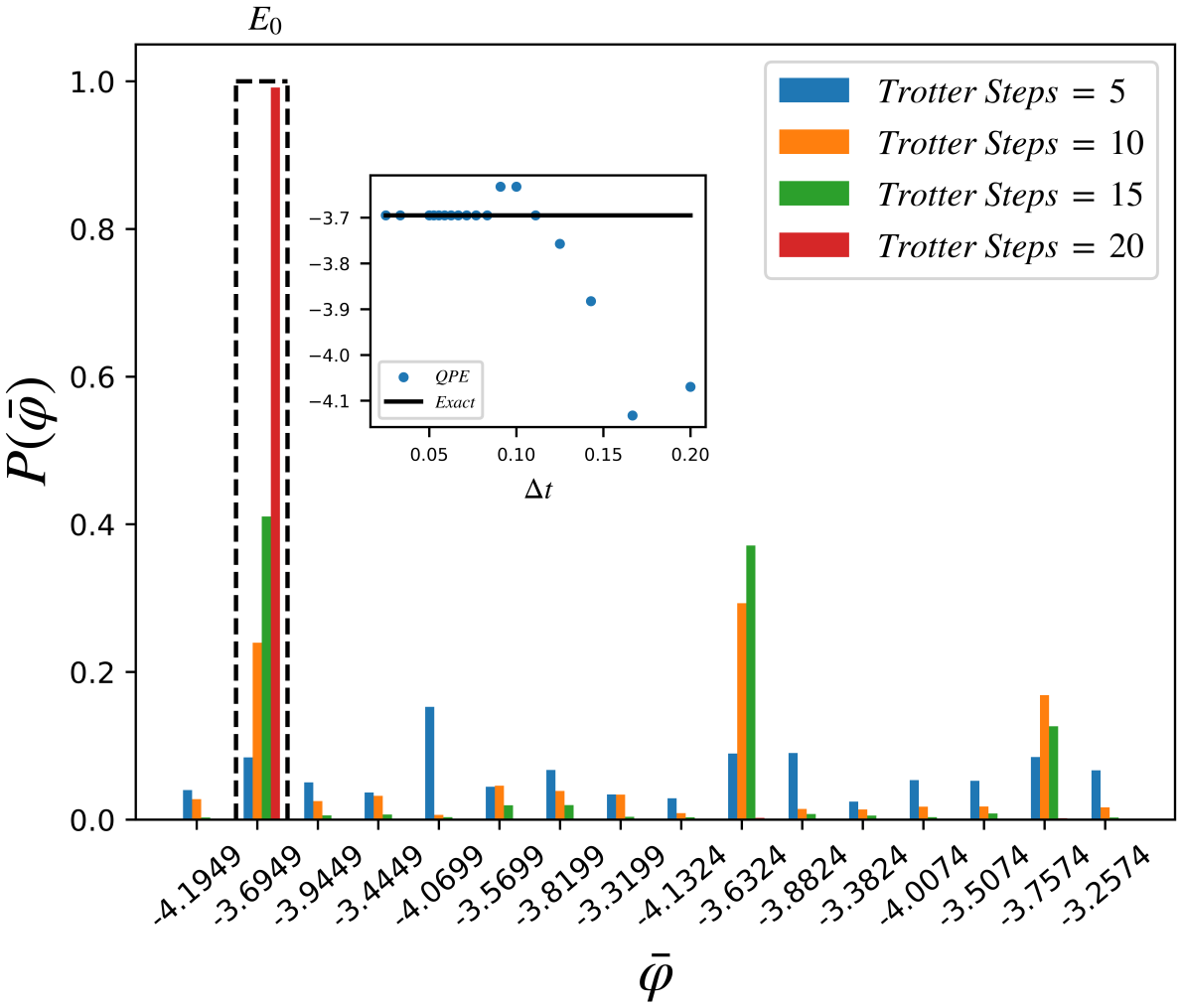


Figure 3.6: Probability of measuring any of the 16 possible values of the phase $\bar{\varphi} = E_0$ associated with $U = e^{-i2\pi H}$ for $g = 2.0$, $N = 3$ with the binary mapping representation for different numbers of Trotter steps. The insets show convergence with Δt, the reciprocal number of Trotter steps. The exact E_0 value is indicated for reference.

Figure	N	g	n	l	d	k	r	Total Qubit Count	Pauli Weight
3.5	2	2.0	4	3	8	3	4	10	6
3.6	3	2.0	4	3	8	3	4	13	6

Table 3.1: Parameters used for Trotter convergence QPE results exhibited in Figs. 3.5 and 3.6. N is the number of rotors, g is the coupling strength, and n and l, respectively, are the maximum and minimum frequency cutoffs used in the binary mapping. $d = n + l + 1$ is the total number of momentum basis states used for each rotor and k is the number of qubits required to encode a single discretized rotor. Here, r represents the QPE register size. The total qubit count corresponding to each QPE simulation is given by $Nk + r$ and the Maximum Pauli weight for the binary encoding is $2k$.

If we use an r-bit approximation to measure $\tilde{E}_1$ and $\tilde{E}_0$, the precision error in each measurement is bounded above by $1/2^{r+1}$. Therefore, to resolve the two values separately, the energy gap $\Delta\tilde{E}_1$ must be larger than $2/2^{r+1} = 1/2^r$. This implies the following constraint on the size of the QPE register,[47]

$$\frac{1}{2^r} < \Delta\tilde{E}_1 \Rightarrow r > \log_2\left(\frac{1}{\Delta\tilde{E}}\right) \Rightarrow r \geq \left\lceil \log_2\left(\frac{1}{\Delta\tilde{E}}\right)\right\rceil \tag{3.58}$$

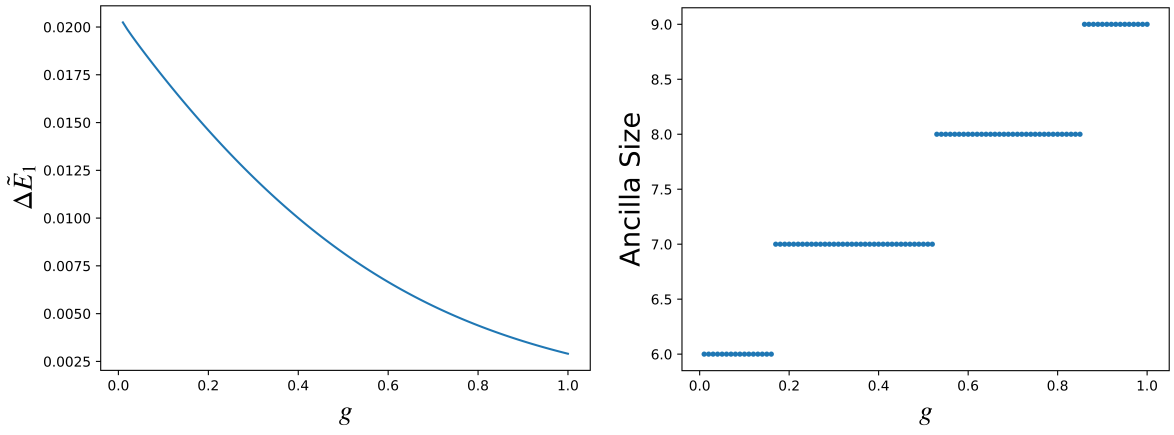


Figure 3.7: The first energy gap of the scaled Hamiltonian and the corresponding lower bound on the QPE ancilla size for a coplanar chain of 3 rotors for $g \in (0.0, 1.0]$.

Fig. 3.7 displays the energy gap and the minimum required QPE ancilla size for a coplanar chain of $N = 3$ rotors for $g \in (0.0, 1.0]$. The gap was computed using ED calculations of

the scaled Hamiltonian in the momentum representation. For the values of g considered, the largest required ancilla size is 9 qubits and smallest is 6 qubits. For a 3 rotor chain with $n = 4$ and $l = 3$, we need 8 qubits to encode the state. This implies that for a coplanar chain of 3 rotors, QPE would require less than 20 logical qubits. Given the seemingly modest requirements, it would be an interesting next step to explore the viability of implementing this on a near-term quantum device such as a trapped-ion simulator capable of computing ground state properties of typical spin models in statistical mechanics.[121,122]

3.4 Conclusions & Outlook

In this chapter, we discussed two approaches for mapping a q-dimensional lattice of planar rotors to a $(q+1)$-dimensional lattice of spin-1/2 particles. The number of qubits grows linearly with the number of particles in both encodings. In the binary encoding, the Pauli weight of the interaction grows logarithmically with the single rotor basis set size used for truncation. However, for the unary encoding, the potential is represented by a sum of 4-body interaction terms. This comes at the price of needing a larger number of qubits i.e. the number of qubits required for the unary encoding grows linearly with the single rotor basis set size instead of logarithmically, as with the binary mapping.

We tested our mappings computationally by calculating the ground state energy of small chains ($N = 2$ and $N = 3$) in the qubit representations and comparing the results to ED in the momentum representation. We also performed some preliminary QPE simulations to determine the number of Trotter steps required for convergence. For this calculation, to avoid needing a large QPE ancilla, we shifted the spectrum so that the binary encoded Hamiltonian ground state energy could be represented by a small number of bits. Finally, we determined the size of the QPE ancilla that would be required to resolve the ground state energy uniquely for $g \in (0.0, 1.0]$ for small chains.

Having established the applicability of quantum algorithms for simulating planar rotor lattices, we will now examine various approximate state preparation techniques that can be used to optimize QPE calculations. This will involve determining whether either of these mappings can be efficiently targeted using VQE to converge to the ground state. One promising candidate for this is the Hamiltonian Variational Ansatz (HVA) which has been successfully used to simulate the Heisenberg and Ising models in statistical mechanics.[123–125]

Another possible contender would be the Matrix Product State (MPS) ansatz which has shown promise in the context of simulating the Heisenberg model on Kagome lattices.[126]

Another future research direction would be to simulate the effect of hardware noise in VQE calculations targeting lattices of planar rotors.[126,127] This could be done by applying a depolarizing noise channel after every 1-qubit and 2-qubit gate[47,127] and would help us assess the noise threshold requirements for VQE simulations in these representations. Following that, we could then explore the possibility of simulating small lattices with current quantum devices that are typically used to simulate spin models in condensed matter physics.[121,122]

Chapter 4

Conclusions & Future Directions

In this thesis, we developed the pair approximation technique for simulating the ground state properties of planar rotor lattices using Path Integral Monte Carlo (PIMC) methods. We also investigated two qubit encodings for planar rotor lattices and discussed some preliminary Quantum Phase Estimation (QPE) simulation results. In Chapter 1, we introduced planar rotor lattices and various grid approximations including the Discrete Variable Representation (DVR) of the problem. We also discussed the Feynman-Kac theorem which is required to derive the pair factorization. The introductory chapter concludes with a discussion of path integral sampling techniques i.e. Metropolis-Hastings (MH) and Gibbs sampling.

Chapter 2 is dedicated to the pair approximation. The approach we introduced uses a DVR grid which allows us to use rejection free sampling to optimize the calculations. We also analyzed the pair propagator using Wigner-Kirkwood expansions and proved that the factorization error is $\mathcal{O}(\tau^3)$. We tested the approach on a coplanar chain of 150 planar rotors with a pairwise dipole-dipole interaction, a system that has been shown to undergo a (1+1)d Ising universality class quantum phase transition in the coupling strength. We computed energetic properties i.e. the ground state energy and the chemical potential. We also calculated two pertinent structural properties: the orientational correlation function and the Binder ratio. Comparing our results to Density Matrix Renormalization Group (DMRG) calculations, we found that the pair approximation yields excellent convergence in the ordered as well as the disordered phase. However, close to the transition, the factorization error increases as many-body correlations become relevant. This can be seen

in the orientational correlation function calculations. Moreover, close to the transition point, as is characteristic of quantum phase transitions, our path integral simulations experience critical slowing down leading to large auto-correlation times and burn-in periods, which is reflected in the convergence times of our Binder ratio simulations.

In chapter 3, we discussed two possible qubit encodings for planar rotor lattices. Both of the mappings we introduced use the momentum representation of the problem because that canonically admits a discrete basis due to the presence of periodic boundaries in the position representation. The first mapping follows by representing each momentum eigenstate of the q-dimensional lattice of rotors in binary and mapping the corresponding projectors to spin-1/2 projectors on a higher dimensional lattice. The second mapping is motivated by the qubit encodings developed for bosonic systems. This involves first embedding the planar rotor lattice in a larger qubit Hilbert space and then projecting down to the subspace associated with the physical system. We tested both of these encodings on small chains of rotors using sparse diagonalization. We also performed QPE simulations to determine the number of Trotter steps required for convergence to the exact results (with a 4th order Trotter factorization) and determined the size of the QPE register necessary for calculating ground state properties of small chains on a quantum device.

4.1 Future Work

In this section, we discuss various future research directions to further optimize Quantum Monte Carlo (QMC) simulations of planar rotor lattices as well as nascent projects involving the qubit encodings developed in chapter 3.

4.1.1 Entanglement Entropy

Entanglement entropy is another important property in the context of many-body physics since it provides a measure of entanglement between subsystems.[47,128,129] In particular, entanglement entropy calculations allow one to compute the central charge critical exponent associated with quantum phase transitions.[19,73] For 1d lattices of rotors, we partition the lattice by placing N_1 sites in partition A and the remaining $N_2 = N - N_1$ sites in partition B as shown in Fig. 4.1. Then, the Von-Neumann entropy is defined as,[47]

$$S = -\mathrm{Tr}(\rho_A \ln(\rho_A)), \quad \rho_A = \mathrm{Tr}_B(\rho), \quad \rho = |E_0\rangle\langle E_0| \tag{4.1}$$

where ρ is the density matrix associated with the ground state of the full system and ρ_A is the reduced density matrix of subsystem A defined by the partial trace of ρ over subsystem B.

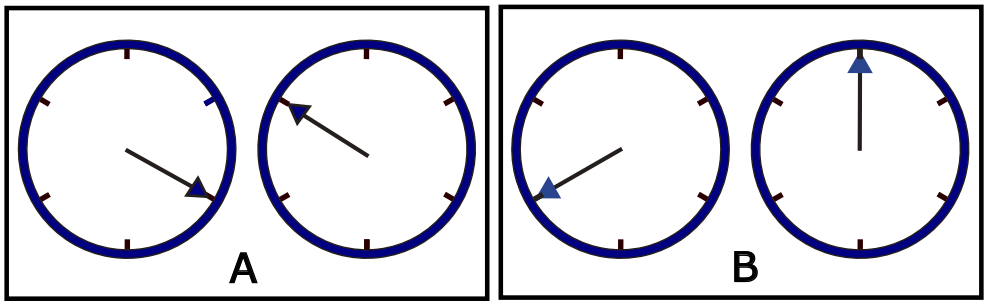


Figure 4.1: Partitioning of a chain of discretized planar rotors into subsystems A and B with $N = 4$, $N_A = 2$ and $N_B = 2$.

While we cannot compute the Von Neumann entropy with path integrals directly, we can compute a related function that can also be used as a measure of entanglement called the second Renyi entropy.[77,130] The nth Renyi entropy is defined as,

$$S_n = \frac{1}{1-n} \ln(\mathrm{Tr}(\rho^n)) \tag{4.2}$$

In the limit of $n \to 1$, $S_n \to S$. S_2 can be calculated using PIGS using the replica trick.[77,130] This involves calculating the ratio N/D given by,[77]

$$\begin{aligned} N = \int d\boldsymbol{\phi}_A d\boldsymbol{\phi}'_A d\boldsymbol{\phi}_B d\boldsymbol{\phi}'_B \ \langle \boldsymbol{\phi}_A, \boldsymbol{\phi}_B | e^{-\frac{\beta}{2}H} | \Psi_T \rangle \langle \Psi_T | e^{-\frac{\beta}{2}H} | \boldsymbol{\phi}'_A, \boldsymbol{\phi}_B \rangle \\ \times \langle \boldsymbol{\phi}'_A, \boldsymbol{\phi}'_B | e^{-\frac{\beta}{2}H} | \Psi_T \rangle \langle \Psi_T | e^{-\frac{\beta}{2}H} | \boldsymbol{\phi}_A, \boldsymbol{\phi}'_B \rangle \end{aligned} \tag{4.3}$$

$$\begin{aligned} D = \int d\boldsymbol{\phi}_A d\boldsymbol{\phi}'_A d\boldsymbol{\phi}_B d\boldsymbol{\phi}'_B \ \langle \boldsymbol{\phi}_A, \boldsymbol{\phi}_B | e^{-\frac{\beta}{2}H} | \Psi_T \rangle \langle \Psi_T | e^{-\frac{\beta}{2}H} | \boldsymbol{\phi}_A, \boldsymbol{\phi}_B \rangle \\ \times \langle \boldsymbol{\phi}'_A, \boldsymbol{\phi}'_B | e^{-\frac{\beta}{2}H} | \Psi_T \rangle \langle \Psi_T | e^{-\frac{\beta}{2}H} | \boldsymbol{\phi}'_A, \boldsymbol{\phi}'_B \rangle \end{aligned} \tag{4.4}$$

Here, note that we have two replicas of the same system; let us call them the primed and the unprimed replicas. We can construct our path integral for both N and D and factor the high-temperature density as before. Then, the paths for N correspond to swapping subsystem A with A' at the middle bead whereas D corresponds to evolving both replicas

in imaginary time independently. We can calculate N/D by starting our simulation in one sector (the swapped or unswapped sector) and then proposing transitions to the other at each simulation time-step. The ratio of the amount of time the system spends in the swapped versus the unswapped sector statistically converges to N/D. Typically, the primitive factorization is used in conjunction with MH for these calculations which converges slowly. Consequently, a future research direction in the context of the pair-DVR technique will be to assess the benefit of using the pair factorization with Gibbs sampling for Renyi entropy calculations.

4.1.2 Higher Dimensional Lattices

In this thesis, we restricted our focus to a 1d lattice of rotors. As discussed in the introduction, an interesting system from a physics perspective is the Quantum Anisotropic Planar Rotor (QAPR) model in which planar rotors are placed on a 2d lattice.[17,25–27] This system has been studied in the literature with a nearest-neighbor quadrupolar interaction using mean-field theory as well as Monte Carlo (MC) simulations.[17,25] Mean field treatments have suggested the existence of a re-entrant phase transition; as the temperature is lowered, the system enters an ordered phase and then subsequently re-enters a disordered phase.[25] Consequently, it would be interesting to investigate if the pair approximation can be used to study that system and if so, determine the phase diagram as well as the critical exponents of the transitions to specify the universality class, provided our techniques can offer sufficient resolution near criticality.

Dipolar planar rotor lattices in 3d can be used to model water confined in crystals such as Beryl and Cordierite, as discussed in chapter 1.[23,24] This system has been shown to exhibit ferroelectric behavior in experiments.[24] Therefore, another promising future direction would be to explore the phase diagram of such systems as a function of temperature as well as the interaction strength using MC simulations. Since this would require simulating a large number of rotors for a range of different parameters, the pair approximation with Gibbs sampling would be a promising candidate for calculating ground state properties efficiently. Moreover, it would also be interesting to develop continuous formulations of the pair approximation that do not require the use of a DVR (to avoid the sign problem) for finite temperature calculations such as those used to study superfluidity in condensed Helium.[11]

4.1.3 Stochastic Series Expansion

In chapter 2, we saw that near criticality, the correlation function had larger convergence errors. Moreover, the Binder ratio calculations suffered from critical slowing down near the transition point. As discussed in chapter 2, these are general feature of quantum phase transitions that can also be observed in spin-1/2 lattices such as the Heisenberg model and the Transverse Field Ising Model (TFIM).[21,22] The critical slowing down in particular is a consequence of a loss of ergodicity characteristic of phase transitions. For spin-1/2 lattices, these issues are usually tackled via the use of cluster moves that change the configuration of a group of sites in a single step. One of the most successful algorithmic approaches to achieve this in QMC is the Stochastic Series Expansion (SSE) technique.[48–50] To briefly explore its implementation, consider the TFIM Hamiltonian,[3,50]

$$H = \sum_{i \neq j}^{N} J_{ij} \sigma_i^z \sigma_j^z - h \sum_{i=1}^{N} \sigma_i^x \tag{4.5}$$

SSE algorithms have been developed for this model with arbitrary interactions in Ref. 50. We start by redefining the Hamiltonian up to a constant offset as follows,

$$H = \sum_{i=1}^{N} \sum_{j=0}^{N} H_{ij}, \quad H_{i,0} = h\sigma_i^x, \quad H_{ij} = |J_{ij}| - J_{i,j}\sigma_i^z \sigma_j^z \;\; (i \neq j), \quad H_{i,i} = h \tag{4.6}$$

Then, the operator $e^{-\beta H}$ is expanded in powers of β to express Z as follows,

$$Z = \sum_{\alpha} \sum_{n=0}^{\infty} \frac{(-\beta)^n}{n!} \sum_{S_n} \langle \alpha | H_{b_1} ... H_{b_n} | \alpha \rangle \tag{4.7}$$

Here, we have expanded each power of H as a sum of the constituent terms and evaluated the product. This yields a sum over all possible n length strings S_n of indices $b_1, ..., b_n$ corresponding to the different terms that sum to yield the many-body Hamiltonian. Note that here, b_k can be a a bond index (i, j) (such that $i, j \geq 1$) or a site index $i \geq 1$. Each of the terms H_{b_k} are proportional to either diagonal on-site terms or off-diagonal one-body σ^x terms that flip the spin they act on (in the σ^z-basis). Moreover, the trace is evaluated in the σ^z basis in the above equation. It can be shown that the higher orders contributions to the partition function in n are diminishing, so the sum can be truncated to some finite

integer L.[49] Finally, the sum over n can be removed entirely by introducing a combinatorial correction and denoting $H_0 = I$ to get,

$$Z = \sum_{\alpha_1,\ldots,\alpha_L} \sum_{S_L} \frac{(-\beta)^n (L-n)!}{L!} \langle \alpha_1 | H_{b_1} | \alpha_2 \rangle \ldots \langle \alpha_L | H_{b_L} | \alpha_1 \rangle \tag{4.8}$$

Now, we are summing over all sequences of length L and the indices can include 0 as well. Here, n is the number of indices that are not equal to 0 in a given sequence. To evaluate this sum stochastically, we need to sample configurations of states and operators such that the trace periodicity condition is met. For the TFIM, this is done by starting with a random configuration satisfying this constraint and proposing changes. The diagonal moves are constructed by finding operators in the string corresponding to $H_0 = I$ and proposing a replacement by $J_{ij}\sigma_i\sigma_j$ for i, j random. These are accepted or rejected with a Metropolis criterion. Conversely, once a non-trivial diagonal operator is found in the string, a removal is proposed in the same way and either accepted or rejected. This allows for the sampling of different values of n.

While diagonal moves are simple and do not affect the trace periodicity condition, the same is not true for off-diagonal updates. To add and remove off-diagonal terms, we form clusters of spins in NL space that are closed. Each cluster is formed by finding a diagonal operator and connecting all spins above or below that operator in L space (time dimension) with a line. If it is a two-body operator, lines are extended for both particles in both directions in time and, if it is a one-body operator, lines are only extended for the particle associated with the operator in the increasing time direction. For the TFIM, the decomposition provided in Eq. (4.6) guarantees that all such clusters close, provided the lines are continued periodically in L space. All the spins connected by a single line are considered to be part of a single loop. Then, all of the spins in a single cluster are flipped with probability 1/2. This has the effect of replacing one-body diagonal operators with one-body off-diagonal operators.

The SSE algorithm for the TFIM described above has been shown in numerous works to be more efficient than conventional path integral techniques.[49,50] Therefore, it is instructive to try and construct something similar for our system. To this end, recall from chapter 1 that our planar rotor chain Hamiltonian can be expressed in terms of clock and shift operators (which are generalizations of σ^z and σ^x),

$$H = A_1 \sum_{i=1}^{N-1} (\sigma_i \sigma_{i+1} + \sigma_i^+ \sigma_{i+1}^+) + A_2 \sum_{i=1}^{N-1} (\sigma_i^+ \sigma_{i+1} + \sigma_i \sigma_{i+1}^+) + \frac{B}{2} \sum_{i=1}^{N} (\tau_i + \tau_i^+) + \frac{2N}{\Delta^2} \tag{4.9}$$

Here, σ is the clock operator that generalizes σ^z and τ is the shift operator which generalizes σ^x,[31]

$$(\sigma)_{nm} = \delta_{nm} e^{i2\pi n/d}, \quad (\tau)_{nm} = \delta_{n,m-1} \tag{4.10}$$

Both σ and τ are d dimensional square matrices and the subtraction in the definition of τ is modulo d because it is the cyclic shift operator. SSE techniques have been recently also developed for the Z_d chain of rotors defined by the Hamiltonian,[131]

$$H = A \sum_{i=1}^{N-1} (\sigma_i^+ \sigma_{i+1} + \sigma_i \sigma_{i+1}^+) + \frac{B}{2} \sum_{i=1}^{N} (\tau_i + \tau_i^+) \tag{4.11}$$

The SSE appraoch for this relies on generalizing the TFIM SSE. The diagonal updates are done in the same way. However, the off-diagonal cluster flip updates are generalized to shift updates by a random integer between 1 and $d-1$. Various approaches exist for determining the required clusters. One possible generalization of the TFIM clusters is as follows: start with a 2-body diagonal operator and include both rotors in N space in the cluster. Then extend in the positive time direction and close loops when a shift operator is encountered. Finally, propose a shift for all rotors in the cluster. While this approach has been useful for simulating the Z_d chain, it remains to be seen whether it will retain its utility for the Z_2 chain. Consequently, another future research direction would be to explore the efficacy of using this SSE algorithm in the clock-shift representation for the Z_2 chain.

4.1.4 Variational Quantum Eigensolver

In chapter 3, we discussed QPE results for our qubit mappings. However, the existence of hardware errors makes QPE simulations on quantum devices difficult.[132] For near-term devices and for QPE state preparation, numerous Variational Quantum Eigensolver (VQE) approaches have been developed.[124,125] Therefore, one future research direction will be to explore the convergence properties of different VQE ansatz such as the Hamiltonian Variational Ansatz (HVA) and the Matrix Product State (MPS) ansatz.[123,126] It would be particularly interesting to investigate if either one of these encodings exhibit faster convergence compared to the other. Moreover, it is also relatively easy to simulate the effect of hardware noise in VQE circuits.[127] Therefore, we also intend to employ these noise models to explore the error correction requirements for VQE techniques targeting planar rotor lattices.

References

[1] P. W. Anderson, Science **177**, 393 (1972).

[2] M. Kardar, *Statistical Physics of Fields*, Cambridge University Press, 2007.

[3] S. Sachdev, *Quantum Phase Transitions*, Cambridge University Press, 2011.

[4] N. Goldenfeld, *Lectures On Phase Transitions And The Renormalization Group*, CRC Press, 2018.

[5] H. E. Stanley, *Introduction to Phase Transitions and Critical Phenomena*, Oxford University Press, 1987.

[6] M. Kardar, *Statistical Physics of Particles*, Cambridge University Press, 2007.

[7] E. Fradkin, *Field Theories of Condensed Matter Physics*, Cambridge University Press, 2013.

[8] R. Mondaini, P. Nikolić, and M. Rigol, Physical Review A **92**, 013601 (2015).

[9] A. Pelissetto and E. Vicari, Physics Reports **368**, 549 (2002).

[10] M. Campostrini, M. Hasenbusch, A. Pelissetto, and E. Vicari, Physical Review B **74**, 144506 (2006).

[11] D. M. Ceperley, Reviews of Modern Physics **67**, 279 (1995).

[12] J. Bardeen, L. N. Cooper, and J. R. Schrieffer, Physical Review **108**, 1175 (1957).

[13] F. Verstraete et al., Nature Reviews Physics **5**, 273 (2023).

[14] U. Schollwöck, Annals of Physics **326**, 96 (2011), January 2011 Special Issue.

[15] T. D. Crawford and H. F. Schaefer III, *An Introduction to Coupled Cluster Theory for Computational Chemists*, John Wiley & Sons, Ltd, 2000.

[16] Y. Yan and D. Blume, Journal of Physics B: Atomic, Molecular and Optical Physics **50**, 223001 (2017).

[17] B. Hetényi and B. J. Berne, The Journal of Chemical Physics **114**, 3674 (2001).

[18] D. Marx and M. H. Müser, Journal of Physics: Condensed Matter **11**, R117 (1999).

[19] T. Serwatka and P.-N. Roy, The Journal of Chemical Physics **160**, 104302 (2024).

[20] W. Zhang et al., The Journal of Chemical Physics **162**, 014106 (2025).

[21] U. Wolff, Nuclear Physics B - Proceedings Supplements **17**, 93 (1989).

[22] C. Bonati and M. D'Elia, Physical Review E **98**, 013308 (2018).

[23] B. P. Gorshunov et al., Nature Communications **7** (2016).

[24] M. A. Belyanchikov et al., Nature Communications **11** (2020).

[25] B. Hetényi, S. Scandolo, and E. Tosatti, Journal of Low Temperature Physics **139**, 753 (2005).

[26] D. Marx and P. Nielaba, The Journal of Chemical Physics **102**, 4538 (1995).

[27] Y. A. Freiman, B. Hetényi, and S. M. Tretyak, 2d and 3d quantum rotors in a crystal field: Critical points, metastability, and reentrance, in *Metastable Systems under Pressure*, Springer, 2010.

[28] J. M. Kosterlitz and D. J. Thouless, Journal of Physics C: Solid State Physics **6**, 1181 (1973).

[29] M. Gouvêa, F. Mertens, A. Bishop, and G. Wysin, Journal of Physics: Condensed Matter **2**, 1853 (1990).

[30] S. Whitsitt, R. Samajdar, and S. Sachdev, Physical Review B **98**, 205118 (2018).

[31] P. Fendley, Journal of Statistical Mechanics: Theory and Experiment **2012**, P11020 (2012).

[32] H. Bernien et al., Nature **551**, 579 (2017).

[33] P. Fendley, K. Sengupta, and S. Sachdev, Physical Review B **69**, 075106 (2004).

[34] R. Samajdar, S. Choi, H. Pichler, M. D. Lukin, and S. Sachdev, Physical Review A **98**, 023614 (2018).

[35] S. T. Thornton and J. B. Marion, *Classical Dynamics of Particles and Systems*, Brooks/Cole, 2004.

[36] J. J. Sakurai and J. Napolitano, *Modern Quantum Mechanics*, Cambridge University Press, 2020.

[37] J. D. Jackson, *Classical Electrodynamics*, John Wiley & Sons, 1999.

[38] B. P. Dolan, arXiv preprint arXiv:2112.12216 (2021).

[39] A. Scardicchio, Physics Letters A **300**, 7 (2002).

[40] H. Kleinert, *Path integrals in quantum mechanics, statistics, polymer physics, and financial markets*, World Scientific Publishing Company, 2006.

[41] G. Guillon, T. Zeng, and P.-N. Roy, The Journal of Chemical Physics **138** (2013).

[42] H. Kleinert and S. V. Shabanov, Physics letters A **232**, 327 (1997).

[43] R. Meyer, The Journal of Chemical Physics **52**, 2053 (1970).

[44] D. T. Colbert and W. H. Miller, The Journal of Chemical Physics **96**, 1982 (1992).

[45] J. Light, I. Hamilton, and J. Lill, The Journal of Chemical Physics **82**, 1400 (1985).

[46] J. C. Light and T. Carrington Jr, Advances in Chemical Physics **114**, 263 (2000).

[47] M. A. Nielsen and I. L. Chuang, *Quantum Computation and Quantum Information*, Cambridge University Press, 2010.

[48] A. W. Sandvik, Physical Review B **59**, R14157 (1999).

[49] A. W. Sandvik, arXiv preprint arXiv:1909.10591 (2019).

[50] A. W. Sandvik, Physical Review E **68**, 056701 (2003).

[51] D. Marx, S. Sengupta, and P. Nielaba, The Journal of Chemical Physics **99**, 6031 (1993).

[52] A. Sarsa, K. Schmidt, and W. Magro, The Journal of Chemical Physics **113**, 1366 (2000).

[53] V. Y. Pan and Z. Q. Chen, The complexity of the matrix eigenproblem, in *Proceedings of the Thirty-First Annual ACM Symposium on Theory of Computing*, 1999.

[54] M. Suzuki, Communications in Mathematical Physics **51**, 183 (1976).

[55] M. Suzuki, Physics Letters A **113**, 299 (1985).

[56] B. C. Hall, *Quantum theory for mathematicians*, Springer, 2013.

[57] A. Pérez and M. E. Tuckerman, The Journal of Chemical Physics **135**, 064104 (2011).

[58] N. Makri and W. H. Miller, The Journal of Chemical Physics **90**, 904 (1989).

[59] J. A. Barker, The Journal of Chemical Physics **70**, 2914 (1979).

[60] E. L. Pollock and D. M. Ceperley, Physical Review B **30**, 2555 (1984).

[61] N. G. Van Kampen, *Stochastic processes in physics and chemistry*, Elsevier, 1992.

[62] P. Del Moral, *Feynman-Kac formulae*, Springer, 2004.

[63] N. G. Van Kampen, Journal of Statistical Physics **44**, 1 (1986).

[64] L. Grafakos, *Classical and modern Fourier analysis*, Prentice Hall, 2008.

[65] M. A. Pinsky, *Introduction to Fourier Analysis and Wavelets*, American Mathematical Society, 2023.

[66] R. S. Strichartz, *A guide to distribution theory and Fourier transforms*, World Scientific Publishing Company, 2003.

[67] D. V. Vassilevich, Physics Reports **388**, 279 (2003).

[68] Y. Fujiwara, T. A. Osborn, and S. F. J. Wilk, Physical Review A **25**, 14 (1982).

[69] S. F. J. Wilk, Y. Fujiwara, and T. A. Osborn, Physical Review A **24**, 2187 (1981).

[70] I. G. Avramidi, *Heat Kernel Method and its Applications*, Springer, 2015.

[71] F. C. Klebaner, *Introduction to stochastic calculus with applications*, World Scientific Publishing Company, 2012.

[72] R. Serfozo, *Basics of Applied Stochastic Processes*, Springer, 2009.

[73] T. Serwatka, R. G. Melko, A. Burkov, and P.-N. Roy, Physical Review Letters **130**, 026201 (2023).

[74] C. P. Robert and G. Casella, *Monte Carlo Statistical Methods*, Springer, 2004.

[75] F. Faizi, G. Deligiannidis, and E. Rosta, Journal of Chemical Theory and Computation **16**, 2124 (2020).

[76] M. S. Moeed, T. Serwatka, and P.-N. Roy, The Journal of Chemical Physics **162**, 024113 (2025).

[77] T. Sahoo, D. Iouchtchenko, C. Herdman, and P.-N. Roy, The Journal of Chemical Physics **152** (2020).

[78] A. Nakayama and N. Makri, The Journal of Chemical Physics **125** (2006).

[79] M. Casula, D. M. Ceperley, and E. J. Mueller, Physical Review A **78**, 033607 (2008).

[80] R. Pessoa, S. Gandolfi, S. A. Vitiello, and K. E. Schmidt, Physical Review A **92**, 063625 (2015).

[81] Y. Yan and D. Blume, Physical Review A **91**, 043607 (2015).

[82] C. M. Holland, Y. Lu, and L. W. Cheuk, Science **382**, 1143 (2023).

[83] L. D. Carr, D. DeMille, R. V. Krems, and J. Ye, New Journal of Physics **11**, 055049 (2009).

[84] S. E. Anderson, K. C. Younge, and G. Raithel, Physical Review Letters **107**, 263001 (2011).

[85] B. Yan et al., Nature **501**, 521 (2013).

[86] J. Biskupek et al., ACS Nano **14**, 11178 (2020).

[87] J. Cioslowski and A. Nanayakkara, Physical Review Letters **69**, 2871 (1992).

[88] B. Abolins, R. Zillich, and K. Whaley, Journal of Low Temperature Physics **165**, 249 (2011).

[89] B. Abolins, R. Zillich, and K. Whaley, Journal of Low Temperature Physics **170**, 131 (2013).

[90] B. P. Abolins, R. E. Zillich, and K. B. Whaley, The Journal of Chemical Physics **148** (2018).

[91] D. Marx, O. Opitz, P. Nielaba, and K. Binder, Physical Review Letters **70**, 2908 (1993).

[92] D. G. Hobson and W. Werner, Bulletin of the London Mathematical Society **28**, 643 (1996).

[93] E. T. Whittaker and G. N. Watson, *A Course of Modern Analysis*, Cambridge University Press, 1996.

[94] K. Binder, Zeitschrift für Physik B Condensed Matter **43**, 119 (1981).

[95] S. Geman and D. Geman, IEEE Transactions on Pattern Analysis and Machine Intelligence **6**, 721 (1984).

[96] S. Bravyi, D. P. Divincenzo, R. I. Oliveira, and B. M. Terhal, arXiv preprint arXiv:quant-ph/0606140 (2006).

[97] G. Pan and Z. Y. Meng, arXiv preprint arXiv:2204.08777 (2022).

[98] D. Thirumalai, E. J. Bruskin, and B. J. Berne, The Journal of Chemical Physics **79**, 5063 (1983).

[99] R. M. Fye, Physical Review B **33**, 6271 (1986).

[100] M. Fishman, S. White, and E. M. Stoudenmire, SciPost Physics Codebases (2022).

[101] P. Henelius and A. W. Sandvik, Physical Review B **62**, 1102 (2000).

[102] B. Bauer, S. Bravyi, M. Motta, and G. K.-L. Chan, Chemical Reviews **120**, 12685 (2020).

[103] A. Montanaro, npj Quantum Information **2**, 1 (2016).

[104] S. B. Bravyi and A. Y. Kitaev, Annals of Physics **298**, 210 (2002).

[105] K. Setia, S. Bravyi, A. Mezzacapo, and J. D. Whitfield, Physical Review Research **1**, 033033 (2019).

[106] F. Verstraete and J. I. Cirac, Journal of Statistical Mechanics: Theory and Experiment **2005**, P09012 (2005).

[107] J. T. Seeley, M. J. Richard, and P. J. Love, The Journal of Chemical Physics **137**, 224109 (2012).

[108] R. Somma, G. Ortiz, E. Knill, and J. Gubernatis, International Journal of Quantum Information **1**, 189 (2003).

[109] N. P. Sawaya et al., npj Quantum Information **6**, 49 (2020).

[110] S. McArdle, A. Mayorov, X. Shan, S. Benjamin, and X. Yuan, Chemical Science **10**, 5725 (2019).

[111] K. Georgopoulos, C. Emary, and P. Zuliani, Physical Review A **103**, 022408 (2021).

[112] S. Roman, S. Axler, and F. Gehring, *Advanced Linear Algebra*, Springer, 2005.

[113] D. E. Knuth, Mathematics of Computation **61**, 277 (1993).

[114] N. S. Mande and R. de Wolf, arXiv preprint arXiv:2305.04908 (2023).

[115] K. Setia and J. D. Whitfield, The Journal of Chemical Physics **148**, 164104 (2018).

[116] J. Tilly et al., Physics Reports **986**, 1 (2022).

[117] R. B. Lehoucq, D. C. Sorensen, and C. Yang, *ARPACK users' guide: solution of large-scale eigenvalue problems with implicitly restarted Arnoldi methods*, SIAM, 1998.

[118] C. Lanczos, Journal of research of the National Bureau of Standards **45**, 255 (1950).

[119] J. R. McClean et al., Quantum Science and Technology **5**, 034014 (2020).

[120] V. Senicourt et al., arXiv preprint arXiv:2206.12424 (2022).

[121] C. Monroe et al., Reviews of Modern Physics **93**, 025001 (2021).

[122] R. Blatt and C. F. Roos, Nature Physics **8**, 277 (2012).

[123] C.-Y. Park and N. Killoran, Quantum **8**, 1239 (2024).

[124] Sumeet, M. Hörmann, and K. Schmidt, Physical Review B **110**, 155128 (2024).

[125] J. Wang and R. Jaiswal, arXiv preprint arXiv:2308.12020 (2023).

[126] Y. Javanmard, U. Liaubaite, T. J. Osborne, X. Xu, and M.-H. Yung, APL Quantum **1**, 046114 (2024).

[127] K. Dalton et al., npj Quantum Information **10** (2024).

[128] M. Headrick, arXiv preprint arXiv:1907.08126 (2019).

[129] I. Bengtsson and K. Życzkowski, *Geometry of Quantum States An Introduction to Quantum Entanglement*, Cambridge University Press, 2017.

[130] C. M. Herdman, S. Inglis, P.-N. Roy, R. G. Melko, and A. Del Maestro, Physical Review E **90**, 013308 (2014).

[131] P. Patil, H. Shao, and A. W. Sandvik, Physical Review B **103**, 054418 (2021).

[132] J. Roffe, Contemporary Physics **60**, 226 (2019).